Electrical characterization of process induced defects in GaAs by Laplace deep level transient spectroscopy

UNIVERSITEIT VAN PRETORIA
UNIVERSITY OF PRETORIA
YUNIBESITHI YA PRETORIA

Fatemeh Taghizadeh

Submitted in partial fulfilment of the requirements for the degree of
Doctor of Philosophy (PhD) in Physics

In the
Faculty of Natural and Agricultural Sciences
Department of Physics
University of Pretoria

July 2019

Supervisor: Prof. F. D. Auret
Co-supervisor: Prof. W. E. Meyer

Declaration of Authorship

I**,** Fatemeh Taghizadeh, declare that the thesis entitled *"Electrical characterization of process induced defects in GaAs by Laplace deep level transient spectroscopy"* which I hereby submit for the degree Doctor of Philosophy (PhD) in Physics is the results of investigations carried out by me under the supervision of Prof. F. D. Auret and co-supervision Prof. W. E. Meyer at the University of Pretoria South Africa. It is my original work and has not previously been submitted by me for a degree at this or any other tertiary institution.

Signed: _____

Date: _____

Abstract

In this study, we investigated defects introduced in n-GaAs with different carrier densities by electron irradiation and sputter deposition by means of conventional deep level transient spectroscopy (DLTS) as well as high resolution Laplace deep-level transient spectroscopy (L-DLTS). In electron-irradiated material, we found that the well-known E3 defect, of which the origin has long been under discussion, consisted of three components (E3a, E3b and E3c). By constructing Arrhenius plots and performing annealing studies, and by comparing our results with literature, we could deduce that the E3a, the main component of the E3 is related to the V_{As}, while the E3b is related to the As_i and the E3c was related to the V_{Ga}-Si_{Ga}. In addition, the E3c was metastable and had a concentration that increased linearly with doping concentration. Further electrical characterization included *I-V* and *C-V* measurements, as well as measurements of the introduction rate, metastability, electric field emission mechanisms and capture cross-sections.

For the sputter-deposited Schottky contacts, DLTS depth profiles showed that the defects were confined close to the surface and that their depth range depended strongly on the doping concentration, and corresponded roughly with the depletion depth of the Schottky diodes. We conclude that the diffusion of these defects was stronlgy enhanced by the conditions (free carrier density and electric field) in the depletion region. Six defects (S1, S2, S3, S4, S5 and S6) were observed by conventional DLTS and were further investigated by L-DLTS. One of these defects, the S6, could be split into two components while three of them (S1, S3 and S5) were metastable. The transformation kinetics of the metastable defects were investigated and we conclude that the prefactor of S5 to S3 transformation was related to free carrier emission but for the S3 to S5 transformation is larger than would be expected. The activation energy of these transformations was similar to that required for arsenic vacancy (V_{As}) diffusion. The real capture cross sections as well as capture barriers were measured for the S3, S4 and S5 defects.

Acknowledgements

All praises are due to the almighty God, the Lord of the worlds. I would not be here today without his blessing, mercy and never-ending grace. Thank you, Lord.

I would like to take this opportunity to express my sincere gratitude towards my supervisor Prof. F. D. Auret for his support, encouragement, constructive criticism, valuable suggestion and his fatherly guidance.

I would also like to express my deepest gratitude to my co-supervisor, Prof W. E. Meyer, for his expert advice and encouragement throughout this Project. Only God can repay them both for all the kindness they have shown towards me.

I would also like to express my gratitude to Mr P. J. Janse van Rensburg and Mr M. Legodi for their contributes towards measurements, and their role in providing technical expertise with regards to sourcing and familiarizing me with lab equipment and proper procedure.

I would also wish to give unending appreciation to my father, Hadi, and my mother, Rana, for their prayers, support, love and encouragement which kept me standing strong throughout all the struggles and frustrations. Also, to my lovely sister, Sepideh, who constantly encouraged and supported me during my work. May God keep you all in good Health.

My special gratitude goes to Kian Ostvar for his encouragement, help, support, guidance. This work would not materialize without him.

I would like to give thank to my dear colleagues, Ms Helga Danga, Mr Shandirai Tunhuma, Dr Ezeikel Omotoso, Mr Meehleketo Mayimele, Mr Abraham Willem Barnard and Mr Phuti Ngoepe, Thanks for your help and support.

I would also like to especially thank my friend Dr Farshad Barzegar for his help and support and my other close friends in South Africa and Iran who support and encouraged me.

Once again I say thank to all the people who have helped me directly or indirectly.

Abbreviations

LEC	Liquid encapsulated Czochralski
VGF	Vertical gradient freeze
MOCVD	Metal organic chemical vapour phase
MOVPE	Metalorganic vapor phase epitaxy
MBE	Molecular beam epitaxy
LED	Light emitting diode
SBD	Schottky barrier diode
DLTS	Deep-level transient spectroscopy
L-DLTS	Laplace-transform deep-level transient spectroscopy
MS	Metal semiconductor
MOS	Metal oxide semiconductor
SNR	Signal to noise ratio
RE	Resistive evaporation
SD	Sputter deposition
MPE	Multiphonon emission

Physical Constants

Boltzmann constant	$k = 1.380\ 658 \times 10^{-23}\ JK^{-1}$
Elementary charge	$e = 1.602\ 177 \times 10^{-19}\ C$
Electron effective mass	$m_e^* = 9.109\ 390 \times 10^{-31}\ Kg$
Electron-volt	$eV = 1.602\ 177 \times 10^{-19}\ J$
Planck's constant	$\hbar = 6.626\ 076 \times 10^{-34}\ Js$

Symbols

E_D	Threshold energy
$e(F)$	Emission rate of electric field
$e\phi_m$	Work function of metal
$e\phi_s$	Work function of semiconductor
$e\chi_s$	Electron affinity of semiconductor
ϕ_{bi}	Built in potential
ϕ_{bn}	Schottky barrier height
v_{th}	Thermal velocity
σ_n	Capture cross-section
e_n	Emission rate
τ	Tunneling time
V_R	Reverse bias
ε	Permittivity of semiconductor
V_{bi}	Built-in voltage
E_α	Activation energy
α	Temperature coefficient
I-V	Current-voltage
C-V	Capacitance-voltage
ϕ_{bIV}	*I-V* barrier height
ϕ_{bCV}	*C-V* barrier height

Dedication

This desertion is dedicated to my beloved parents

who taught me to trust God, for their prayers,

supporting and encouraging me to believe in

myself and making me who I am.

Table of Contents

List of Figures

1 INTRODUCTION

1.1 Crystal structure and growth

Semiconductor diodes were the first electronic devices. Here we briefly explained the history of diodes and materials used for that (Note that, in this work we used GaAs and we concentrate on this material). In 1874, Braun [1] investigated the "unilateral conduction" across the contact between a metal and a certain crystal material (while in 1873, thermionic emission discovered by Guthrie [2]). Fitts constructed the first selenium diodes in 1886 but was not practical till the 1930s while he found an application which converted AC voltage to DC in an industrial environment with large power requirement [3]. In 1894, Chandra Bose used a crystal for detecting radio waves for the first time [3]. After that Pickard patented a silicon detector in 1906 [4]. In 1930s researchers recognized the potential of the crystal detector in microwave technology. [5]. From that time the material was used for the development of electronic devices. Germanium (Ge) was the first material that was used in semiconductor electronics. After Ge, Silicon (Si) came into the semiconductor market, and in 1960s the first GaAs transistor entered the commercial market [6]. Gallium arsenide (GaAs) is a III-V semiconductor which is composed of Ga from group III and As from group V of the periodic table. GaAs was first synthesized in 1929 by Goldschmidt [7], and the first GaAs diode was reported in 1958 [8].

Gallium has 31 electrons, and according to the electron configuration, as shown in Figure 1.1, Ga has two electrons in the 4s subshell and 1 electron in the 4p subshell. That means gallium has 3 valence electrons. According to the Figure 1.2 on the electronic configuration of As, it has 33 electrons, 2 electrons in the 4s subshell and 3 electrons in the 4p subshell. This means that As has 5 valence electrons [9].

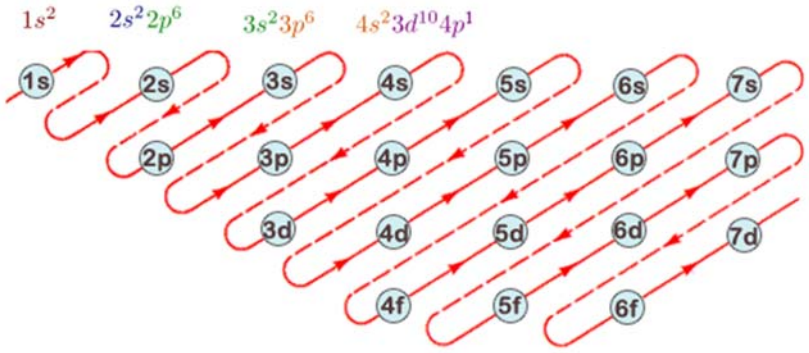

Figure 1.1: Electron configuration of Gallium [9].

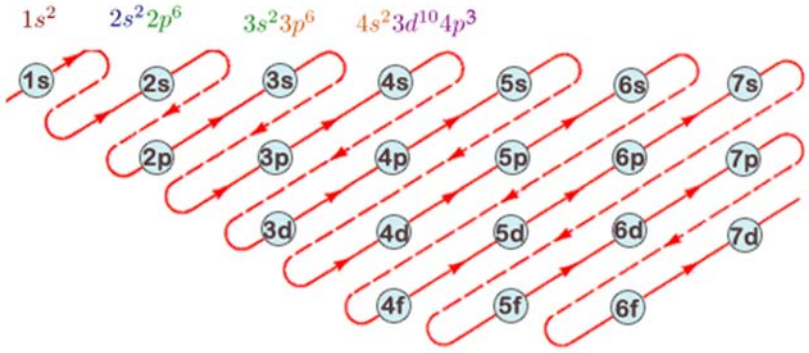

Figure 1.2: Electron configuration of Arsenic [9].

The GaAs crystal configuration is known as the zinc blende structure. Figure 1.3 illustrates the zinc blende structure of GaAs. This crystal consists of two face centred cubic (fcc) lattices, offset by a quarter of a body diagonal.

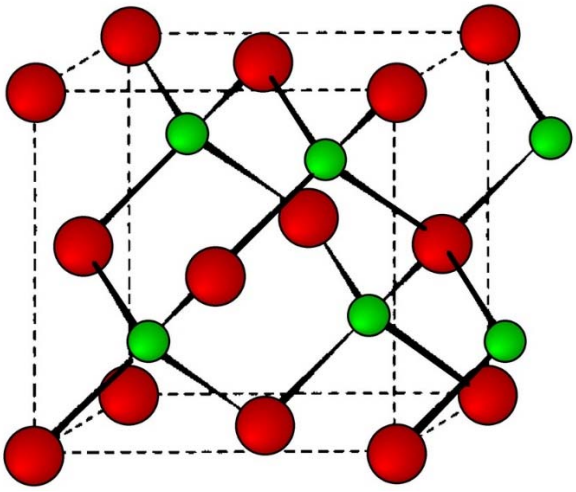

Figure 1.3: Model of a cubic unit cell of GaAs showing the zinc blende crystal structure [10]. The red and green spheres represent gallium and arsenic respectively.

Each Ga atom is surrounded by As atoms and each As atom is surrounded by Ga atoms. The Ga atoms bond with arsenic atoms forming a 4 co-ordinate tetrahedron with a lattice constant of 5.67 Å [11]. GaAs has covalent bonds between its atoms, and two interpenetrating face centred cubic-sub-lattices which are separated by 2.44 Å [12]. If elements intentionally introduced at a Ga site are from group four of the periodic table, like Si, the elements act as dopants and become *n*-type.

The energy band gap between the conduction band and the valence band in GaAs is 1.43 eV. GaAs has a direct band gap which is larger than that of Si and Ge [13].

The direct band gap in GaAs permits light emission at high efficiency [14]. GaAs also displays good resistance to ionizing radiation - up to 1 Grad, which is about two orders of magnitude higher than that of Si-based devices [15].

By slowly cooling molten material, bulk semiconductor crystals are obtained. There are different methods to grow the single bulk crystal, but the two main methods are Czochralski and Bridgman.

Some methods to prepare single crystal and films of gallium arsenide include:

- Bulk Crystals:
  - Bridgman- Stockbarger techniques, in which gallium and arsenic vapours react, and free molecules deposit on a seed crystal at the cooler end of the furnace [16].

- Liquid encapsulated Czochralski (LEC) growth to produce high purity single crystals can exhibit semi-insulating characteristics [17]
- The vertical gradient freeze (VGF) process [18]

- Epitaxial Layers:
  - Vapour-phase epitaxy VPE reaction of gaseous gallium metal and arsenic trichloride [19].
  - Metal-organic chemical vapour deposition (MOCVD) reaction of trimethylgallium and arsenic [20].
  - Molecular beam epitaxy (MBE) of gallium and arsenic [21]

1.2 GaAs applications

Due to its properties, GaAs has many applications including solar cell, computer networking, radiation hard electronics and microwave diode technologies. Other examples are:

- space applications [22],
- high-efficiency solar cells [23], [24],
- detection of X-rays [25],
- near-infrared laser diodes (since 1962) [26],
- spin-polarized electron sources [27],
- cellular phone technology [28] and
- Opto-electronic devices such as: Light emitting diodes (LED's), lasers and detectors [8].

1.3 Irradiation and sputter deposition induced defects

Materials are constantly subjected to ionizing radiation in a variety of different ways and in different environments. However, the effects are highly dependent on the characteristics of the exposed material as well as factors such as the type and fluence of the radiation and also the duration of exposure.

On earth, the effective radiation levels in the majority of environments are too low to significantly affect most materials, therefore significant exposure is only experienced close to radioactive sources as well as manmade equipment such as particle accelerators.

However, in space, an object is constantly subjected to high-energy radiation. For instance, earth-orbiting satellites experience high levels of radiation that originate from the Van Allen belts where the interaction between the earth's magnetic field and charged particles form a radiation-rich environment. Furthermore, cosmic rays, gamma rays, low-energy plasma, solar flares and so forth, are other sources of radiation. Aside from electromagnetic waves, these cosmic radiations consist of high-energy electrons, alpha particles (protons), neutrons and etc.

In the 1950s, at the beginning of the space age, the effects of irradiation on semiconductors drew much attention, whereas, a wide range of studies on radiation-induced defects were undertaken in the 1960s. The results of these studies on radiation-induced defects expanded our understanding of some of the important features of defect physics, such as defect generation, annealing, migration and lattice relaxation. However, thanks to the vital importance of semiconductors in our modern technology, the study of the radiation-induced effects in semiconductors is still a subject of much interest in the scientific community [29], [30].

Particle irradiation has a major role in the creation, operation and life-cycle of many semiconductor-based devices. For instance, irradiation is used to vary the properties of materials in a controlled manner, for instance during transmutational doping of semiconductors and device isolation by proton implantation. It is a widely used processing technique, since it offers many practical benefits from a manufacturing point of view, such as the ability to perform multiple processing steps under vacuum without the need to expose the semiconductor (material) to the atmosphere. However, aside from the intentional effects, interactions of energetic particles with the material itself or the impurities within it can produce unwanted changes to the surface of the

material or even deeper layers. Therefore, these effects are studied and are considered as advancements made in semiconductor technology.

Another important field of this type of study is concerned with semiconductor-based components (mostly electronics) that are meant to operate in or near a radiation-rich environment. Since the operation, efficiency and life cycle of these devices as influenced by nuclear radiation, proper understanding of these effects are necessary before they are designed for such applications. In this respect, if such components are critical to the success of a mission (outer space) or safety of system operators (nuclear applications), failures can have severe negative consequences [30].

One important tool in the study of irradiation-induced defects in semiconductors was introduced by Lang *et al.* in 1970 [31]. This technique, called deep-level transient spectroscopy, is capable of characterizing deep-level defects in semiconductors based on properties of metal-semiconductor junctions.

The electrical properties of semiconductors can change drastically by radiation where the type and fluence of the radiation can affect the material differently. Radiation affects semiconductors' lattice structure by introducing vacancies, interstitials, interstitial vacancy-impurity complexes, electron-hole pairs and charging effects [32]. Research on GaAs defects started in 1977 [33]. Scientists proposed different models about the nature of these defects and their origin. The E3 defect is one of the defects in *n*-type GaAs which is introduced by radiation, and its energy level is located at 0.35 eV below the conduction band minima. This defect consists of three different components, and each component has its specific properties. The electrical properties of this defect are described in Chapter 4 of this thesis.

Sputter deposition was used to fabricate both low- and high-barrier Schottky barrier diodes (SBD's). This method has many advantages such as: depositing metal with a high melting point, high deposition rates and the stoichiometrical deposition of compounds [34]. The energetic particles incident on the semiconductor during the process introduce surface and sub-surface disorder (defects), which affect the Schottky barrier diode characteristics [35]. These electrical properties are treated and described in Chapter 4. All defect characterization measurements were done by conventional DLTS and Laplace DLTS high-resolution method [36].

1.4 Outline of the thesis

This thesis is divided into 5 chapters:

- Chapter 2 is a literature review on the formation of defects, ideal Schottky diodes and the theory of methods and different measurements to investigate the electrical properties of defects.
- Chapter 3 elaborates on the experimental techniques used to investigate the features of defects.
- Chapter 4 contains the results and a discussion.
- Chapter 5 general conclusions and future work are discussed.

2 LITERATURE REVIEW

Semiconductors are called semiconductors because they represent a type of material that has a conductivity between conductors and insulators under the same conditions. Semiconductors can be either elemental (consisting of just one element), such as germanium or silicon, or compounds like gallium arsenide or silicon carbide. The energy band model is one of the methods used to describe the electrical properties of a solid. According to the energy band model, solids can be divided into three different groups: conductors, insulators, and semiconductors. This depends on the properties of the two energy bands above and below the Fermi-energy (called the valence and conduction band). The difference in energy between the highest valence state and lowest conduction band state is the band gap, which is the region where no electron state can exist. The band gap is the significant factor in determining the electrical properties of materials. In general, the band structure of a solid is the combined result of quantum interactions among electron levels of individual atoms with one another and is, therefore, a consequence of the atomic structure of the solid. Hence, if this atomic structure is perturbed in any way, the effects might be observed in the band structure.

When a metal comes in contact with a semiconductor, a rectifying contact, called a Schottky barrier diode (SBD) may be formed. SBDs contain a depletion region in the semiconductor from which defect information can be extracted by, for example, deep-level transient spectroscopy (DLTS).

Defects change the properties of SBDs and the semiconductors on which they are formed. Defects are formed when foreign atoms are present in the semiconductor or when atoms are displaced from their regular lattice positions by radiation or processing [13], [16].

In the present study DLTS and Laplace DLTS were used to characterize the electrical properties of defects in semiconductors during electron irradiation and sputter deposition. In this chapter, we explain the theory of the formation and properties of SBDs under ideal and non-ideal conditions. The nature of different kinds of defects is detailed. The DLTS and high-resolution DLTS (Laplace-DLTS) techniques are explained as well.

2.1 Semiconductor defects

Defects are known as any imperfection in a crystal lattice such as displacement, addition, missing or foreign atom that interrupts the continuity in the lattice repetition. Defects can be introduced during the growth of the material, fabrication of devices or exposure of devices to radiation. These defects affect the properties of the material and, amongst others, cause localised energy states in the band gap of a semiconductor. The electrical conductivity of a semiconductor is important and by introducing impurity atoms, they can be modified. These impurities introduce acceptor and donor states in the band gap close to the top of the valence band and close to the bottom of the conduction band [6].

2.1.1 Categorization of defects

1. Point defect: this type of defect is localized at or near a single atom. Point defects can be formed by displacing or removing a single atom or a cluster of atoms from the original positions or by introducing foreign atoms into the lattice. A summary is given here of different types of point defects with illustrations of some of these point defects in Figure 2.1.

    - Vacancy defect: A defect in which an atom is missing from a position that should have been occupied in the perfect crystal [37].
    - Interstitial defect: A type of defect in which a foreign atom occupies a site in the crystal structure where there should not be an atom [38].
    - Self-interstitial: An interstitial atom of the same species as the semiconductor [39].
    - Frenkel defect: Occurs when a lattice atom is displaced into an interstitial site, thereby creating a vacancy-interstitial pair [40], [41].
    - Substitutional impurity: Crystal lattice position occupied by a foreign atom [42]

An antisite defect [43] is another type of point defect in compound semiconductors, where an atom is on the wrong lattice site (i.e. Ga on an As position in GaAs).

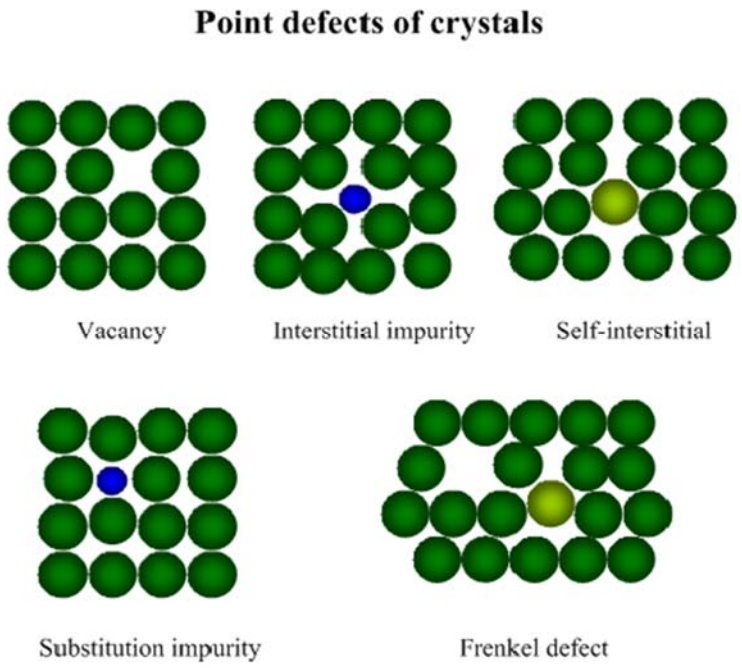

Figure 2.1**:** A sketch of different kinds of point defects in a semiconductor crystal [44].

2. Line defect: is a one-dimensional defect. A dislocation is a linear defect which appears when an entire row of lattice points deviate from the perfect arrangement [45]. Dislocations are generally caused by stress being applied to the lattice and are categorized into two types: Edge dislocation and Screw dislocation [45].

3. Planar defect: is a two-dimensional defect and formed when distortion occurs across a plane. Two different forms of planar defects are: Grain boundary and Stacking fault [46].

4. Bulk defect: A three-dimensional defect which is a volume distortion in the crystal lattice. These defects can be inclusions, pores, cracks, voids (small regions without any atoms -

can be considered as clusters of vacancies) or precipitates (impurities clustered together to form small regions of a different phase). [47].

2.1.2 Deep and shallow level defects

Electrical properties of semiconductors can be modified by systemically introducing impurities. Defects are classified as shallow level or deep, based on the localization of their wave functions. The energy states of shallow levels are close to the band edges and their wave functions are not localized. The properties of these shallow levels are well described by a suitably adapted version of the Bohr model of the hydrogen atom [48]. In terms of the band model for semiconductors, the deep levels are usually further from the valance and conduction band are more localized by comparison to shallow levels.

Shallow levels are easily ionized by thermal excitations and carriers will be released into the semiconductor's conduction and/or valence bands. These impurities are called dopants. For *n*-type materials, the dopant materials are donor atoms, causing the donation of electrons to the conduction band and thus leaving positively charged ionized donors. Conversely, for *p*-type material, the dopant materials are acceptor atoms which introduce holes into the valance band.

Binding of electrons is stronger for deep-level defects which levels interfere with electrical transports and other properties of the semiconductor. They behave as recombination centres and allow electrons and holes to recombine and nullify each other's effects. This phenomena can lead to an increased level of noise in transistors and photodiodes [48] as well as decreasing efficiency of solar cells [49]. However, this phenomenon can result in increasing the switching speed of diodes [50], [51].

2.1.3 Radiation-induced defects in GaAs

Electron irradiation in the 1 MeV range, introduces vacancy-interstitial pairs [52]. Energetic particles penetrate into the semiconductor material and lose their energy through interaction with the host atoms of the crystal lattice. Some of the energy is lost via ionization of the target atom and the rest of the energy is transferred via non-ionizing events where the target atom is displaced [53]. One of the decisive parameters related to primary damage production is the displacement

threshold energy (E_{Dis}), which can be used to estimate the total damage in the material theoretically [54]. The threshold energy is the minimum amount of energy required to displace an atom from its original position in the lattice and possibly result in creating a Frenkel pair [52]. For most materials, the displacement threshold energy is around 10 eV. The threshold energy can be specified as the minimum energy required to produce a Frenkel pair of a given atom in the lattice for GaAs [55]. Previous experiments measured the threshold energy in GaAs (using DLTS and frequency-domain technique) to be approximately 10 eV [56], [57]. Furthermore, using nonelectric methods, namely molecular dynamic (MD) simulations, at low temperature, Nordlund *et al.* proposed a value of 15 eV. [58]. Recently, Chen *et al.* analysed the threshold energy depending on the crystallographic direction, reporting a minimum E_{Dis} of 8 eV and maxima of 22 and 28 eV for Ga and As, respectively [54]. The average displacement threshold energy is 13±1 eV.

2.1.4 Process induced defects in GaAs

As-grown bulk and epitaxial wafers are used to fabricate electronic devices. Typical processes include: oxidation, dopant diffusion, ion implantation and metallization. According to the type of device, some or all of these processes are used. Metallization is an important processing step and is used, among others, to fabricate Schottky and ohmic contacts to semiconductors. [59].

Sputter deposition is one of the techniques which is used to fabricate contacts with special properties. This technique results in more intimate contacts compared to the other deposition methods. Furthermore, sputter-deposited contacts have good adhesion to different substrates (metals, semiconductors and oxides).

Sputter etching is one of the related dry processing techniques used to remove contamination from the surface of semiconductors.

Both sputter etching and deposition cause surface damage that usually decreases and increases Schottky barrier heights on n- and p-type semiconductors, respectively, as reported by Weinman *et al.* [60], Fonash *et al.* [61] and Vandenbroucke [62]. Sputtering also causes defects deeper in the material that may be detected by DLTS.

2.2 Metal-semiconductor junctions

Metal-semiconductor (MS) junctions have been studied widely on account of their usage in devices and also because they are important tools that are used in the electrical characterization of many electrical properties of semiconductors. MS contacts are divided into rectifying and non-rectifying contacts according to their rectifying properties. Rectifying contacts allow current flow in one direction only, but non-rectifying contacts allow free current flow in both directions. Schottky contacts are rectifying contacts while Ohmic contacts are non-rectifying contacts. Although there are many different models that can be used to explain the operation of a metal-semiconductor contact, the model proposed by Schottky in 1924 [63] will be exclusively used in this work.

2.2.1 The ideal case

When a metal comes into contact with the semiconductor material, a potential barrier may be formed at the interface. The mechanism of Schottky diode formation is discussed in numerous publications (e.g. [64], [65]) and is summarised in the following paragraphs, based on Figure 2.2, For a detailed discussion regarding metal-semiconductor contacts, please refer to Sze & Ng [13]. In Figure 2.2 (A), E_C represents the bottom of the conduction band and E_V the top of the valance band. Part (A) illustrates the electrically neutral, isolated metal and semiconductor. The Fermi levels (E_F) of the metal and semiconductor have different positions. Here $e\chi_s$ is the electron affinity of the semiconductor (the energy released when an electron is added to the semiconductor), While $e\phi_m$ and $e\phi_s$ respectively denote the work functions of the metal and the semiconductor. The work function of a material is defined as the minimum required energy to separate an electron from the material. In other words, the work function is the difference between the vacuum level and the Fermi level while the difference between the vacuum level and the energy level of the conduction band edge is referred to as the electron affinity of the semiconductor. As shown in Figure 2.2, the electron affinity of the semiconductor is lower than that of the metal, which causes the formation of a Schottky contact.

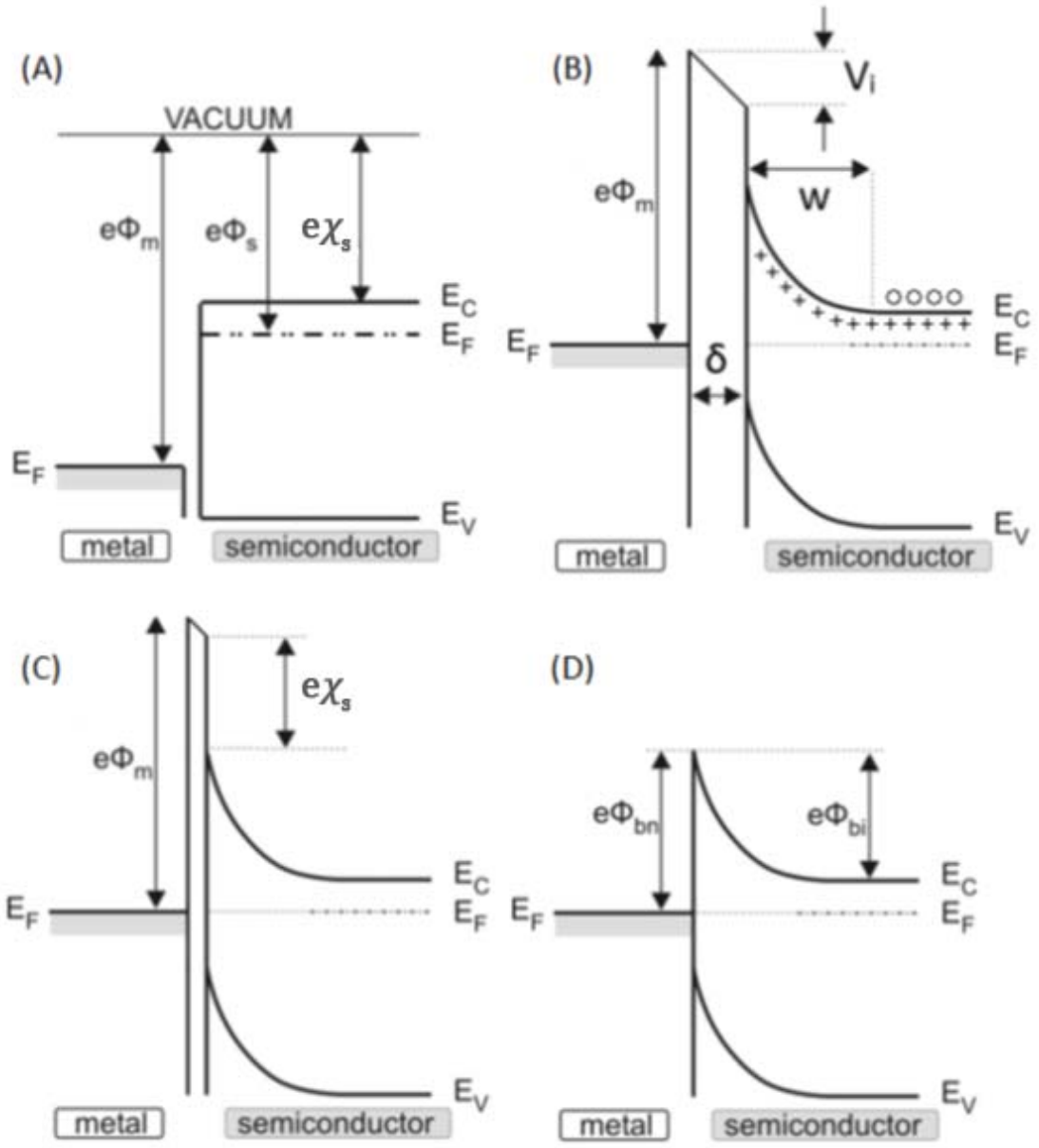

Figure 2.2: The formation of a Schottky barrier: (A) the metal and semiconductor are in their isolated vacuum conditions, (B) electrically connected, (C) separated by a narrow gap and (D) in intimate contact [64].

If the metal and *n*-type semiconductor are electrically connected with an imaginary thin wire, as a result of the difference in the Fermi level of the semiconductor and the metal, there will be a flow of electrons from the semiconductor to the metal. After the flow is stabilized, the surface of the

metal will be negatively charged while positive charges accumulate on the surface of the semiconductor. Donor atoms are the reason for the positive charge of the semiconductor with a lack of electrons. As long as the finite concentration of donors is there, this region is empty of electrons. This region, called the depletion region, spans from the MS interface to a specific depth in the semiconductor. As opposed to this, a very high concentration of electrons can be incorporated in the metal, and this charge concentration is confined to the surface on the metal.

As long as the Fermi levels of two materials approach each other, this build-up of charge will continue. During this procedure, an electric field will be created in the gap (δ) between the two materials because the vacuum levels are no longer the same. Figure 2.2 (B) shows the depletion region (width *w*), created due to the electric field.

Here V_i represents the difference between the electrostatic potentials at the surfaces of the metal and semiconductors (differences between the two vacuum levels), As shown in Figure 2.2(C), the electric field in the gap will increase if the gap (δ) between these two materials decreases. However, the electric fields remain finite. The energy difference between the vacuum levels of semiconductor and metal decreases according to the Equation (2.1):

$$E_f = qV_i . \tag{2.1}$$

When the two materials are almost in contact, a small potential barrier forms that separates the two surfaces (V_i is practically zero). However, due to the narrow size of this barrier, electrons easily passes through it by the tunnelling effect.

The ideal case, as shown in Figure 2.2 (D), occurs when the barrier of the vacuum disappears completely, and the electrons will only experience the potential barrier due to the bending of the bands. As described, the difference between the semiconductor electron affinity and the metal work function determines the magnitude of the potential barrier [66]. The height of this barrier is measurable relative to the Fermi level as stated by Equation (2.2):

$$e\phi_b = (e\phi_m - e\chi_s). \tag{2.2}$$

The barrier height relative to the position of the conduction band in the neutral semiconductor is called the diffusion potential (or built-in potential barrier) [67], and is indicated by $e\phi_{bi}$ Under zero bias conditions, it is equal to [13]:

$$e\phi_{bi} = e\phi_b - (e\phi_s - e\chi_s). \tag{2.3}$$

2.2.2 Non-ideal case (effects on the barrier height)

According to the report by Grundmann [68], the metal-semiconductor Schottky barrier height between GaAs and most metals is approximately 0.8 V, i.e. the barrier height is not as sensitive to the work function of the metal as expected. This has also been reported by Rhoderick [64] and Myburg *et al.*[69] that the relationship between the metal work function and the Schottky barrier height is not linear. Factors that can affect the Schottky barrier height among others are; the presence of surface or deep-level defect and electric field.

The model of a Schottky diode can be explained as follows:

- There is an interfacial layer of atomic dimensions between metal and semiconductors. This layer is able to accommodate a potential difference, though it is transparent to the flow of electrons.
- The interface state density, which is expressed as the number of states per unit area of the interface and per unit energy in the semiconductor band gap, is characteristic of the semiconductor and does not depend on the metal type.
- A distribution of surface states at the metal-semiconductor interface exist, which are donor like if below the surface potential, and acceptor like if the states are above the surface potential [13].

2.2.3 Reverse and forward bias

By applying a bias across the barrier, the Fermi levels of the semiconductor and the metal shift with respect to each other. When no bias is applied, the rate of electron flow from both sides of the junction is equal, therefore there is no net flow of electrons across the barrier. By applying a reverse bias (in the case of a *n*-type semiconductor, this means applying a positive voltage to the semiconductor relative to the metal) the Fermi level of metal is raised relative to that of the semiconductor, and the depletion width is increased. The semiconductor's bands bend further causing an increased barrier height for electrons in the semiconductor as shown in Figure 2.3 (A). At the same time, the barrier seen by an electron from the metal remains constant, so the current from the metal to the semiconductor does not change, while the same is not true for electrons on the semiconductor side as only those with adequate energy can overcome the barrier. This means that the current under reverse bias tends toward a limit as the reverse bias is increased. Under forward bias, the barrier for electrons from the semiconductor is decreased, while the barrier for electrons in the metal, as previously, remains constant. This leads to a rapid increase in the flow of electrons from the semiconductor to the metal as shown in Figure 2.3 (B) [70].

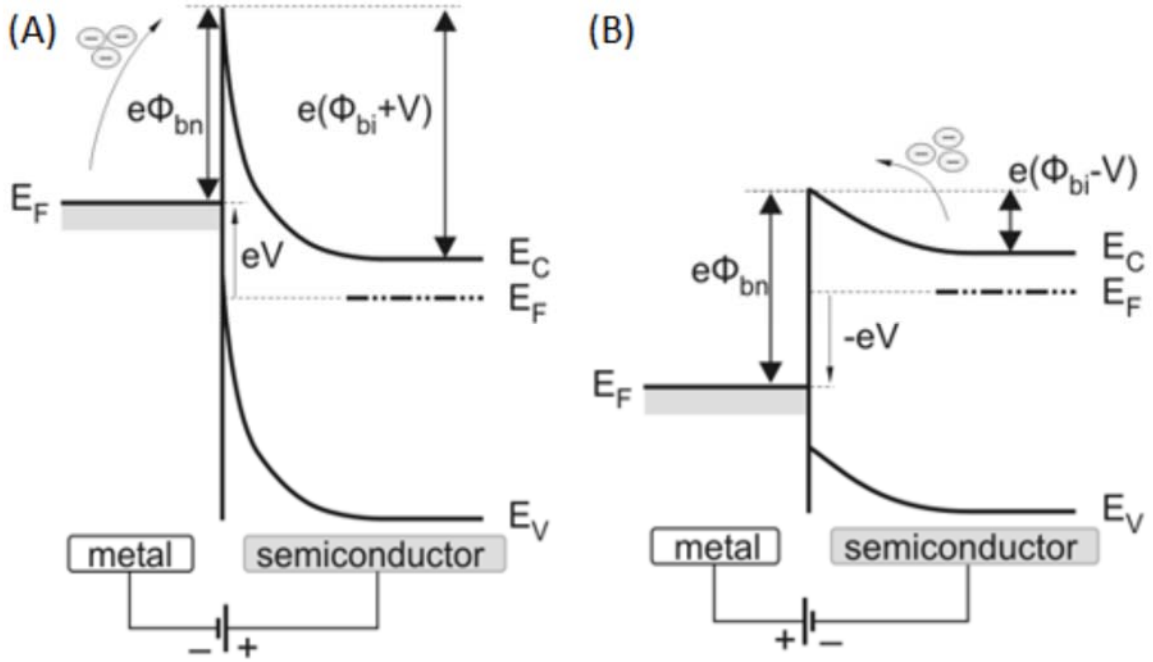

Figure 2.3: The Schottky barrier between a metal and semiconductor (*n*-type) with perfect contact under (A) reverse bias and (B) forward bias [64].

2.2.4 Emission and capture of carriers from defects

As mentioned previously, some of the properties of semiconductors are drastically affected by defect states in the band gap. Defects behave as donors or acceptors, the defect states can also affect the mobility of charge carriers by scattering. Defects can also cause features in the optical absorption and emission spectrum of the semiconductors. One of the significant effects is the emission and capture of charge carriers due to the deep levels in the band gap. This emission and capture of charge carriers lead defects to act as recombination or trapping centres, and influence the carrier lifetime in semiconductors.

The kinetics of emission and capture of carriers from defect levels have been well studied [71], [72], [73]. In this chapter, a single level with two charge states in a non-degenerate semiconductor will be discussed as originally proposed by Bourgoin [74].

Assume a defect with two charge states S and B, where the defect in the S state has one electron more than the B state. In what follows e_n and k_n are the emissions and capture rates of electrons and e_p and k_p are the emission and capture rates of holes.

Assuming that during the capture process there is no barrier for electrons to overcome, the probability per unit time that a defect in state B can capture an electron from the conduction band, can be written as

$$k_n = c_n n = \sigma_n \nu_{th,n} n \,, \tag{2.4}$$

where c_n is the electron capture coefficient of the defect, n is the concentration of the electrons, σ_n is the electron capture cross-section of the defect and $\nu_{th,n}$ is the thermal velocity of the electrons in the conduction band. Equation (2.5) describes the capture rate, which is similar to that for electrons and P is the concentration of holes in the valence band

$$k_p = c_p p = \sigma_p \nu_{th,n} p \,, \tag{2.5}$$

Here the densities of states in the conduction and valence bands are much higher than the carrier concentration, therefore, it is reasonable to assume that the total number of empty states are independent of the carrier concentration. So, the emission rates of electrons and holes are not dependent on the carrier concentration [74]. Taking *s* and *b* as the concentration of defects in states S and B respectively, the emission and capture rates of electrons and holes are given by:

electron emission	$e_n b$	
electron capture	$k_n s = c_n n s$	(2.6)
hole emission	$e_p s$	
hole capture	$k_p b = c_p p b$	

It must be noted that the capture and emission rates are equal at thermal equilibrium for both types of charge carriers. The superscript (^{0}) indicates the value of the quantity at equilibrium. Therefore, it follows that $c_n n^0 s^0 = e_n b^0$ and $c_p p^0 b^0 = e_p s^0$, now as shown in Equation (2.7) and (2.8), e_n and e_p can be expressed as:

$$e_n = c_n n^0 \frac{s^0}{b^0} = \sigma_n \nu_{th,n} n^0 \frac{s^0}{b^0} \tag{2.7}$$

and

$$e_p = c_p p^0 \frac{b^0}{s^0} = \sigma_p \nu_{th,p} p^0 \frac{b^0}{s^0}. \tag{2.8}$$

The ratio between the concentrations of two charge states of the defect in thermal equilibrium is:

$$\frac{s^0}{b^0} = \gamma \exp\left(\frac{E_T - E_F}{kT}\right), \tag{2.9}$$

In Equation (2.9), γ is a degeneracy factor [74], and E_T is defect's energy. The carrier densities at thermal equilibrium for electrons and holes are

$$n^0 = N_C \exp\left(\frac{E_F - E_C}{kT}\right) \tag{2.10}$$

and

$$p^0 = N_V \exp\left(\frac{E_V - E_F}{kT}\right). \tag{2.11}$$

If we substitute Equation (2.9) into Equation (2.8) and (2.7), and use Equations (2.10) and (2.11), we get Equation (2.12) and (2.13) for the emission rate of electrons and holes respectively

$$e_n = \sigma_n \nu_{th,n} \gamma N_C \exp\left(-\frac{E_C - E_T}{kT}\right) \tag{2.12}$$

and

$$e_p = \frac{\sigma_p \nu_{th.n} N_V}{\gamma} \exp\left(-\frac{E_T - E_V}{kT}\right). \tag{2.13}$$

By assuming a Boltzmann distribution, the thermal velocity of electrons can be written in terms of their effective mass m_e^*

$$\nu_{th,n} = \left(\frac{8kT}{\pi m_e^*} \right)^{\frac{1}{2}} \tag{2.14}$$

and the density of states in the conduction band N_C can be written as

$$N_C = \frac{1}{\sqrt{2}} \left(\frac{m_e^* kT}{\pi \hbar^2} \right)^{\frac{2}{3}}. \tag{2.15}$$

The emission rate is calculated by substituting Equation (2.14) and (2.15) into Equation (2.12),

$$e_n = \frac{2}{\pi \hbar^3} \frac{\sigma_n m_e^* k^2 T^2}{g} \exp\left(-\frac{E_C - E_T}{kT} \right). \tag{2.16}$$

The degeneracy γ used by Bourgoin has been replaced by $1/g$, here g is the degeneracy factor of the defect level.

If we consider that the capture cross-section of defect is not dependent on temperature, then an Arrhenius plot of $\ln(e_n / T^2)$ as a function of $1/T$ has produced a linear relationship from which energy E_T and capture cross-section σ_n of the defect may be calculated. The energy and capture cross-section are referred to as the defects' signature, and these are important parameters because they are used to identify a defect during electrical measurements.

The capture cross-section calculated from the Arrhenius plot is called the apparent capture cross-section, and the notation is $\sigma_{n,a}$. This frequently differs from the capture cross-section values obtained by direct methods.

2.2.5 Field dependence of the emission rate

As mentioned previously, there is an intrinsic electric field formed in the depletion region of a Schottky barrier diode. Sometimes the field in this region is quite large, almost up to the dielectric breakdown field of the semiconductor. If a defect is placed in this region it will be subject to the field, and then the shape of the potential well of a defect will be perturbed. This perturbation could increase the probability of emission of carriers trapped in the well. The extent of this increase is dependent on the dimensions and the shape of the potential perturbation. Here we will discuss two different mechanisms of electric field enhanced emission.

I. THE POOLE-FRENKEL EFFECT

One of the most common mechanisms responsible for enhanced emission is the Poole-Frenkel effect. The emission rate of a defect is enhanced by lowering the defect potential due to this mechanism. Emission enhancement due to this mechanism is mainly for shallow levels. The Poole-Frenkel effect is the governing enhancement mechanisms for low electric field strengths, nevertheless, for higher fields other mechanism are present. When an external electric field is applied to an electron trapped in a potential well, the electron will experience a combined electric field equal to the sum of the both fields. The applied field causes asymmetry lowering of the potential barrier. This causes a trapped electron to escape the well more readily. [75] as shown in Figure 2.4.

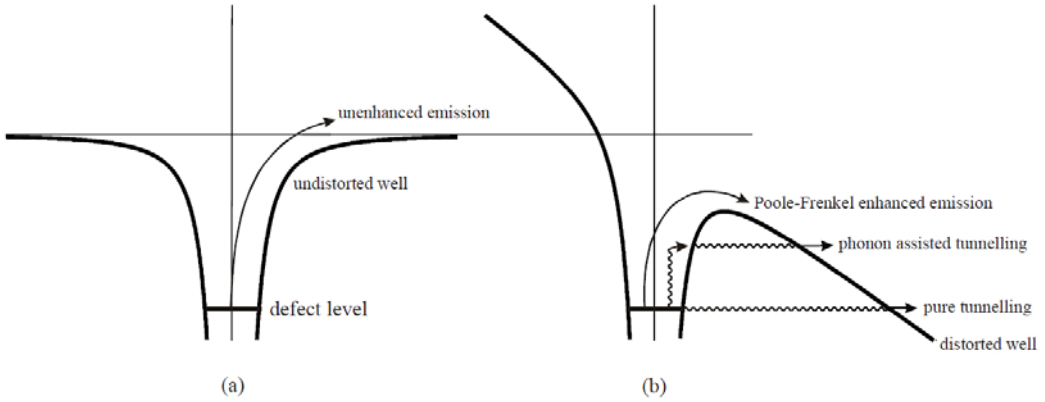

Figure 2.4: The columbic well in a (a) zero electric field, and (b) external electric field [76].

The Poole-Frenkel effect happens just for charged impurities, the ionization energy of a columbic well placed in an electric field is lowered by:

$$\Delta E_T = \sqrt{\frac{qF}{\pi\varepsilon}}\,. \tag{2.17}$$

If this equation is substituted in Equation (2.12), this indicates that the emission rate of the defect can be written as

$$e(F) = e(0)\exp\left(\frac{1}{kT}\sqrt{\frac{qF}{\pi\varepsilon}}\right), \tag{2.18}$$

Here $e(0)$ is the emission rate at zero electric field, k is the Boltzmann's constant, T is the absolute temperature, Here F is electric field and ε is permittivity of semiconductor.

The Poole-Frenkel effect is used by scientists to find the approximate range of the defect's potential. A stronger Poole-Frenkel enhancement would indicate a wider range of possible potentials.

A graph of log $e(F)$ as a function of $\sqrt{F}$, has been used to distinguish between donor or acceptor defects. A linear correlation is indicative of emission of a charge carrier from a centre with the opposite charge. Therefore, for an n-type material a linear log e is $\sqrt{F}$ correlation suggest emission of electrons from a donor type defect [74]. The Poole-Frenkel effect is observed only for charged impurities, while the phonon-assisted tunnelling or direct tunnelling, which occurs for high electric fields, is possible for impurities in all charge states. E.g. the field effect has been observed for a neutral defect [75].

II. PHONON ASSISTED AND PURE TUNNELLING

Here two models are explained, pure tunnelling and phonon-assisted tunnelling. These models are dominant in much high field regions ($> 10^8$ V m^{-1}).

The model indicating defects with a significant electron-lattice coupling, is phonon-assisted tunnelling. Owing to the electron-lattice coupling, a trapped electron can occupy a set of stationary quasi levels which are separated by an energy $\hbar\omega$, where $\hbar\omega$ is the phonon's energy. The coupling constant or Huang-Rhys factor (S) can be calculated as shown in Equation (2.19) [79]

$$S = \frac{\Delta E}{\hbar\omega}, \tag{2.19}$$

where ΔE presents the vibrational energy loss. The field enhanced emission rate due to phonon-assisted tunnelling which described by Pons [80] can be written as

$$e(F) = \Sigma_p \Pi_p \Gamma(\Delta_p)(1 - f_{1,p}). \tag{2.20}$$

Here Π_p is the probability of finding the electron at quasi level p, $\Gamma(\Delta_p)$ is the tunnelling probability for an electron at quasi level with the energy Δ_p above the ground state, and $(1 - f_{1,p})$ is the Fermi-Dirac probability of finding an empty state in a conduction band.

The other model which is used to describe phonon-assisted tunnelling was reported by Ganichev *et al.* [81]. This method defines phonon-assisted tunnelling with regard to the tunnelling time τ of an electron under the potential of the defect. The model considers both strong and weak electron-phonon coupling. The model reported by Ganichev for field enhanced emission is given by

$$e(F) = e_0 \exp\left(\frac{\tau_2^3 e^2 F^2}{3m^* \hbar}\right) \tag{2.21}$$

In this equation τ_2 is the tunnelling time of a free electron with zero kinetic energy under the potential curve of ionized impurity, *e* is the charge of an electron, *F* is the electric field strength and m^* is the effective mass of charge.

The tunnelling time can be written as shown in equation (2.22), where τ_1 is the tunnelling time under the potential curve for a bound electron and T is the temperature

$$\tau_2 = \frac{\hbar}{2k_B T} \mp \tau_1 \tag{2.22}$$

The minus and plus signs correspond to the case of weak and strong electron-phonon coupling, respectively. A comparison between the equations derived by Makram-Ebeid [79] and Ganichev [81] for field enhanced emission displays that the Ganichev model predicts a simple functional relationship between the emission rate and the electric field strength $\ln e(F) \propto F^2$. But the Pons [80] model (Equation 2.20) does not predict such a simple relationship between the emission rate and the electric field. In the Poole Frenkel model, the dependence of the emission rate dependence on electric field strength is $\ln e(F) \propto \sqrt{F}$, Therefore, an easy way to distinguish the Poole-Frenkel effect and phonon-assisted tunnelling is to plot the logarithm of emission rate against the F^2 and $\sqrt{F}$, and testing for a linear relationship [75], [82].

2.3 Deep -Level Transient Spectroscopy

In 1974, Lang [31] introduced the deep-level transient spectroscopy (DLTS) as a new technique for characterizing the electrical properties of deep levels in semiconductors. DLTS is essentially, a high frequency (typically 1 MHz) capacitance transient thermal scanning technique. The operation of DLTS relies on the correlation between concentration and characteristics of deep-level states and certain properties of a simple semiconductor device such as the capacitance of a reverse-biased Schottky diode. In the traditional (capactitance) DLTS measurements, the change in the capacitance of a Schottky diode is used to measure the change in the charge state of a deep level defect. One of the abilities of DLTS allows for the distinction between minority and majority

carrier traps. This technique may be used to determine the concentration, emission and capture rate, and other fundamental parameters of defects in semiconductors. By measuring the emission rate as a function of temperature, the enthalpy of ionization and the apparent capture cross-section of the defect may be determined (as described in section 2.2.4) and used to identify the defects.

2.3.1 Capacitance signal during DLTS

Figure 2.5 shows a typical simple circuit diagram for measuring any p-n junction, Schottky device or a MOS device. The depletion region width changes in accordance with the applied voltage across the metal-semiconductor junction. Because of the change in the depletion width, the observed capacitance also changes, which is attributed to the change in the number of free carriers on either side of the junction. These changes are caused by junction and diffusion capacitance. Under reverse bias, the change in the junction capacitance is dominant because of the depletion region width changing, but under significant forward bias, changes in diffusion capacitance are dominant because of changes in minority carrier concentration.

For a junction formed between a metal and *n*-type semiconductor, in the quiescent state of the system, there is no net flow of electrons over the junction, and hole densities in the depletion region are low. The density of filled traps, n_T , correlate with the total density of traps, N_T , as shown in Equation (2.23), where e_n is the electron emission rate and e_p is the hole emission rate [71]

$$e_p n_T = (e_n + e_p) N_T, \tag{2.23}$$

Or can be written in terms of the density of filled traps under a steady state

$$n_T = \left(\frac{e_n + e_p}{e_p} \right) N_T. \tag{2.24}$$

By changing the bias applied to the system, the total charge of the depletion region increases or decreases due and the capacitance changes.

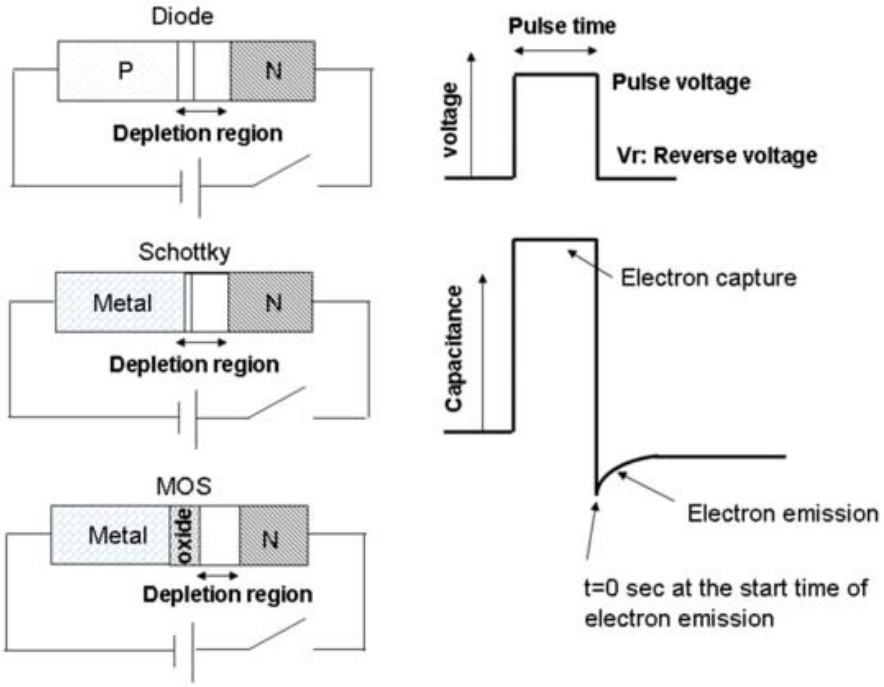

Figure 2.5: Diagram of the different simple devices that generate a capacitance signal used in DLTS [83].

Figure 2.6 shows the DLTS scan cycle which leads to the capacitance transient. Figure 2.6 (a) shows the Schottky diode in a quiescent state under reverse bias. During this time, the traps in the depletion region are empty. Figure 2.6 (b) displays that the filling pulse is utilized to decrease the reverse bias to zero bias, which leads to a decreasing depletion region and electrons can be captured by deep levels. The rate at which the density of filled traps increases can be written as [51]

$$\frac{dn_T}{dt} = c_n(N_T - n_T) \tag{2.25}$$

Equation 2.25 applies when the re-emission of electrons is neglected. Here c_n is the capture time constant of the defect for electrons. If the filling pulse is long enough ($t \geq \frac{1}{c_n}$), all traps will be filled and $n_T = N_T$.

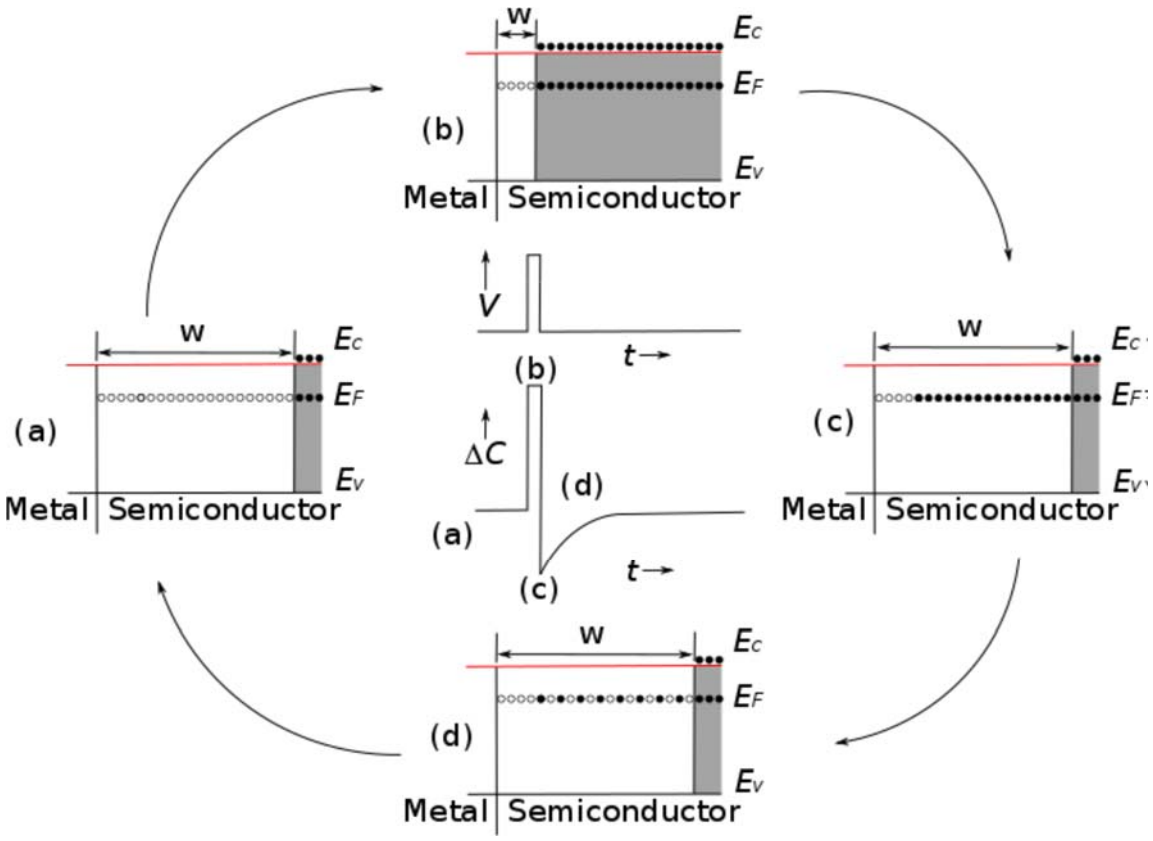

Figure 2.6: The basic procedure of a DLTS cycle and process of obtaining a DLTS spectrum (a) reverse bias, (b) filling pulse, (c) directly after removing pulse and (d) at time t after removing pulse [31].

As shown in Figure 2.6 (c), the bias is restored to its former level, after which the capacitance drops sharply to a minimum value, which happens due to the electrons trapped in the depletion region. When the system is returned to its quiescent reverse bias (V_R), the traps begin to thermally emit the trapped electrons and the density of filled traps changes with time. The emission rate is given by

$$\frac{dn_T}{dt} = e_p N_T - \left(e_n - e_p\right) n_T \,. \tag{2.26}$$

The solution of the equation is

$$n_T(t) = \frac{e_p}{e_n + e_p} N_T + \frac{e_n}{e_n + e_p} N_T e^{-\left(e_n - e_p\right)t}, \qquad t \geq 0 \tag{2.27}$$

an exponential decay with time constant

$$\tau = \frac{1}{e_n + e_p}. \tag{2.28}$$

In the case of electron emission where $e_n \gg e_p$, the solution reduces to

$$n_T(t) = N_T e^{(-e_n t)}. \tag{2.29}$$

In this case, it is possible to get a measure of the trap concentration, by using the amplitude of transient. The emission rate of electrons in terms of the time constant is

$$\tau = \frac{1}{e_n}. \tag{2.30}$$

Assuming an abrupt junction approximation, it is reasonable to assume that the capacitance of a Schottky diode is similar to that of a parallel plate capacitor

$$C = \frac{\varepsilon A}{w} \tag{2.31}$$

where A is the junction area and the depletion width is w

$$w = \sqrt{\frac{2\varepsilon(V_b - V)}{qN_d^*}}\,. \tag{2.32}$$

Here V_b is the built-in voltage, V is the applied bias, ε is the permittivity of the semiconductor and N_d^* is equal to $N_D - n_T$.

When $n_T \ll N_D$ the depletion region width doesn't change much during the emission process. Considering Equation 2.29, the emission of carriers can be defined by an exponential decay function. The capacitance can also be defined by an exponential decay,

$$C(t) = C_\infty + \Delta C e^{-\lambda t}\,. \tag{2.33}$$

With some manipulation of Equation (2.32), the capacitance under reverse bias can be written as shown below, where C_0 is the capacitance of the quiescent state at reverse bias V_R.

$$C(t) = C_0 - C_0 \frac{n_T}{2N_D} \tag{2.34}$$

Or it can be written as

$$C(t) = C_0 - C_0 \frac{N_T}{2N_D} e^{-\frac{t}{\tau}} \tag{2.35}$$

The capacitance can be changed by varying the applied reverse bias, and from this, the emission rate and concentration can be obtained according to these equations [84].

2.3.2 DLTS signal processing

The capacitance signal obtained during a DLTS measurement at a given temperature and reverse bias is given by Equation (2.35). The conventional DLTS technique detects emissions in a fixed rate window over a temperature range, and is the fundamental technique to determine DLTS signals. The significant feature of this method is that, by setting up the rate window, the system produces a signal when the time constant of the transient is in the given rate window. The rate window can be considered as a filter that only allows specific transients with a time constant equal to the centre of the window to be recorded by the system. Since the emission process is temperature dependent, at a given temperature only defects whose transients' time constants have this characteristic are detected. The results can be presented as a temperature dependent graph, where the amplitude of the transient corresponds with the maximum output of the detected signal. The earliest methods used to implement the time filter is a dual-gate boxcar average. This method requires the measurement of the capacitance at t_1 and t_2, and the DLTS signal $S(T)$ can be obtained by subtracting them [84].

$$S(T) = C(t_1) - C(t_2) = C_0 \frac{N_T}{2N_D}(e^{-\frac{t_1}{\tau}} - e^{-\frac{t_2}{\tau}}). \tag{2.36}$$

Figure 2.7 displays the capacitance transient and the signal obtained from the transient. As we see in Figure 2.7 the difference between the capacitances create a bell-shaped curve. According to Equation 2.36, at lower temperatures, the emission process is slow leading to slower change in capacitance from time t_1 to t_2 that resembles a straight line in the $C(T)$ vs time graph (Figure 2.7 a). From Equation 2.36, $S(T) = 0$, since the $C(t_1) = C(t_2)$. By increasing the temperature, however, the decay rate of the transient increases leading to an increased change in capacitance between t_1 and t_2, and therefore an increase in $S(T)$. At much higher temperature, the transient becomes very fast (i.e. time constant is short), so that $C(t_1) \approx C(t_2)$ and the change between two gates is small again, so $S(T)$ is small. Therefore, a maximum signal $S(T)_{\max}$ will occur for a transient with a time constant $\tau_{\max}$ between these two extremes. The value $\tau_{\max}$ can be calculated from Equation 2.36 by setting the derivative equal to zero

$$\tau_{\max} = \frac{t_1 - t_2}{\ln(\frac{t_1}{t_2})}. \tag{2.37}$$

By substituting Equation 2.37 into Equation 2.36 the $S_{\max}$ can be calculated as shown below:

$$S(T) = C_0 \frac{N_T}{2N_D}\left(\exp\left(\frac{-\ln(\frac{t_2}{t_1})}{\frac{t_2}{t_1}-1}\right) - \exp\left(\frac{\frac{t_2}{t_1}-\ln(\frac{t_2}{t_1})}{\frac{t_2}{t_1}-1}\right)\right). \tag{2.38}$$

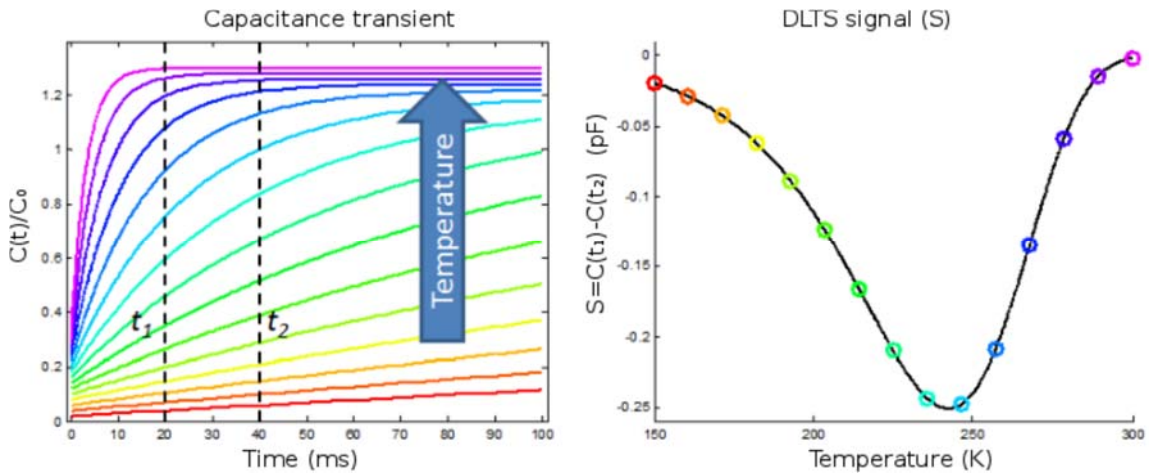

Figure 2.7: (A) Capacitance transient with a change in temperature, (B) the signal obtained from the transient [85].

From Equation (2.38) it is clear that $S_{\max}$ is proportional to the defect concentration, and the peak height is dependent on the ratio of t_1 and t_2 [84]. Information regarding the thermal activation energies can be obtained by varying the rate window. One of the disadvantages of conventional

DLTS is the overall achievable resolution of the technique, causing defects having similar emission properties to be difficult to distinguish by conventional DLTS.

2.3.3 Laplace DLTS (L-DLTS)

Laplace DLTS is a high resolution technique which was introduced by Dobaczewski *et al.* [36]. In this technique, the transient is recorded at a fixed temperature and analysed mathematically using a numerical inverse Laplace transform. A large number of transients have to be recorded and averaged to improve the signal to noise ratio (SNR), because the inversion algorithm is very sensitive to noise. L-DLTS works on the assumption that the observed transient consists of a range of emission rates

$$f(t) = \int_0^\infty F(s)e^{-st}ds\,. \tag{2.39}$$

where $f(t)$ is the recorded transient and $F(s)$ is the spectral density function. By applying an inverse Laplace transform to the function $f(t)$, the emission rates for the range of transients can be calculated. In practice, obtaining the Inverse Laplace transform of a real function accurately through numerical (algorithmic) methods is a long standing problem in signal processing, as reported by Dobaczewski *et al.* [36], that can be compounded by poor signal-to-noise ratio. Therefore to ensure the validity and the accuracy of the results, care must be taken to reduce the SNR. The SNR is, amongst others, affected by the quality of samples, the number of averages and the equipment. As explained by Dobaczewski *et al.* [86], results of the inverse Laplace transform of the signal are presented in the form of single or multiple peaks where they correspond with one or more exponential components in the signal. The absence of peaks in the final spectrum indicates a lack of or inability of the equipment to detect any exponential components in the measured signal. The area under the peaks in L-DLTS corresponds to the concentration of the defect.

2.4 Arrhenius' law

The reaction rate increases with increasing temperature. Svante Arrhenius proposed the Arrhenius equation in 1889 by using the Boltzmann distribution law and the activation energy to express activation energies

$$k = Ae^{-\frac{E_\alpha}{k_B T}} \tag{2.40}$$

Here k is the rate constant, A is the frequency factor, k_B is Boltzmann constant, T is the absolute temperature and E_α is the activation energy [87].

2.4.1 Annealing activation energy

During isothermal annealing at temperature *T*, the change in the concentration of defects over time period, $\frac{dN_T(t)}{dt}$, is a function of defects concentration at the time t, $f(N_T)$. Therefore, the relationship is written as

$$\frac{dN_T}{dt} = -Kf(N_T) \tag{2.41}$$

Here K is the annealing rate constant. If $f(N_T) = N_T$, the annealing kinetics are referred to as first order [88]. If we solve the Equation (2.41) by assuming that $f(N_T) = N_T$, then the concentration at any given time is

$$N_T(t) = N_T(0)e^{-k(T)t}. \tag{2.42}$$

Where $N_T(0)$ is the initial concentration before annealing, $k(T)$ is the temperature dependent annealing rate constant which is obtained from Equation (2.40) and t is the total annealing time [88].

Therefore, the defect concentration follows an exponential decay during the isothermal annealing procedure. Equation (2.42) can also be written as:

$$\ln\left(\frac{N_T(t)}{N_T(0)}\right) = -k(t)t\,, \tag{2.43}$$

Plotting $\ln(N_T(t)/N_T(0))$ as a function of time, results in a straight line with a negative gradient that is equivalent to the annealing rate constant of the defect at a specific temperature. Now, we can rewrite the Equation 2.40 as

$$\ln[k(T)] = \ln(A) - \frac{E_\alpha}{k_B T} \tag{2.44}$$

For a first-order reaction, by plotting $\ln[k(T)]$ versus T^{-1}, a linear plot will be obtained where the gradient of the line is equal to the annealing activation energy and the y-intercept of the line is the frequency factor. The activation energy is defined as the required energy to remove a single defect from the system. The frequency factor depends on the annealing mechanism, and if the activation energy is considered an energy barrier, it can be defined as the frequency of attempts to conquer this barrier. The frequency factor can be used to determine the process the defect undergoes during annealing, namely, diffusion, recombination, dislocation or complex formation [74].

2.4.2 The activation energy for electron emission

DLTS and L-DLTS are two most common methods used to determine the emission rates of defects in order to calculate their activation energy. For calculation by conventional DLTS, multiple scans across a wide temperature range with different emission rate windows is required [89]. Then, the

emission rate, e, can be calculated for each peak and plotted as $\log\left(\frac{e}{T^2}\right)$ vs $\frac{1}{T}$ from which a linear plot is obtained, as shown in Figure 2.8. From gradient and y-intercept, the activation energy and apparent capture cross-section can be obtained.

In L-DLTS, the activation energy is obtained from determining emission rates at different temperatures. These emission rates are processed as described previously. Laplace DLTS can separate defects with emission ratios ($\frac{e_1}{e_2}$) of around four, which is difficult to identify by conventional DLTS.

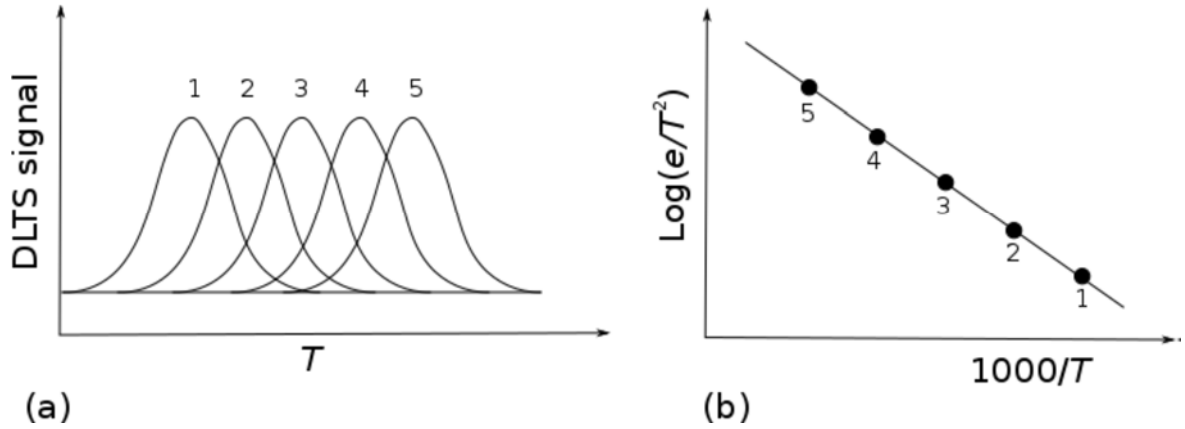

Figure 2.8: (a) DLTS spectra with different rate window conditions and (b) the Arrhenius plot obtained from the maxima [90].

2.5 Depth profiles

By using the Equation 2.38, the concentration of deep levels, N_T, can be calculated as a function of depth but this result is only an approximation [91]. When defects are deep in the band gap and a small reverse bias is used, the assumptions made may lead to significant errors. In order to obtain more accurate results, we consider an *n*-type semiconductor with the same type and concentration of shallow donors, N_D, as the previous one, at an energy level $e^{-1}E_T$ (here e is an absolute electronic charge) for N_T deep donors. By applying a quiescent reverse bias to the Schottky diode

the depletion layer region is $0 < z < w$ as shown in Figure 2.9. In the region $0 < z < w - \lambda$ the deep level is above the Fermi level that will eventually be empty. The depletion width is related to the capacitance

$$C = \frac{\varepsilon A}{w} \tag{2.45}$$

Here ε is the dielectric constant, $w - \lambda$ is the depth, at which the deep levels cross the bulk Fermi level $e^{-1}E_F$. From the equation below we can calculate λ [92].

$$\lambda = \left(\frac{2\varepsilon(E_F - E_T)}{e^2 N_D} \right)^{\frac{1}{2}}. \tag{2.46}$$

To profile the distribution of deep levels, the intended region has to be filled with electrons. It can be done experimentally by applying a forward bias V_+ that is -superimposed on an initial quiescent reverse bias ($V_p = V - V_+$). This leads to a temporary reduction of the depletion region width that lasts for the duration of the forward bias pulse. Figure 2.9 shows the depletion region width as a function of pulse height (voltage). When the applied pulse increases, the depletion width decreases, more defects fill and consequently the DLTS peak height increases too. For a Schottky diode with constant defect density, the correlation between the change in the depletion region width and the change in capacitance of the junction is linear. Although the depth resolution of the depth profile can, in principle, be increased by applying a smaller positive pulse, the ultimate resolution is limited by the Debye length [89], [92].

By applying the pulse, electrons will fill defects in the region $w_p - \lambda_p \le z \le w - \lambda$. The correlation between the two applied biases V (quiescent negative bias) and V_D (built in voltage) the concentrations N_D and N_T is given by

$$V + V_D = \int_0^{w-\lambda} N_T(z).zdz + \int_0^{w_0} N_D(z).zdz. \tag{2.47}$$

Here, w_p and λ_p are the values during pulse V for w and w_0 is the depletion width during pulse V_D . This charge distribution relaxes in time to

$$V + V_D = \int_0^{w-\lambda} N_T(z).zdz + \int_0^{w} N_D(z).zdz. \tag{2.48}$$

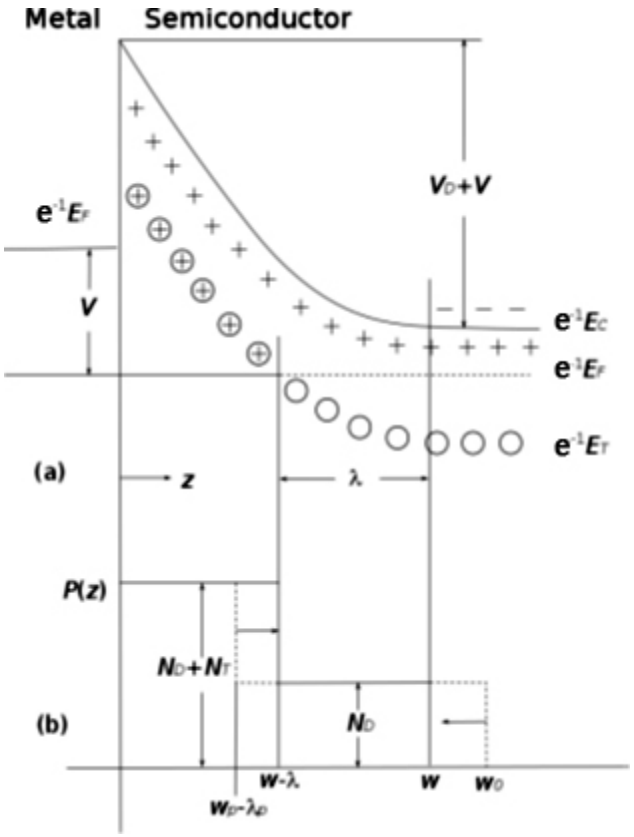

Figure 2.9: (a) Energy band diagram for a Schottky diode under a quiescent reverse bias. (b) The solid lines show the charge distribution at quiescence and dashed lines show the change in charge distribution after a pulse [92].

By combining Equations 2.47 and 2.48, it follows that

$$\int_0^{w_0} N_T(z).zdz = \int_{w_0-\lambda_0}^{w-\lambda} N_D(z).zdz \tag{2.49}$$

Supposing that $\Delta C(0)$ is smaller than C, the $N_D(z)$ slowly changes with position in the range of $w \le z \le w_0$ and $N_{T(s)}$ slowly changes with position in the range $w_p - \lambda_p \le z \le w - \lambda$ it follows from Equations 2.45 and 2.49 that

$$\frac{N_T(w_m - \lambda_m)}{N_D(w)} = \frac{1}{\left(\frac{w-\lambda}{w}\right)^2 - \left(\frac{w_p - \lambda_p}{w}\right)^2} \tag{2.50}$$

With

$$w_m - \lambda_m = \frac{1}{2}\left[(w - \lambda) - (w_p - \lambda_p)\right]. \tag{2.51}$$

This equation reduces to Equation 2.35 when $\frac{\lambda}{w} \langle\langle 1$ and $\frac{(w_p - \lambda_p)}{w} \langle\langle 1$. If Equation 2.35 is used instead of 2.51 for the case where $\frac{\lambda}{w} \langle\langle 1$ is not true, N_T reduces by a factor of $\left(1 - \frac{\lambda}{w}\right)^2 - \left(\frac{w_p}{w} - \frac{\lambda_p}{w}\right)^2$. So even for homogeneously doped samples, $N_T(z)$ appears to become lower as z approaches the surfaces for Equation 2.35 [92].

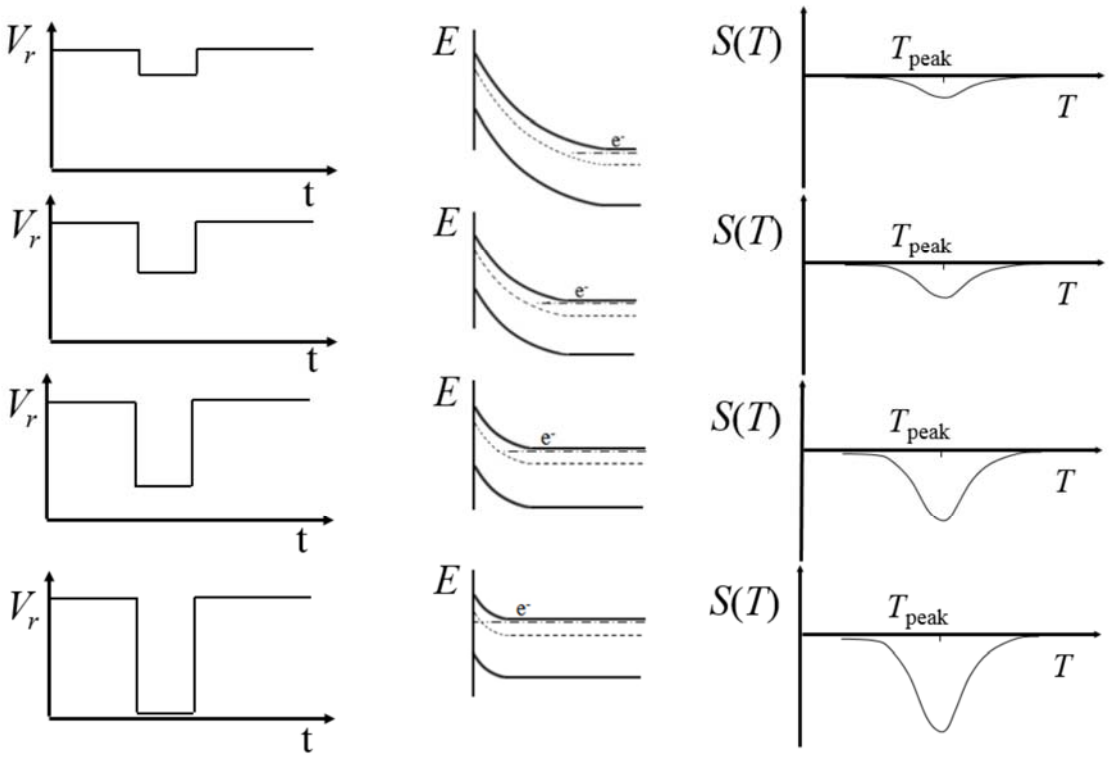

Figure 2.10: DLTS transient obtained during depth profiling. From left to right we have the pulse applied to the Schottky diode, its corresponding depletion width being filled and the signal obtained through DLTS and L-DLTS measurements [90].

3 EXPERIMENTAL TECHNIQUES

In this chapter, the SBD fabrication and experimental techniques are described. The samples used in this study are fabricated from silicon doped (*n*-type) GaAs with carrier densities of approximately 7.1×10^{14} cm^{-3}, 1.0×10^{15} cm^{-3}, 1.9×10^{15} cm^{-3} , 1.0×10^{16} cm^{-3} and 8.0×10^{16} cm^{-3}, that were MOVPE grown on n^{++} substrates. Due to a limited amount of 7.1×10^{14} cm^{-3} and 8.0×10^{16} cm^{-3} wafers, they were not used for all experiments.

3.1 Device fabrication

3.1.1 Cleaning procedure

The first stage in any semiconductor device fabrication is the cleaning and etching process. Proper cleaning procedures must be followed in order to clean the surface of the substrate from any foreign contaminants. It is also important to remove the oxide layer from the surface to ensure optimum contact between the surface of the metal and the semiconductor.

In order to ensure that no additional contaminants are introduced to the surface, all the glassware and tweezers that were used for each cleaning step were used exclusively for the cleaning of GaAs samples. The cleaning procedure was performed in three steps. The first step, called degreasing, was carried out to remove organic contaminants on the surface, and was performed as follows:

- Boiling in trichloroethylene for 5 minutes to dissolve and remove the contaminants.
- Boiling in isopropanol for 5 minutes to remove the trichloroethylene.
- The samples were rinsed in de-ionized water (18 MΩ cm) three consecutive times to remove isopropanol.

The second step was wet etching, which involved dipping the samples in a solution (described below to remove any surface states or dangling bonds.

- H_2O [100%]: H_2O_2 [50%]: NH_4OH [25%] with (100:1:3) volume ratio, for 60 seconds.

- The samples were rinsed in deionized water to remove the etching solution.

At room temperature, the etching rate for GaAs in the aforementioned solution is estimated to be 3000 Å/min [93].

The third and final step in this procedure was the removal of the remaining oxide layer using a diluted acidic solution:

- Dip in H_2O [100%]: HCl [70%] solution with volume ratio 1:1 for 1 minute.
- The samples were rinsed again in de-ionized water three consecutive times.
- The samples were consequently blow-dried using filtered nitrogen gas.

3.1.2 Ohmic contacts

The samples were rapidly placed in the vacuum chamber of a resistive-evaporation deposition system, after the cleaning and etching processes, in order to fabricate a multi-layered ohmic contact (Ni (5 nm), Au-Ge (145 nm), and Ni (50 nm)) on the back surface of each sample. Prior to the onset of the deposition process, the chamber pressure was lowered to approximately 1×10^{-6} mbar. Once the vacuum pressure was stabilized, deposition of the first layer commenced at a rate of 1 Å/s. The same process and conditions were applied for the deposition of the remaining two layers.

The fabricated ohmic contact was annealed at 450 °C for 2 minutes in an Ar-filled environment in order to alloy and lower the contact resistance.

3.1.3 Schottky contacts

The same cleaning procedure as described in section 3.1.1 was carried out for the fabrication of Schottky contacts, with the exception of the dipping in H_2O: H_2O_2: NH_4OH which was skipped. After the cleaning and etching process, the samples were placed into either the resistive deposition or the sputter deposition system. High purity Au was deposited through a metal mask, to make Au Schottky contacts. In the resistive evaporation system, the 0.6 mm diameter Schottky contacts were made by depositing 1200 Å Au at a rate of 1 Å/s on the front of the sample, while the vacuum remained at 1×10^{-6} mbar. In the sputter system, the deposition was carried out under RF power of

150 W in an Ar environment at 8×10^{-2} mbar with a DC bias of 580 V for 5 minutes. Figure 3.1 shows the front and the side views of a Schottky barrier diode (SBD) after fabrication.

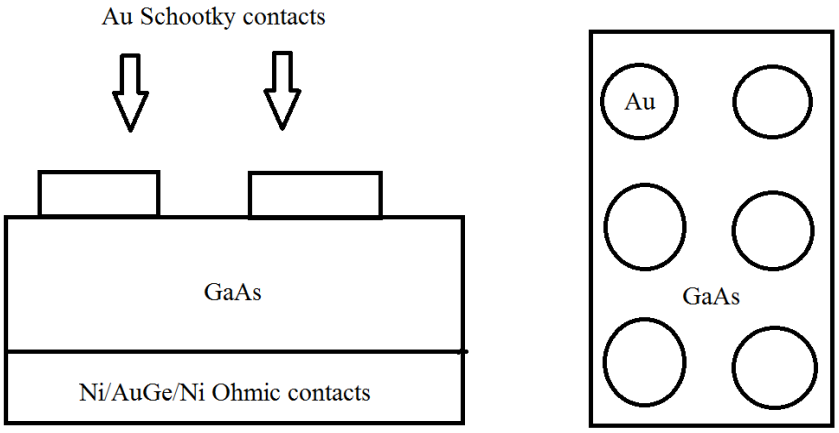

Figure 3.1: The Front and side views of the SBDs after fabrication.

3.1.4 Resistive evaporation (RE)

Figure 3.2 shows a schematic representation of the resistive-evaporation deposition (RE) system used in this study. RE is one of the techniques frequently utilized for metal deposition. This system consists of a glass bell jar, a mounting plate, multiple ceramic crucibles, a quartz crystal monitor housed within a chamber that is connected to a forepump and a diffusion pump that create the high vacuum within the chamber. The deposition process starts when a high electrical current is controllably applied to the crucible resulting in the crucible heating up until its temperature has risen close to the boiling point of the metal inside, thus heating up the metal until it starts evaporating under vacuum. The solid material (in this work, Ni, Au/Ge or Au) was used. As the evaporated metal particles contact the surfaces inside the chamber, including the surface of the sample, they begin to condense and a thin film is formed on the substrate. It is critical to keep the temperature of the sample as low as possible (close to room temperature) for this process to take place. Since defects in the sample can anneal out at high temperatures during the deposition, therefore, the sample holder is placed at a distance from the crucible and a small crucible is used to avoid excess heat in the system. During the deposition, a quartz crystal monitor recorded the

thickness of the deposited layers on the substrate. While the material is under evaporation, collisions with remnant gas occur inside the chamber, leading to loss of a fraction of the material and contamination of the layer. Therefore, for deposition, we required pressures in the order of 10^{-5} mbar or lower to minimize this loss.

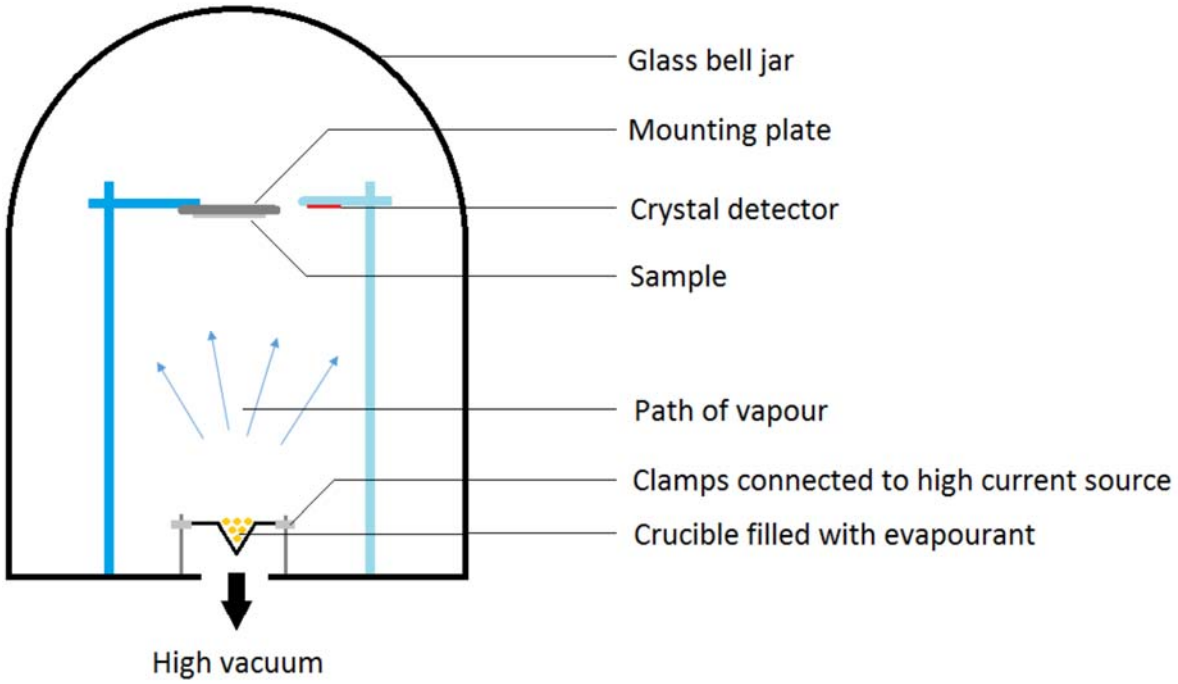

Figure 3.2: Schematic of the RE system [90].

3.1.5 Sputter deposition

One of the most important physical vapour deposition techniques used to deposit thin films onto the surfaces of materials is sputtering. The advantages of sputter deposition are: the capacity to deposit metals with a high melting point, stoichiometric deposition of compounds, high deposition rate and better adhesion than resistive deposition [34]. The process involves the creation of gaseous plasma that is then accelerated and collides with the source material to be deposited (target). The high energy collisions of ions with the target result in the ejection of particles in the form of neutral particles, individual atoms, molecules or clusters of atoms. The ejected particles will travel in a straight line until they collide with other particles or encounter a surface. Therefore, placing a

substrate in the path of these particles, results in a thin coat being formed on its surface. For creating the plasma, the vacuum chamber is filled with an inert gas and a negative voltage is applied to the target. Free electrons close to the surface of the target are accelerated by the electric field and ionize the gas. Once this process is cascaded, it creates the plasma in the chamber. The deposition occurs when the positively charged ions are accelerated towards the cathode, colliding with the surface of the target, causing release of material from the target and creation of more free electrons as they transfer their energy to the material. Different energy sources (RF, MW, and DC) are utilized to feed and maintain the plasma state as it transfers energy into the target and its surroundings.

In this work, a direct sputtering system configuration was used. The magnets in this system are located behind the target to form a magnetic field that traps the free electrons directly above the surface of the target. This placement has two advantages; in the first place, rejected free electrons from the target are prohibited from bombarding the surfaces, thereby avoiding overheating and structural damage to the sample. The second advantage is the curved path followed by the free electrons, as a result of their interaction with the magnetic field that leads to increasing the possibility of electron-gas collisions, which in turn increases the chance of ionization by several orders of magnitude. This leads to a significant increase of the rate at which target material is ejected and deposited onto the substrate [94], [95]. Figure 3.3 shows the schematic of the sputtering system.

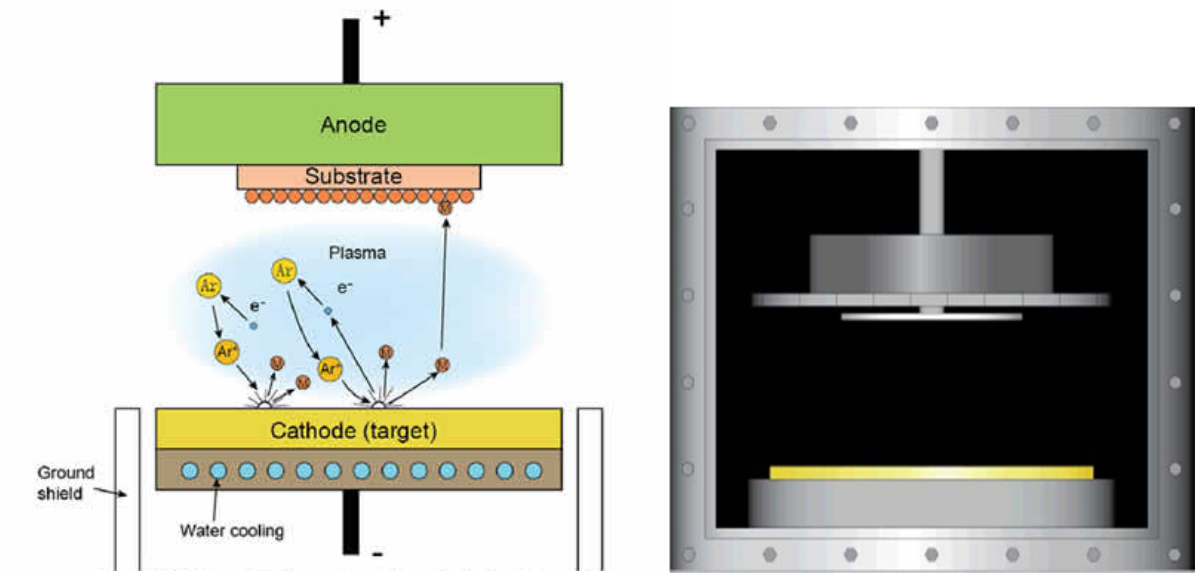

Figure 3.3: Schematic of sputter deposition system [95].

3.2 Defect introduction by beta particle source

The strontium source which we used for sample irradiation is disc-shaped, with a diameter of 8.4 mm and an activity of 36 mCi.cm^{-2}. The ^{90}Sr is a beta particle source with a half-life of 28.8 years and a decay process comprised of two stages. Firstly it decays to yttrium with a half-life of 64.1 h via emission of an electron with a maximum energy of 0.5 MeV. Secondly, the yttrium then decays to a stable isotope of zirconium via emission of an electron with a maximum energy of 2.27 MeV. The energy available is shared between the electron and an anti-neutrino. As a result, the ^{90}Sr source emits electrons within the energy range 100-2000 keV at a flux of 6.8×10^9 cm^{-2} s^{-1}.

The samples were exposed to the ^{90}Sr source by being placed underneath it. From the energy distribution of the source, as shown in Figure 3.4, it can be deduced that most of the emitted electrons have energies above the threshold energy of creation for point defects in GaAs by elastic collisions. (i.e. 220 keV for GaAs)

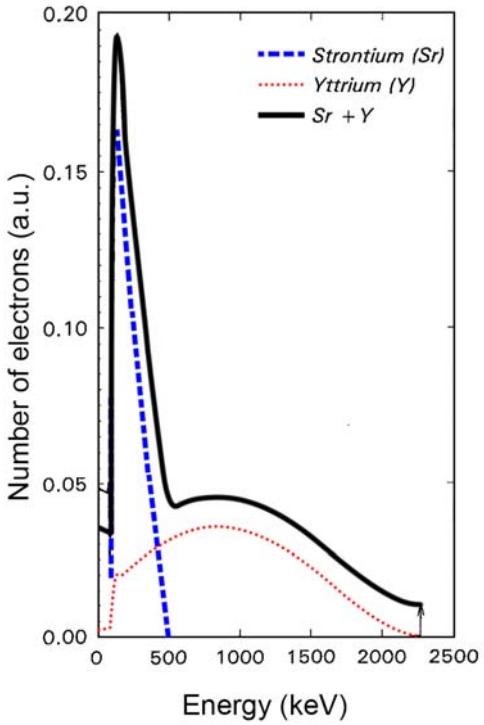

Figure 3.4: Energy distribution of electrons emitted by ^{90}Sr [96].

3.3 Instruments and techniques

3.3.1 *I-V* and *C-V* measurements

Current-Voltage (*I-V*) measurements provide significant information regarding the electrical properties and the quality of the metal-semiconductor junction. The important parameters obtained from these measurements are the Schottky barrier height (ϕ_{bIV}), series resistance (R_S) and the reverse leakage current measured at –V (usually –2 V in this study).

Capacitance-voltage (*C-V)* measurements provide information about the carrier density of the sample as well as the Schottky barrier height (ϕ_{bCV}) of the junction. In this study, *C-V* measurements were used to monitor the change in carrier density after irradiation and sputter deposition, which is important because it is used to obtain the accurate defect concentration by determining the free carrier density temperatures where the defects are observed.

According to the Schottky diode equation, the equation used in the *I-V* measurements is

$$I = I_0 \exp(eV / nkT) \tag{3.1}$$

In this equation I is the current density, I_0 is the saturation current density given by Equation 3.2 and n is the ideality factor.

$$I_0 = A^{**}T^2 \exp(-e\phi_b / kT) \tag{3.2}$$

where A^{**} is the Richardson constant and T is the temperature of the metal-semiconductor junction [13].

In *I-V* measurements, deviation from ideality occurs on account of the recombination and generation of carriers, image force lowering of the barrier, series resistance effects and tunnelling of carriers. In Figure 3.5 the *I-V* characteristic of ideal and non-ideal of SBDs and the process which is responsible for deviation are shown. Region (a) shows recombination-generation, (b) is the thermionic emission current region, (c) the high injection current region, (d) is dominated by the effect of series resistance region and (e) is dominated by the reverse leakage current due to recombination-generation and surface effects.

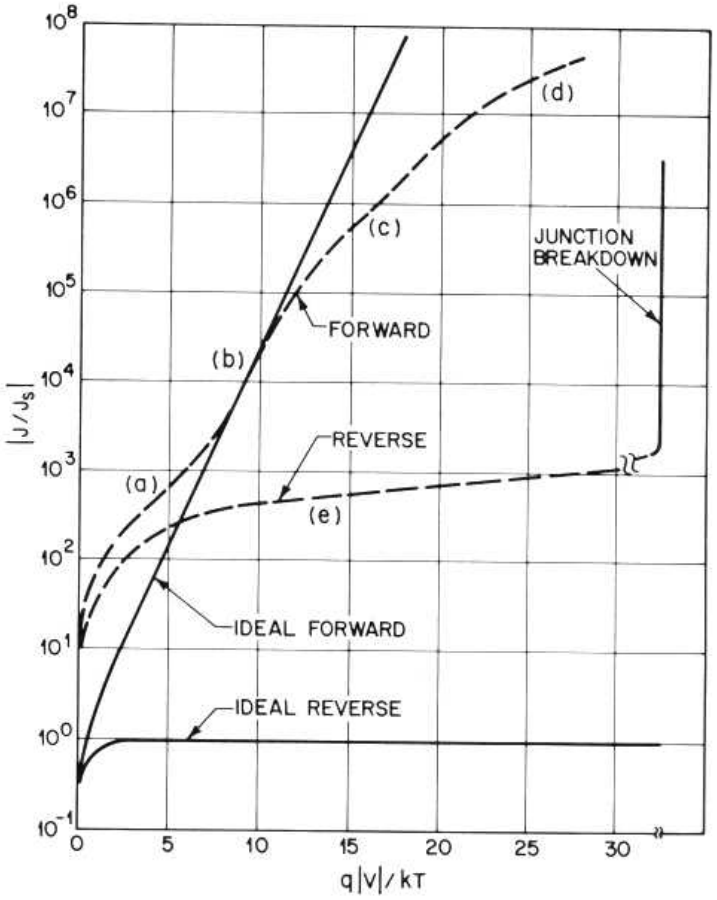

Figure 3.5: Current-Voltage characteristic of an ideal and non-ideal SBD [97].

The *I-V* system consists of an HP4140 pA meter/DC voltage source, with the lowest current measurement of 1.0×10^{-14} A and a probe station. Combined with this, is a *C-V* system comprising an HP 4192A LF Impedance analyser. Samples were placed on the probe station in a light-tight Faraday housing to prevent light and electromagnetic interference from reaching the sample. A LabVIEW^{TM} program was used to control the measurements. The results of the measurements were presented in the form of *I-V* and *C-V* plots from which diode parameters such as the ideality factor (n), barrier height (ϕ_{bIV}), device series resistance, carrier concentration (N_D), barrier height (ϕ_{bCV}) and built-in voltage (V_{bi}) were calculated. For gaining the capacitance, an AC voltage is superimposed on a DC bias in a desirable range.

3.3.2 DLTS setup

The DLTS system consists of:

- An insulating sapphire disk, is used to electrically insulate the sample from the cold finger of the cryostat while maintaining good thermal contact. The disk is soldered onto the top of the cold finger with a thin indium foil on top of it to provide electrical access to the ohmic contact on the sample.

- A Boonton model 7200 capacitance meter with a 100 mV AC ripple voltage, at 1 Mhz for measuring the capacitance of the Schottky diode.

- A Lakeshore 340 temperature controller used to set and stabilize the temperature of the sample using a PID control loop.

- A capacitance selection box, connected to the Boonton, which is used to reduce the measured capacitance of the junction by subtracting a constant value from it. This allows for changing the measurement scale within a range of 2 to 200 pF.

- A “Laplace card” used to convert the analogue signal received from the capacitance meter to digital data for processing by a PC. The card also produces produce the trigger pulses for the pulse generator.

- An Agilent 3320A 15 MHz wave form external generator used to provide the required quiescent reverse bias and the filling pulse.

- A vacuum pump used to insulate and prevent condensation.

- A closed-cycle helium cryostat capable of cooling the sample down to 10K.

The sample to be measured is mounted on a conducting stage (indium foil which is isolated by the sapphire disk from the system). Two probes connect the ohmic contact with the indium foil and Schottky contacts to the capacitance meter. If the ohmic contact is on the back of the sample, the connection between the contact and the probe can be made through the conducting stage. As explained above, all the instruments are controlled by a computer through the "Transient Processor" software. A block diagram of the DLTS (LDLTS) system is shown in Figure 3.6.

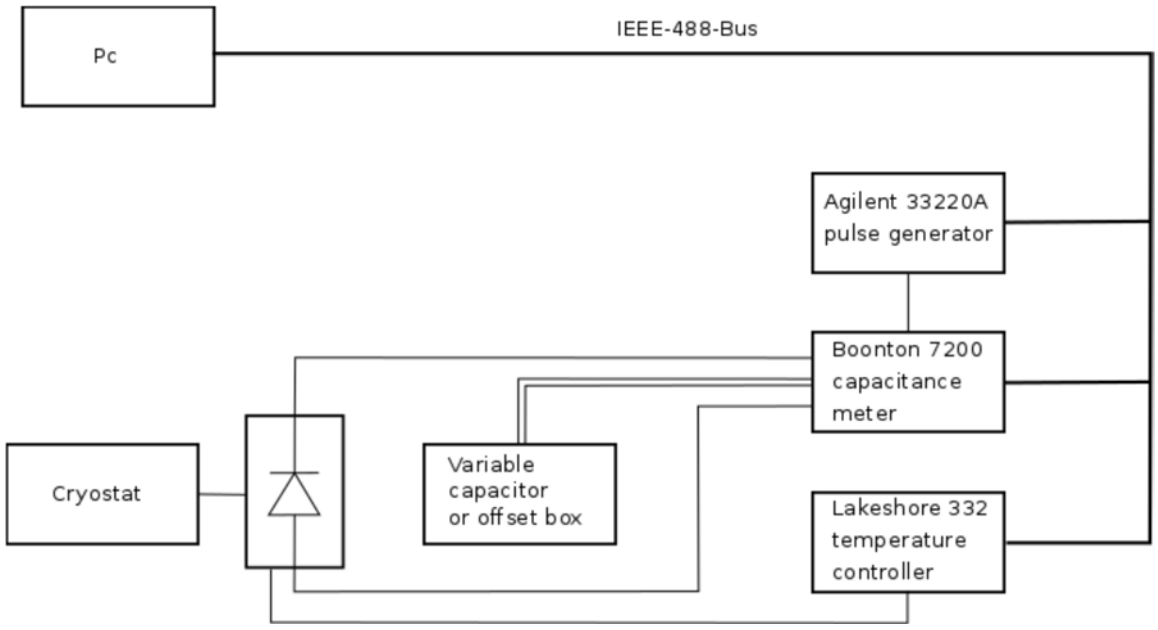

Figure 3.6: Block diagram of DLTS and L-DLTS measuring setup [90].

3.3.3 Laplace DLTS

Laplace DLTS is an isothermal technique and the accuracy of measurements is directly affected by slight variations in temperature.

For Laplace measurements, the sample is kept at a constant temperature, by the Laplace DLTS card the multiple capacitance transients were recorded and averaged to improve the SNR. Hereafter a numerical inverse Laplace transform was applied to the received signal to form the

emission rate spectrum. In Laplace DLTS, the manual input of regularization was used to determine how the inversion routine (Contin) split the broad peak into two or more than two peaks. Figure 3.7 shows a screenshot of the front panel for L-DLTS.

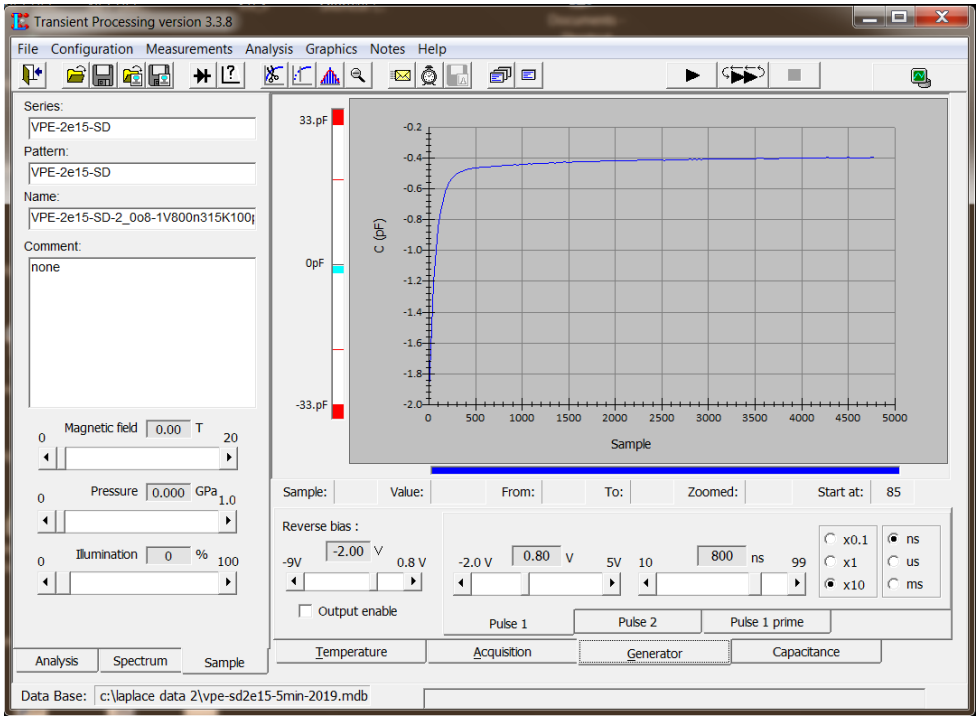

Figure 3.7: A screenshot of the front panel for Laplace DLTS.

4 RESULTS AND DISCUSSION

4.1 Introduction

In this chapter, firstly, the results of the fine structure of the E3 defect in *n*-type GaAs, which was introduced via electron irradiation will be discussed. The samples studied here were subjected to electron irradiation, during which each of them was irradiated for a specific time. The origins of the native defects, as well as those of defects introduced during sputter deposition, will be presented. *I-V* and *C-V* measurements, conventional and Laplace DLTS were done first. After that, the introduction rate, electric field dependence, depth profiles, real capture cross-section and annealing measurements were performed in order to characterize the electrical properties of these defects. Subsequently, the sputter deposition induced defects were characterised similarly. Then, for metastable defects, the introduction and removal rate kinetics were determined as well.

4.2 The characterisation of the fine structure of the E3 electron induced defect in GaAs

In 1977, Lang *et al*. established the effect of radiation-induced defects in GaAs for the first time [33]. From that time until now different measurements were carried out to investigate the nature and origin of the E3 defect, one of the main electron irradiation-induced defects in GaAs. Lang [33] and Farmer [98] proposed that the origin of the E3 is a V_{Ga}, based on their Hall measurements and DLTS results. On the other hand, Murawala *et al*. [99], according to theory and DLTS measurements, concluded that E3 is a V_{As}. Recently, by using density functional theory (DFT), using the local density approximation (LDA) and the Perdew-Burke-Ernzerhof (PBE) functional, Schultz [100] supported Murawala's conclusion. However, several authors suggested that the E3 defect consists of defect pairs: by using electron paramagnetic resonance (EPR), Pons *et al*. [101] and Stievenard *et al*.[102] found evidence for its being the $V_{Ga} - As_i$ while Von Bardeleben *et al*.[103], by using (EPR), deduced that it was the $As_{Ga} - V_{As}$ pair. The E3 was also proposed to be the antisite As_{Ga} by Schick *et al*. [104].

In this work, GaAs samples with three different silicon doping densities and free carrier densities of 7.1×10^{14} cm^{-3}, 1.9×10^{15} cm^{-3} and 1.0×10^{16} cm^{-3} were used for measurements.Tthe cleaning procedure was exactly the same as explained in Section 3.1.1 in Chapter 3. These samples were irradiated by beta (electron) radiation emanating from ^{90}Sr for different periods, depending on their doping densities.

4.2.1 *I-V* and *C-V* measurements of the E3 irradiation-induced defect

I-V and *C-V* measurements were performed before and after irradiation on *n*-type GaAs. Figure 4.1 (a) shows the results of the *I-V* measurements, under forward and reverse bias. The linearity of the log *I-V* plot for the unirradiated samples indicates the high quality of these n-GaAs based devices with an ideality factor of $n = 1.03$. Note that in the case of an ideal diode the TE current is dominant. After irradiation, the region of the plot between 0 to 0.2 V contained a bump which perturbs the linearity of the plot and therefore the ideality factor increased to $n = 1.13$ for $0.2 < V < 0.42$ and ideality factor is greater than 1.13 for $0.08 < V < 0.2$. The bump in the plot is caused by a generation-recombination current that is superimposed on the TE current. The generation-recombination current is introduced due to irradiation-induced defects. The reverse current of the irradiated samples is higher than the corresponding current in the unirradiated samples. The results are included in Table 4.1.

Figure 4.1 (b) displays the *C-V* plots of the samples, and the aim is to show the change in free carrier density as a result of electron irradiation. From the graph, it is clear that the line representing the samples before the irradiation process is steeper, which suggests an increase in free carrier density, $N_D = 1.0 \times 10^{15}$ cm^{-3} compared to $N_D = 1.9 \times 10^{15}$ cm^{-3} for irradiated samples.

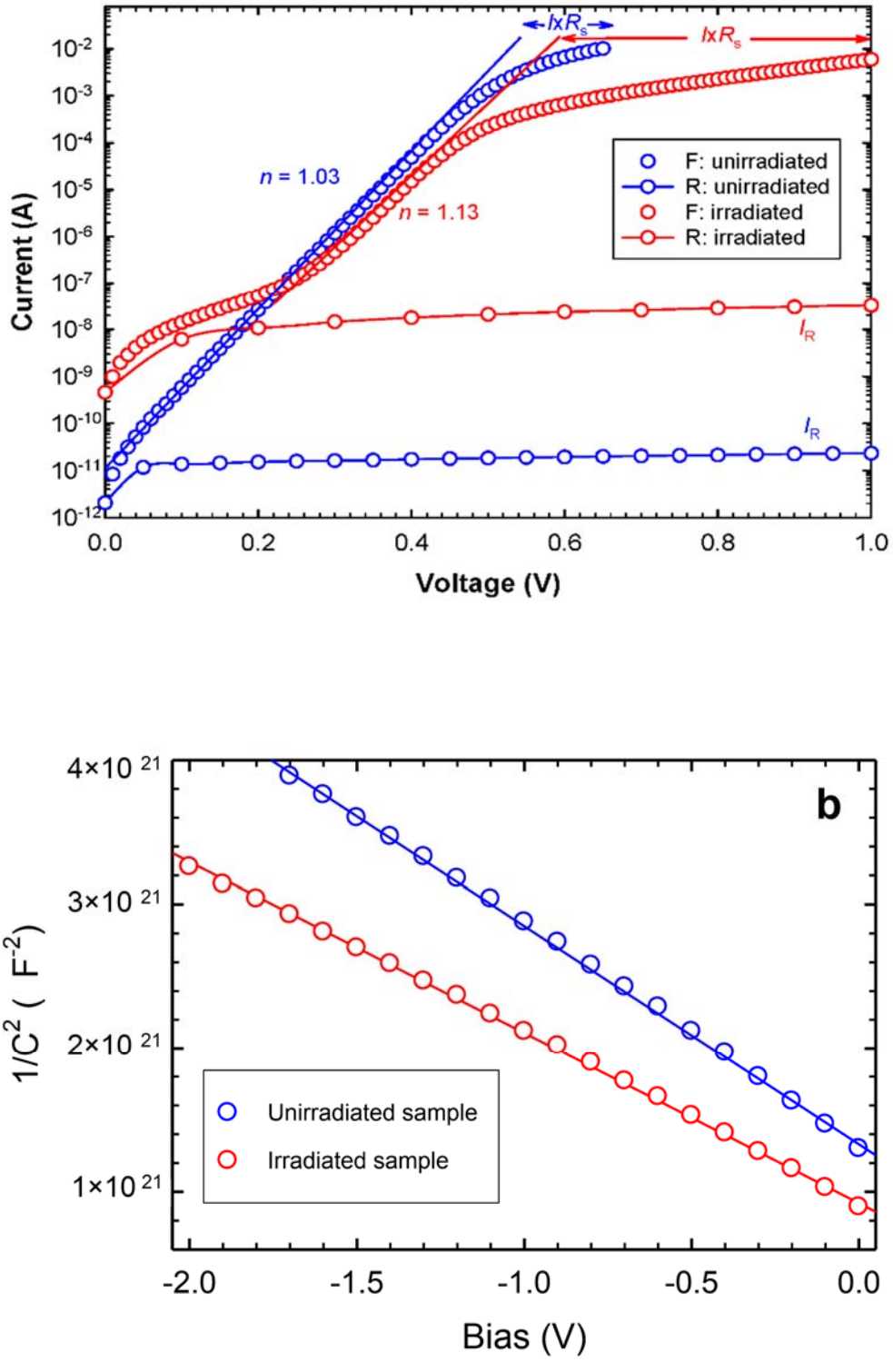

Figure 4.1: (a) *I-V* and (b) C^{-2}-*V* plots of GaAs samples with an initial carrier density of 1.0×10^{15} cm^{-3} before and after irradiation.

Table 4.1: The *I-V* and *C-V* characteristics of the Schottky diodes before and after electron irradiation.

Sample		n	ϕ_{bIV} (eV)	ϕ_{bCV} (eV)	$R_s(\Omega)$	Carrier concentration (cm^{-3})
1.0×10^{15} cm^{-3}	Unirradiated	1.03	0.86	0.95	3.1	1.0×10^{15}
	Irradiated	1.13	0.90	1.16	3.7	1.9×10^{15}
1.0×10^{16} cm^{-3}	Unirradiated	1.04	0.85	0.96	10.6	9.5×10^{15}
	Irradiated	1.15	0.96	1.05	11.2	1.0×10^{16}

4.2.2 Conventional and Laplace DLTS

Figure 4.2 displays the conventional DLTS and LDLTS spectra of GaAs samples with 3 different carrier densities (7.1×10^{14} cm^{-3}, 1.9×10^{15} cm^{-3} and 1.0×10^{16} cm^{-3}). The conventional DLTS spectrum was recorded over the temperature range 20 – 300 K as seen in Figure 1(a) and shows three prominent peaks: E1, E2 and E3, which are spaced far from each other in terms of energy levels. These peaks are observable at temperatures close to 30 K, 70 K and 200 K at a rate window of 80 per second. The Laplace DLTS spectrum of the E3 defect at 205 K is shown in Figure 1(b). From the conventional DLTS spectrum, it seems that the E3 is a single peak (although it is broad and with some asymmetry in the 1.0×10^{16} cm^{-3} doped GaAs). However, by using Laplace DLTS, it was clear that the E3 defect is comprised of 3 different individual components which we labelled E3a, E3b and E3c. In the DLTS spectra of the defects in material with three carrier densities are compared. The E3 peak in higher carrier density material was shifted to the left, and was asymmetric towards the lower temperature side. Additionally it was broader than in lower carrier density material. The Laplace DLTS spectra of the E3 defect for the different carrier density materials show that the relative amplitudes of the E3c peaks were enhanced in higher carrier density, material thereby explaining the shift and broadening observed in the conventional DLTS spectrum.

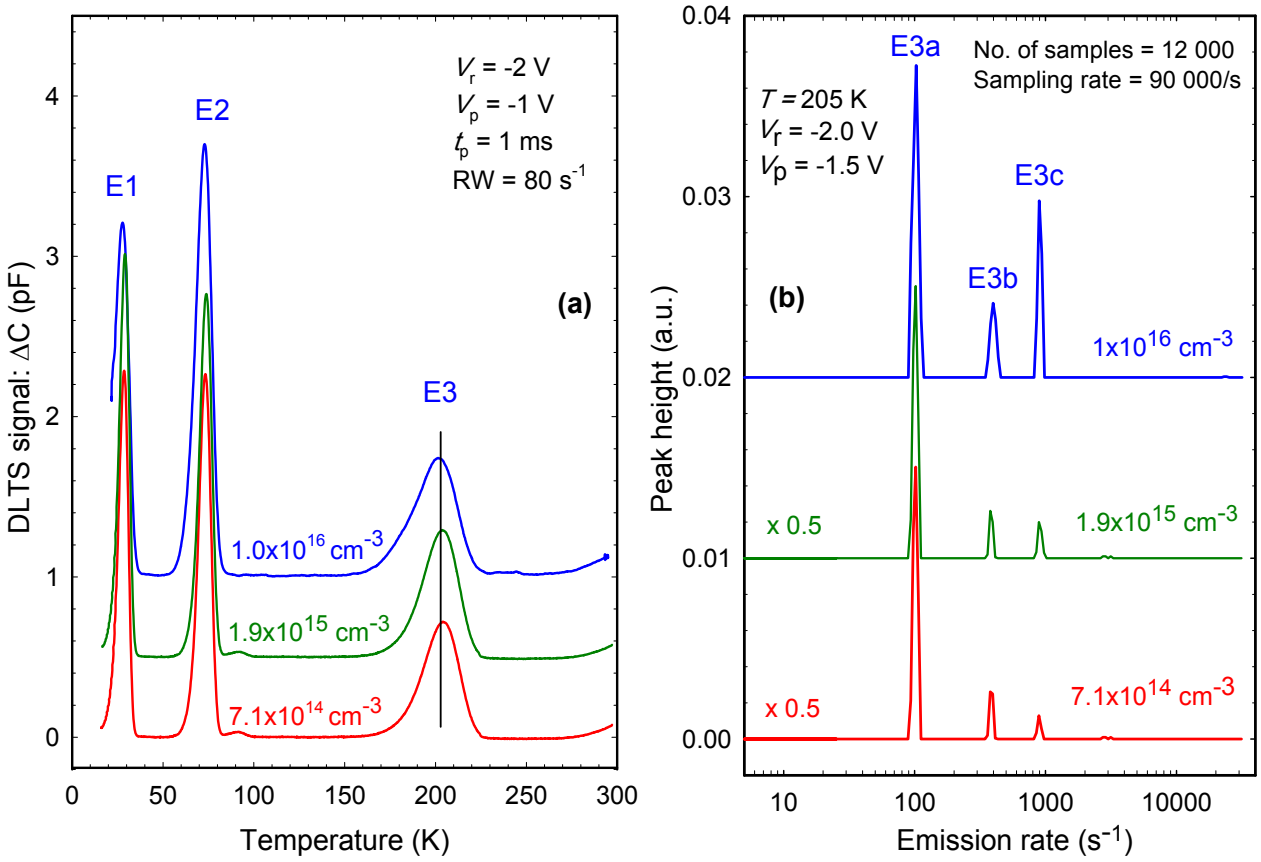

Figure 4.2: (a) conventional DLTS and (b) Laplace- spectra of the E3 defect in n-GaAs with three different carrier densities: 7.1×10^{14} cm^{-3}, 1.9×10^{15} cm^{-3} and 1.0×10^{16} cm^{-3}.

Figure 4.3 demonstrates the Laplace DLTS spectra's dependence on temperature. The measurements were done for 2 samples with different carrier densities, (1.9×10^{15} cm^{-3} and 1.0×10^{16} cm^{-3}) at 199, 205 and 211 K. All three peaks shifted together to the right in an orderly manner when the temperature was raised in both samples, indicating that the splitting of the defect into three components was reliable.

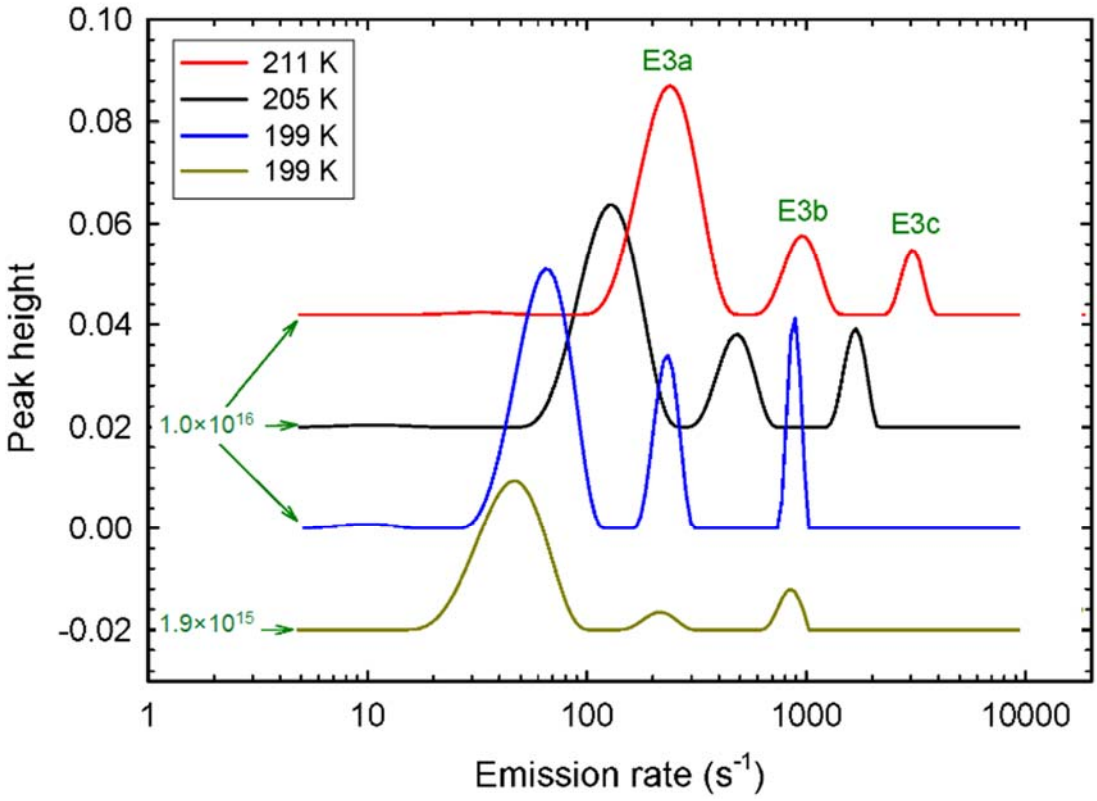

Figure 4.3: The shift in the activation energy of the three constituent peaks as a result of changes in temperature in 1.9×10^{15} cm^{-3} doped GaAs. The spectrum at 199 K in 1.0×10^{16} cm^{-3} doped material is shown as well.

4.2.3 Arrhenius plots

After DLTS and Laplace measurements Arrhenius plots where made to check the activation energies and obtain apparent capture cross-sections. Arrhenius plots of 3 samples with different carrier densities (7.1×10^{14}, 1.9×10^{15} and 1.0×10^{16} cm^{-3}) for the defects E3a, E3b and E3c are shown in Figure 4.4. The Arrhenius plots show a high degree of linearity and the activation energy decreased with increasing free carrier density, i.e. for E3a activation energies of 0.38, 0.37 and 0.36 eV were found for carrier densities of 7.1×10^{14} cm^{-3}, 1.9×10^{15} cm^{-3} and 1.0×10^{16} cm^{-3}, respectively. However, the activation energies of E3b and E3c in the 7.1×10^{14} cm^{-3} doped material have a $\pm$ 0.01 eV error bar because of the lower concentration of these defects compared to the same defect in the higher carrier density GaAs. The properties of the three defects are listed in Table 4.2.

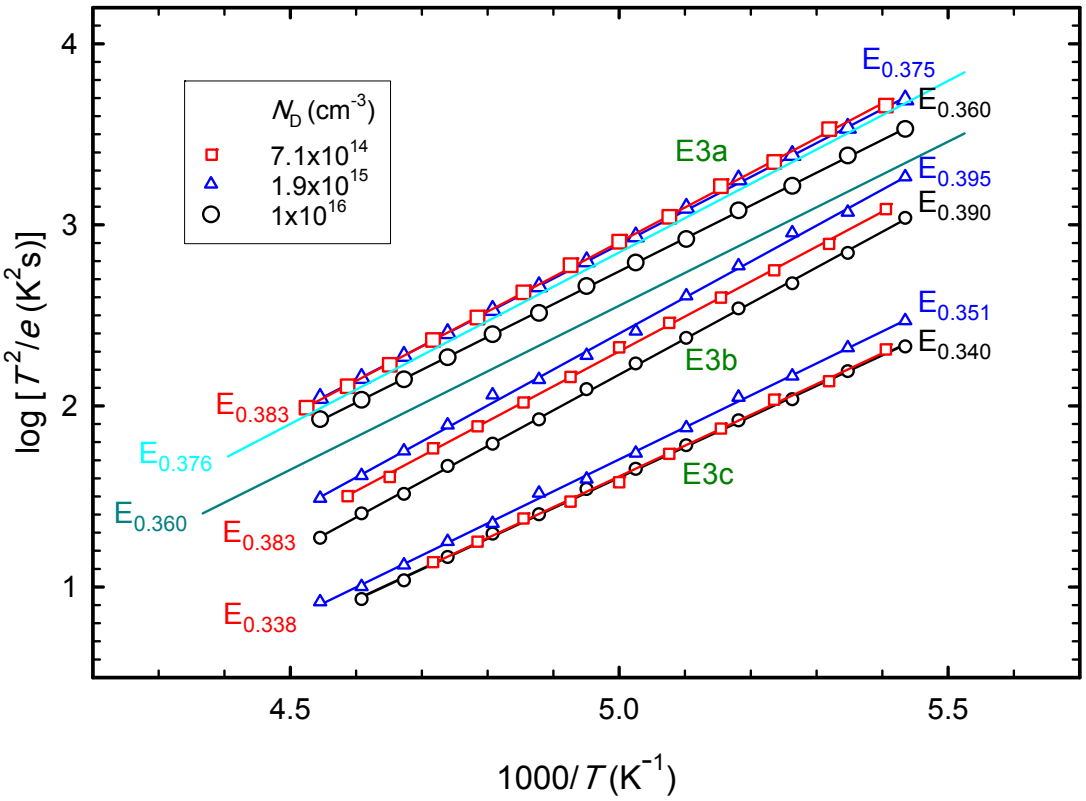

Figure 4.4: Arrhenius plots of the E3 and its three components in GaAs for 3 different carrier densities. The solid line without symbols is for conventional DLTS scans. The subscripts beneath the E labels are the DLTS activation energies in eV determined from the Arrhenius plots. Note that the error bars for the E3b and E3c for the 7.1×10^{14} cm^{-3} doped material are ± 0.01 eV because these defects are present in very low concentrations compared to the defects in the 1.0×10^{16} cm^{-3} doped GaAs.

Table 4.2: Electronic properties of the E3 defect and its components in GaAs with a doping density of 7.1×10^{14} cm^{-3} , 1.9×10^{15} cm^{-3} and 1.0×10^{16} cm^{-3}.

Defect	E_α (eV)	$\sigma_{n,a}$ (cm^2)	σ_n (cm^2)	Defect ID[ǂ]
E3	0.376[†] 0.360[*] 0.300 [101] 0.375 [105] 0.390 [106]	4.1×10^{-14}[†] 3.2×10^{-14} [*] 6.2×10^{-15} [101] 1.3×10^{-14} [105] 6.0×10^{-14} [106]	--------	-------
E3a	0.380[**] 0.375[†] 0.360[*]	4.7×10^{-14} [**] 2.9×10^{-14} [†] 2.1×10^{-14} [*]	3.0×10^{-16} [**] (205K) 1.0×10^{-16} [†] (205K) 3.1×10^{-17} [*] (205 K)	V_{As}
E3b	0.383[**] 0.395[†] 0.390[*]	2.1×10^{-13} [**] 3.4×10^{-13} [†] 4.8×10^{-13} [*]	----------	As_i
E3c	0.338[**] 0.351[†] 0.340[*]	7.7×10^{-14} [**] 1.3×10^{-13} [†] 6.8×10^{-14} [*]	----------	V_{Ga}-Si_{Ga}

[**]This study, measured in material with a free carrier density of 7.1×10^{14} cm^{-3}
[†]This study, measured in material with a free carrier density of 1.9×10^{15} cm^{-3}
[*]This study, measured in material with a free carrier density of 1.0×10^{16} cm^{-3}
[ǂ]The defect id discussed later in the summary section.

Note: Here E_α is the activation energy, $\sigma_{n,a}$ is the apparent capture cross section and σ_n is the real capture cross section.

4.2.4 Introduction rate of E3a and metastability of E3c

The introduction rate measurements were done to investigate the E3 defects' dependence on the Si dopant. We measured the main component, E3a, for 3 different carrier densities as function of electron fluence, as shown in Figure 4.5. (Note that E3b and E3c components for the lower doping density GaAs were too small to allow for an accurate measurement of their introduction rates as a function for doping density). From the results, we obtained that the introduction rate was the same for all the free carrier densities. This indicates that the E3a defect does not involve a dopant atom (Si). The introduction rate of the E3a in our samples was 0.42 cm^{-1}, which agrees with the value of 0.4 cm^{-1} found by Pons [101].

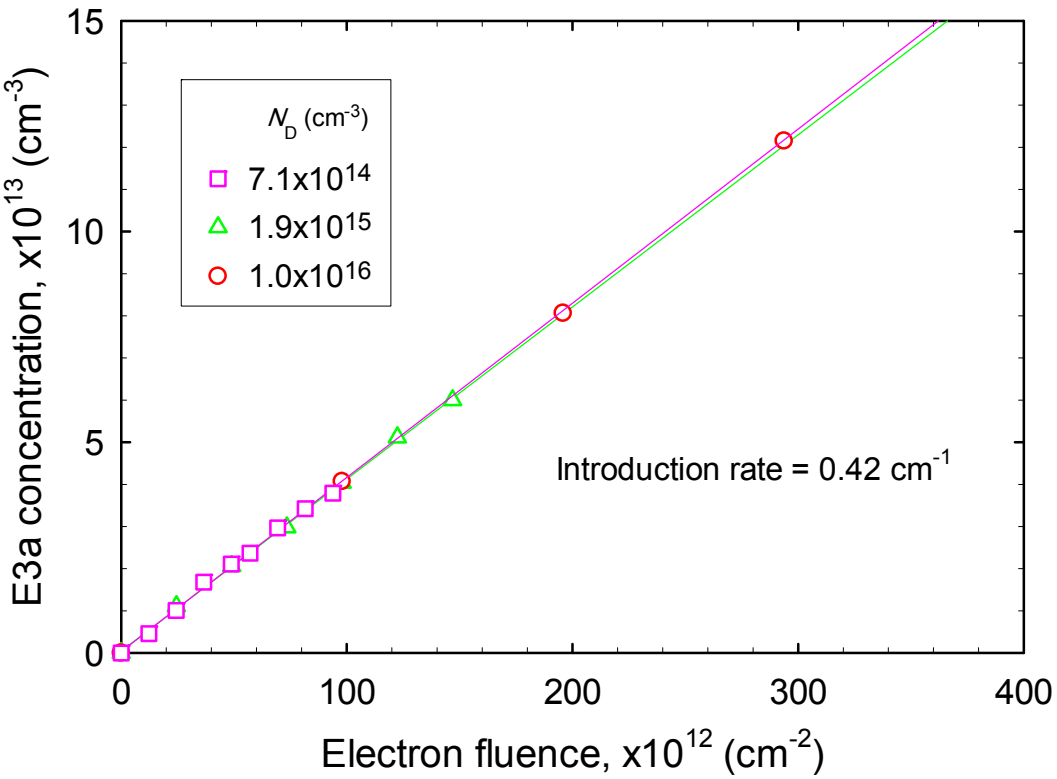

Figure 4.5: Concentration of the E3a in GaAs as a function of electron fluence from a ^{90}Sr radionuclide at 200 K, with pulses $V_r = -2$ V and $V_p = 0$ V.

In order to investigate possible metastability of defects, the sample was measured before and after subjecting the diode to minority carrier injection pulses (3 V forward bias) at low temperatures (90

– 120 K). Laplace DLTS spectra of samples with different carrier densities are shown in Figure 4.6. Three different spectra are shown: before injection, after injection and subtracted from each other for each carrier density. First of all, from the graphs we see that the concentration of the E3 defect increased with increasing carrier density. Next, before injection, the spectrum consisted of all 3 components of the E3 defect. However, after injection, the E3c was reversibly removed and only the E3a and E3b were observable in the spectrum. For the re-introduction of the E3c, the sample was heated to above 160 K under zero bias. The subtracted spectrum shows only the E3c. These processes were reproducible and indicate that the E3c is metastable. This metastable phenomenon has been observed previously [107], but at the time it was not realized that E3 is not a single peak because it was before the existence of Laplace DLTS.

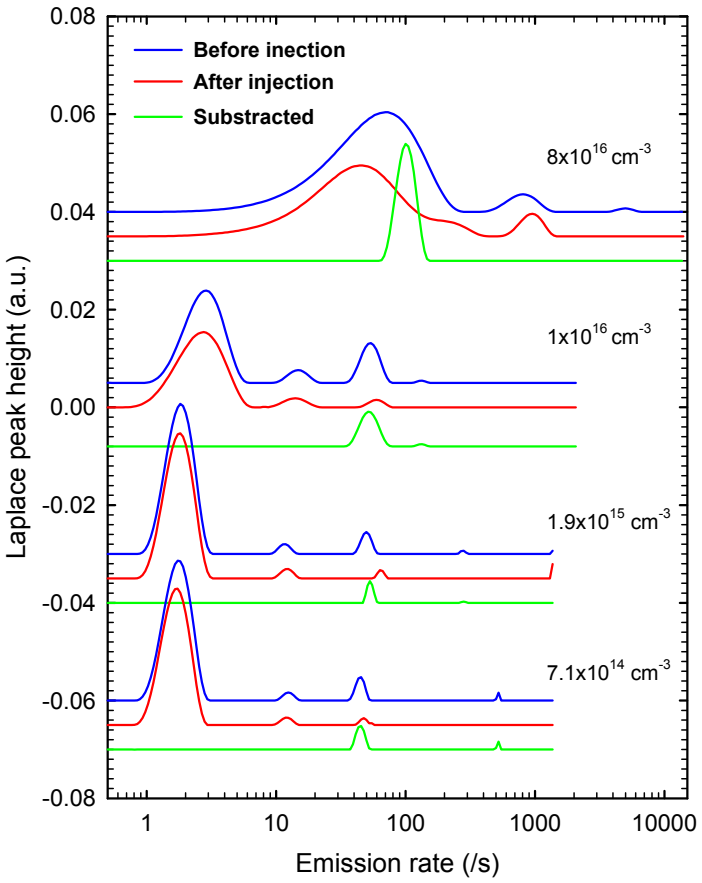

Figure 4.6: Laplace DLTS spectra of electron-irradiated n-GaAs with four different carrier densities before and after carrier injection. Spectra were recorded at 200 K by applying a reverse bias of -2 V and a filling pulse amplitude of 2 V.

4.2.5 Electric field dependence

The electric field dependence of the E3a is displayed in Figure 4.7. These measurements were done for 3 different carrier densities to distinguish between Poole-Frenkel (emission rate proportional to the square root of the electric field) and phonon-assisted tunnelling (emission rate proportional to the square of the field) as described in Section 2.2.5. According to Figure 4.7, it is clear that the field enhanced emission of carriers is best described via phonon-assisted tunnelling, and applies to all three carrier densities.

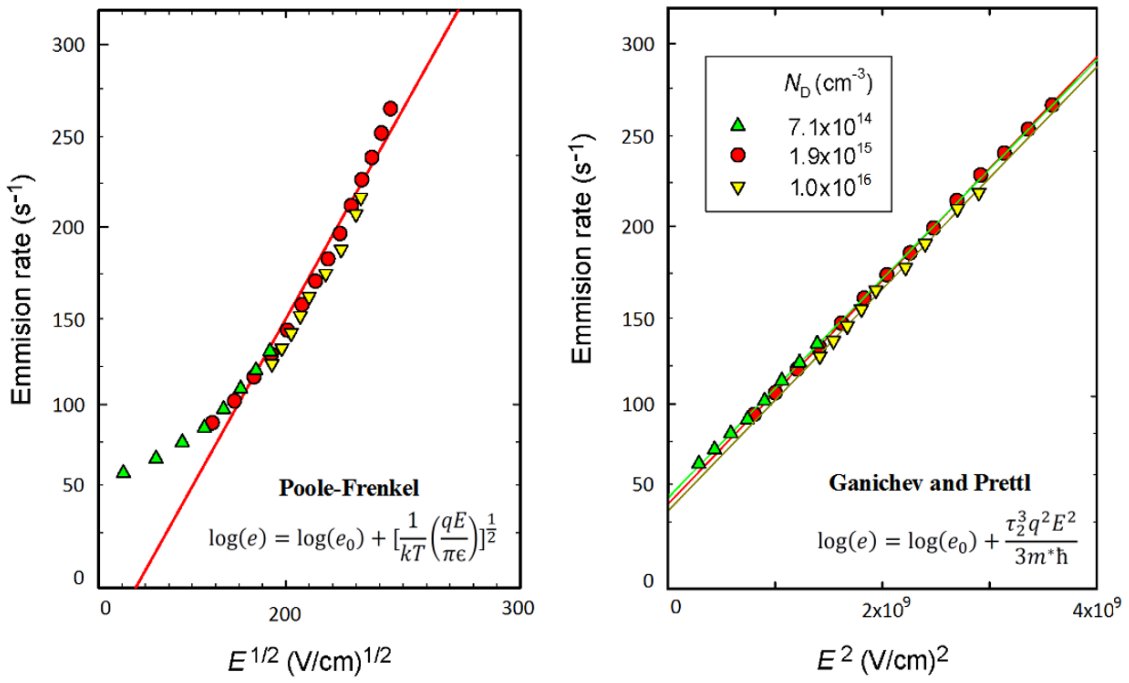

Figure 4.7: Electric field dependence of the E3a defect in GaAs for different carrier densities.

The graphs of emission rate vs. the square of the electric field for different temperatures (200 K, 205 K, 210 K, 215 K and 220 K) and the tunnelling time as a function of 1000/T are shown in Figure 4.8. The model by Ganichev and Prettl describes the phonon-assisted tunnelling in terms of the tunnelling time of an electron through the potential well of the defect as explained in Section 2.2.5. By increasing temperature, emission rate increased, however, the dependence of the

emission rate on the electric field did not change. We calculated the tunnelling time according to this model and Figure 4.8 (a), and it was found to be given by

$$\tau_2 = \frac{81000}{T} + 234\,(\text{fs}) \tag{4.1}$$

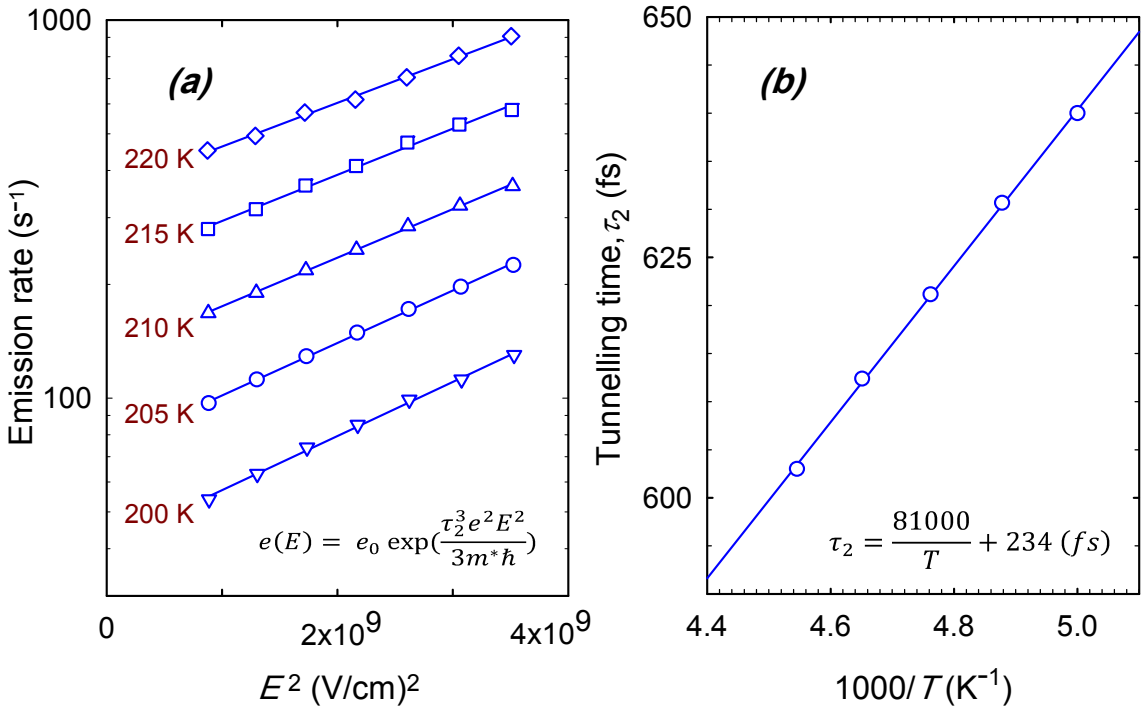

Figure 4.8: Tunnelling time vs. 1000/T for the E3a. The equation of the regression line is shown in the legend.

4.2.6 Capture cross-section

The true capture cross-section measurements of E3a were performed for two different carrier densities, 1.9×10^{15} and 1×10^{16} cm^{-3}, as shown in Figure 4.9. The capture cross-section of these samples was measured by measuring DLTS peak amplitude as a function of filling pulse width at

different temperatures. The DLTS signal after application of a filling pulse of length t_p, is described by the following equation [108]

$$S(t_p) = S_{\text{inf}}\left[1 - e^{\left(\frac{t_p}{\tau_c}\right)}\right] \tag{4.2}$$

In this equation, S_{inf} is the magnitude of the DLTS signal observed after applying a filling pulse sufficiently long to fill all the defects, and τ_c is the time constant of the capture process given by

$$\tau_c = \sigma n \nu_{th} \tag{4.3}$$

where σ is the capture cross-section, n is the free carrier density and ν_{th} is the thermal velocity of the carriers [108]. It follows that σ may be determined from the slope of the plot shown in Figure 4.9.

$$\sigma = 2.3 \text{ slope} / n\nu_{th} \tag{4.4}$$

Calculations using Equation 4.4, with experimentally determined slopes and values of n, show that the capture cross-section for material with a free carrier concentration of 1.0×10^{16} cm^{-3} is approximately a factor of three lower than that with 1.9×10^{15} cm^{-3} namely 3.1×10^{-17} cm^2 *vs.* 1×10^{-16} cm^2, respectively.

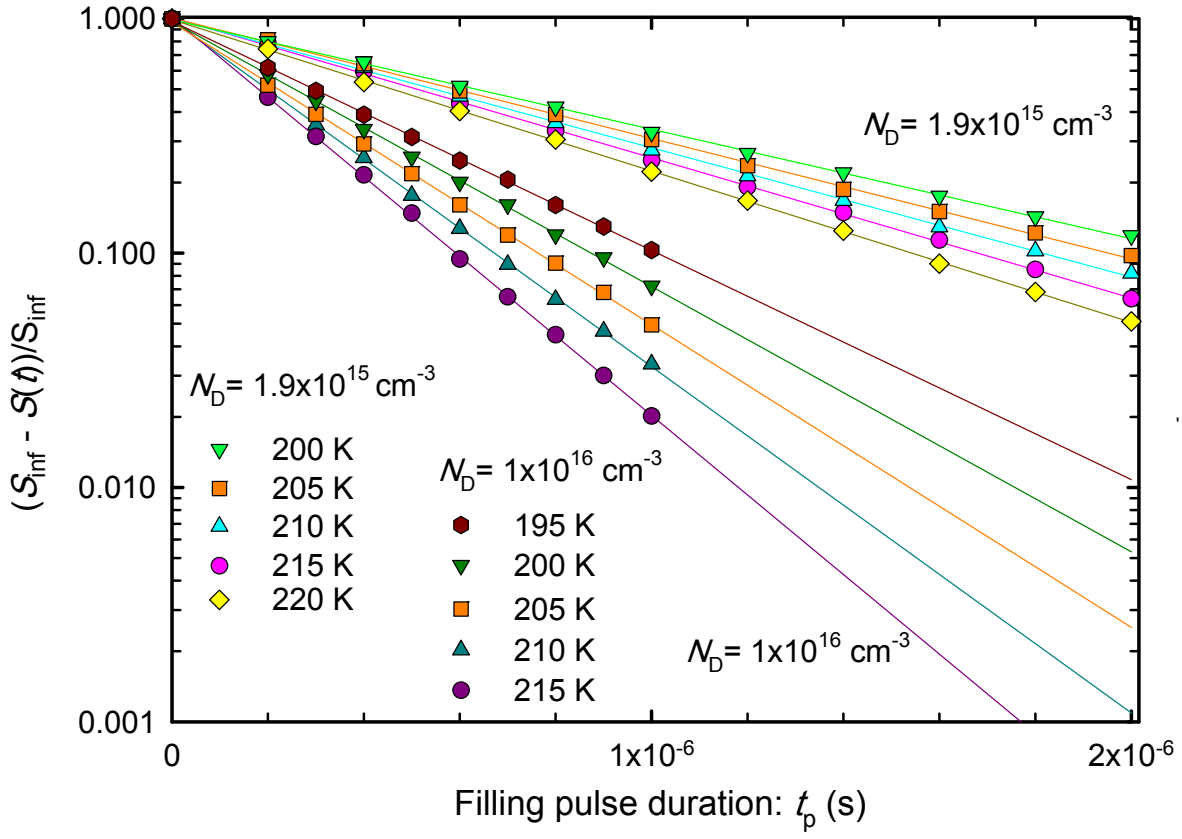

Figure 4.9: Determination of the capture cross-section of E3a in GaAs for $N_D = 1.9\times10^{15}$ cm^{-3} and $N_D = 1.0\times10^{16}$ cm^{-3}.

The temperature dependence of the capture cross-section may be explained by the existence of a capture barrier, ΔE, so that the capture cross-section as a function of the temperature is given by

$$\sigma(T) = \sigma_\infty e^{\frac{-\Delta E}{kT}} \tag{4.5}$$

where k is the Boltzmann constant, T is the temperature and σ_∞ is the high temperature limit capture cross-section. The capture cross-section for samples with a carrier density of 1×10^{16} cm^{-3} and 1.9×10^{15} cm^{-3} were measured at different temperatures and are used in Figure 4.10 to calculate

the capture barriers. As seen in Figure 4.10, the capture barrier (applying Equation (4.5)) for 1.9×10^{15} cm^{-3} is 0.023 eV and for 1×10^{16} cm^{-3} it is 0.039 eV. The high temperature limit capture cross-section (σ_∞) was 6.76×10^{-15} cm^2 and 5.24×10^{-15} cm^2 respectively for the 1.9×10^{15} cm^{-3} and 1×10^{16} cm^{-3} doped material. The carrier dependence might be explained by an Auger process, although the carrier concentration is rather low for Auger processes to be significant. According to Mitonneau *et al.* [109] the capture cross section of the 1.9×10^{15} cm^{-3} sample is in the range expected for multiphonon emission (MPE) mechanism and for 1.0×10^{16} cm^{-3} sample is in the range expected for a recombination centre.

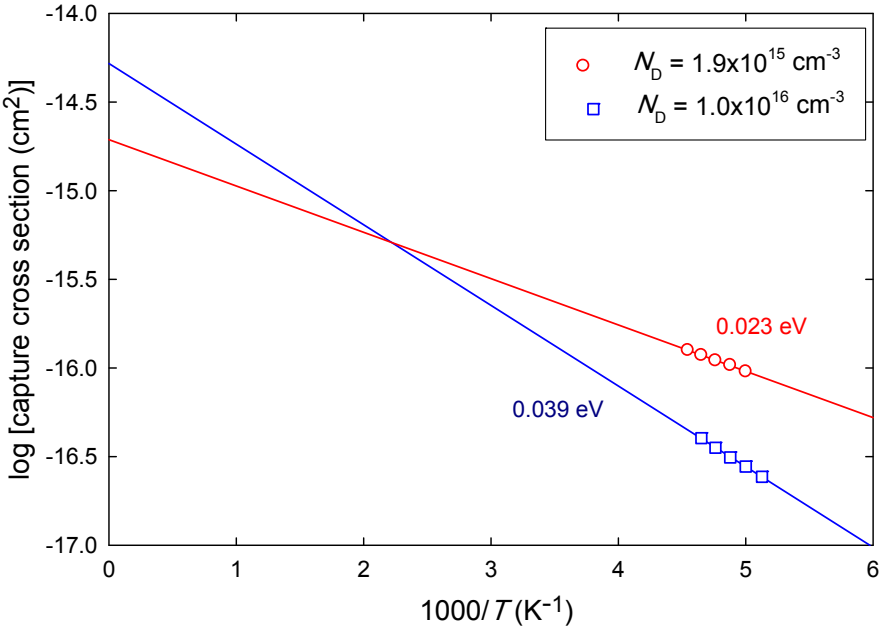

Figure 4.10: Arrhenius plots for the determination of the capture barriers of the E3a in a GaAs for $N_D = 1.9\times10^{15}$ cm^{-3} and $N_D = 1.0\times10^{16}$ cm^{-3}.

4.2.7 Annealing measurements

Figure 4.11 demonstrates the effect of annealing on the E3 defect. The annealing measurements were done for the sample with a carrier density 1.0×10^{16} cm^{-3}. As can be seen, the E3b defect annealed out before the other two at 500 K. E3a and E3c annealed out simultaneously at 525 K. This indicates that the E3b defect is structurally different from the others.

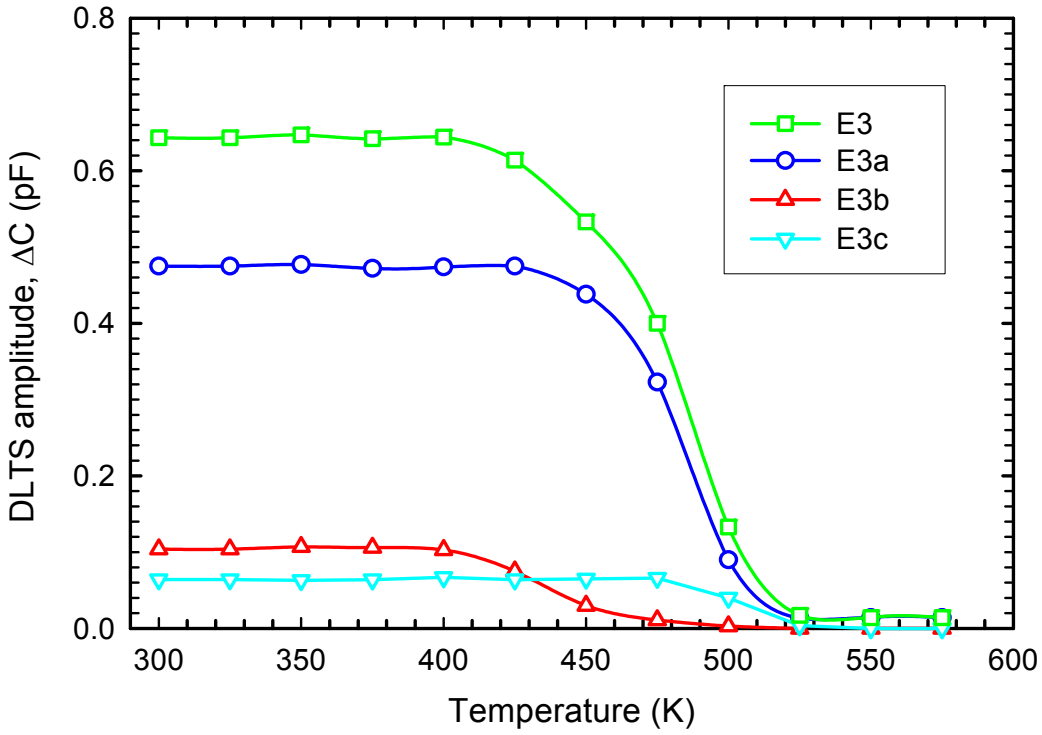

Figure 4.11: Isochronal annealing (10 min. periods) of the components of the E3 defect in GaAs, and the total E3 (square symbol) is the sum of the three E3 components.

4.2.8 Summary of the E3 electron irradiation induced defect

In summary, we found that the E3 is not a single defect, but consists of 3 different components (E3a, E3b and E3c). Different measurements were done on these defects, and we found that one of these defects was highly concentration dependent (E3c) and another of them annealed out earlier

than the other two (E3b). The origin of each of them was investigated and compared to the reports by other scientists. Bondarenko *et al.* [110] deduced from positron annihilation and Hall measurements that in Si-doped GaAs, the E3 may be a $V_{Ga} - Si_{Ga}$. This proposed defect could well be our E3c since we found that the E3c concentration is directly proportional to the Si doping concentration. E3a is the most prominent component of the E3 and may, therefore, be the V_{As} which Bondarenko *et al*. [110] predicted to form in undoped GaAs. The latest reports regarding the E3 origin by Schultz [100] supports that E3 is V_{As}. Stievenard *et al*. [102] argued that the E3 is a $V_{As} - As_i$. Since nd the As_i was found to anneal out earlier (around 493 K) than V_{As} (around 523 K), we conclude that the E3b that anneals out earlier is the As_i. The annealing temperature of the E3a agreeing roughly with that of the V_{As} is further support for the E3a being due to the V_{As}.

4.3 Characterisation of the sputter deposition induced defects

Control samples were prepared by resistive evaporation of contacts on material with two different carrier densities (1.0×10^{15} cm^{-3} and 1.0×10^{16} cm^{-3}). Au Schottky barrier contacts that were DC sputter deposited on Si-doped *n*-type GaAs under a power of 150 W will be discussed in this section. DLTS and Laplace DLTS were used to characterise the sputter-induced defects near the surface of the GaAs. (Note that, for clarity, we identify the samples by their approximate carrier densities before sputtering in order to avoid repetition of the different numbers of carrier densities of sputtered and control samples).

4.3.1 The *I-V* and *C-V* characterisation

Figure 4.12 shows the *I-V* and *C-V* graphs. As shown in this figure, the ideality factor determined from the *I-V* curve for control samples was 1.02 for both carrier densities which is close to the ideal factor 1.0. This ideality factor indicates that thermionic emission was the dominant current transport mechanism. However, for sputtered samples, the ideality factor was higher and we had a lower barrier height compared to the control sample. Contrary to some deviation from ideality, the ideality factor was still close to unity, while the reverse leakage current did not increase significantly above the saturation current, which indicates that the thermionic emission was still the main current transport mechanism in the sputtered diode as well. The lower doped material displayed a higher reverse leakage current, apparently on account of more carrier generation by defects in the wider depletion region. The sputtered samples furthermore have higher series resistance compared to the control samples. The details are included in Table 4.3.

Figure 4.12 (b) displays the *C-V* characteristics (plotted $1/C^2$ vs V) of the samples. According to the figure, the carrier concentration profiles for control samples were constant but the sputtered samples show a significant increase in carrier concentration. The sputtered samples' decrease in barrier height compared to control samples reflects the decrease in barrier height observed in the *I-V* characteristics. The barrier heights calculated from *C-V* characteristics were found to be higher than the *I-V* barrier heights, which demonstrates that there might have been some barrier height in homogeneities. The slight deviations from linearity in the *C-V* characteristics illustrate the minor

variation in the carrier density with depth. It is evident that the carrier density changes due to sputter deposition occur up to a depth far beyond that probed by the depletion region. Hence, it is clear that the sputtered defects have diffused a significant distance into the semiconductor.

The deviation from ideal thermionic emission and the reduction in the barrier height may be due to near-surface damage changing the properties of the interface, as well as deep level defects causing both carrier generation and barrier height inhomogeneity.

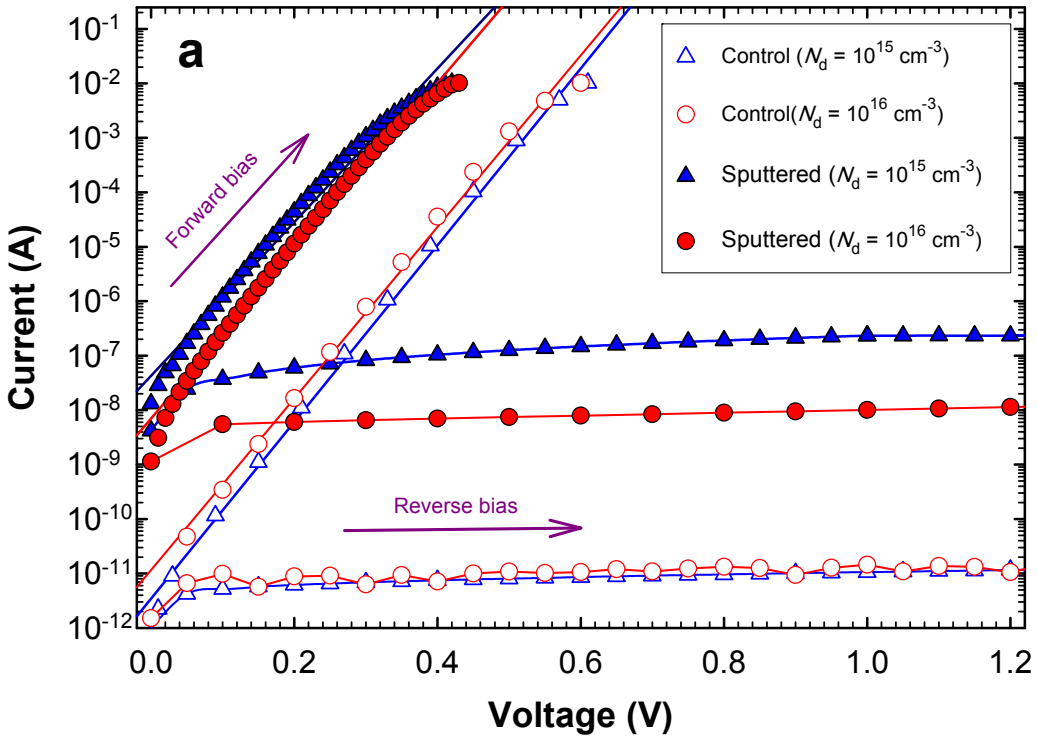

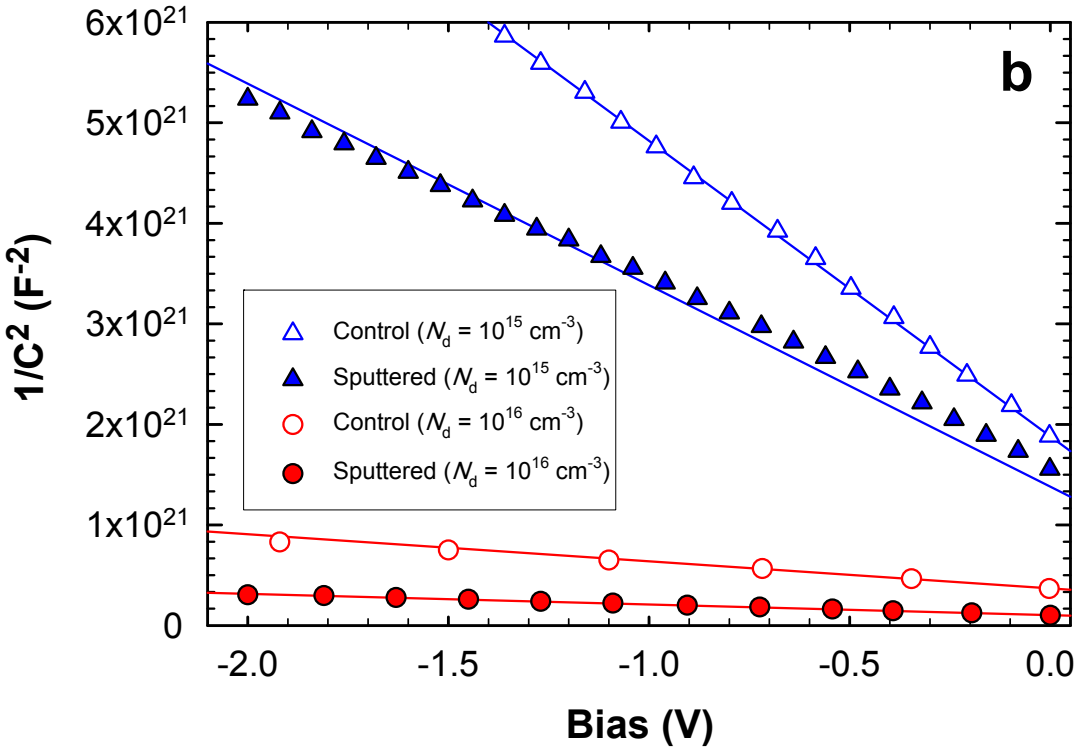

Figure 4.12: Demonstrates the change in (a) *I-V* and (b) C^{-2}-*V* plots as a result of the sputter deposition of 1.0×10^{15} cm^{-3} and 1.0×10^{16} cm^{-3} samples.

The current density vs bias and net donor concentration profiles are shown in Figure 4.13. With regard to Figure 4.13 (a), the current density increases with increasing bias. The sputtered samples have higher carrier density at lower bias compared to control samples. The depth profile graph is shown in Figure 4.13 (b). According to this graph, the control samples have deeper defects compared to sputtered samples, and it is shown that sputtered samples represent near-surface damage. This graph proves that sputter deposition increases the carrier concentrations of all samples.

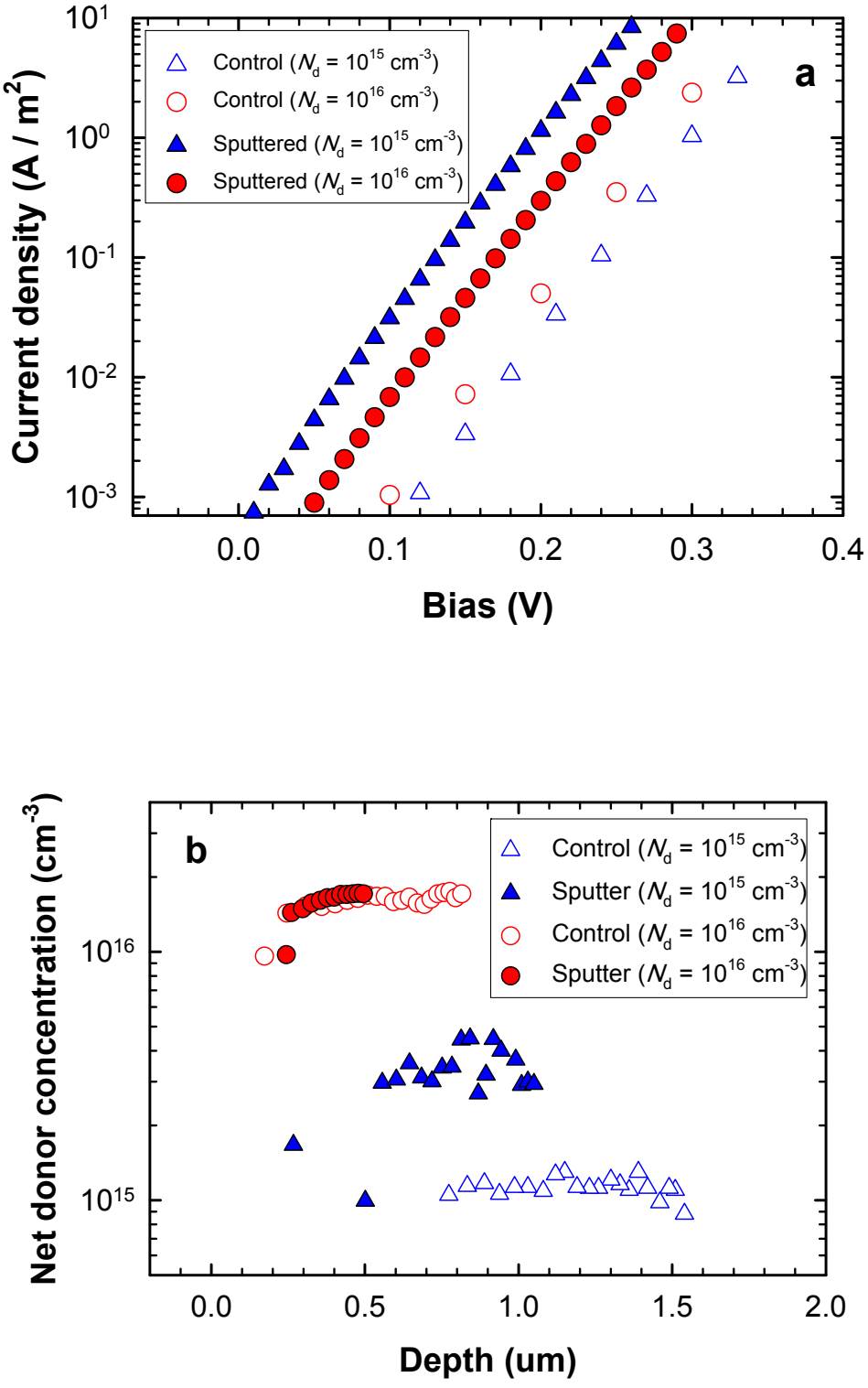

Figure 4.13: (a) carrier density difference of control and sputtered samples, (b) net donor concentration of control and sputtered samples. (1.0×10^{15} cm^{-3} and 1.0×10^{16} cm^{-3}).

Table 4.3: Diode parameters of *n*-type GaAs of control and sputter samples (1.0×10^{15} cm^{-3} and 1.0×10^{16} cm^{-3})

Sample		n	ϕ_{bIV} (eV)	ϕ_{bCV} (eV)	R_s (Ω)	Carrier concentration (cm^{-3})
1.0×10^{15} cm^{-3}	control	1.02	0.96	0.97	3.8	1.0×10^{15}
	sputtered	1.15	0.63	0.74	10	3.5×10^{15}
1.0×10^{16} cm^{-3}	control	1.02	0.87	1.72	3.4	1.6×10^{16}
	sputtered	1.11	0.65	1.05	4.8	1.6×10^{16}

4.3.2 The DLTS results

The DLTS spectra of sputter induced defects and control sample of n-GaAs Si doped with a concentration of 1.0×10^{15} cm^{-3} and 1.0×10^{16} cm^{-3} is shown in Figure 4.14. These spectra were recorded in the 20-405 K temperature range and at a rate window of 80 s^{-1} by applying a reverse bias and filling pulse amplitude of –1 V and 1.4 V, respectively. Curve (a) displays the control sample spectra, and we can see only the EL2 defect. For the sputtered diodes on 1.0×10^{16} cm^{-3} doped GaAs, we observed seven defects (S1, S2, S3, S4, S5 and S6a & S6b), as shown in curve (b). The sputtered diodes on 1.0×10^{15} cm^{-3} doped GaAs are shown in curves (c) and (d) which indicates that the S5 and S3 are metastable: After applying –2 V at 400 K for 10 minutes and cooling down under –2 V, the S5 defect transformed to S3. However, when by applying zero bias at 400 K for 10 minutes and cooling down under the same bias, the S3 defect transformed back to the S5 defect. For the S1 defect, the procedure was the same; by applying reverse bias of –2 V at 400 K for 10 minutes the S1 defect was introduced and by applying zero bias at 400 K for 10 minutes, this defect was totally removed. On the other hand, no new defect was observed when the S1 defect was removed.

According to Figure 4.14, it is clear that the s4 defect was highly carrier density dependent and the peak height decreased by about a factor ten when the dopant concentration was reduced by a factor of 10. Note that, in order to show the S4 defect more clearly in 1.0×10^{15} cm^{-3} doped material, the S4 peak height was multiplied by a factor of 10 in curves (c) and (d),. The S2 defect was only observed in one of the 1.0×10^{16} cm^{-3} doped samples, but the reason for this is not clear as yet.

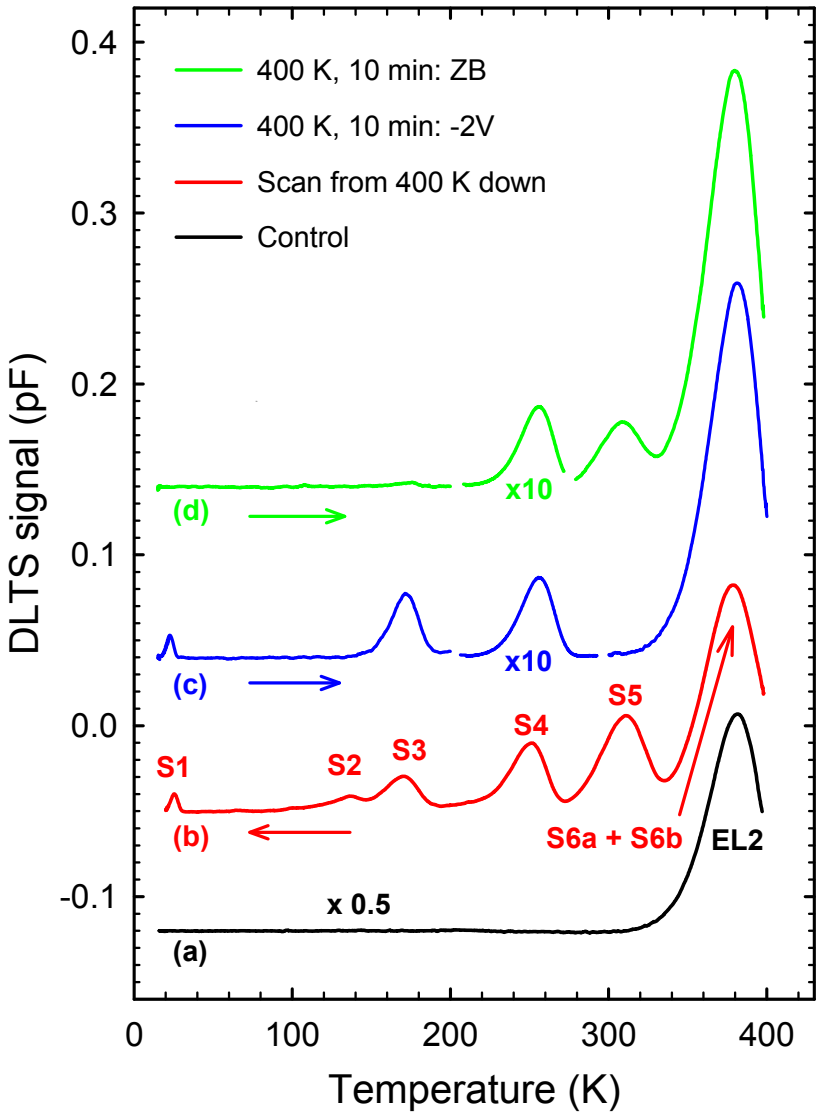

Figure 4.14: DLTS spectra of (a) a control sample, (b) sample (1.0×10^{16} cm^{-3} Si-doped) directly after sputtering, (c) sputtered sample (1.0×10^{15} cm^{-3} Si-doped) after applying –2 V at 400 K for 10 minutes, and (d) sputtered sample (1.0×10^{15} cm^{-3} Si-doped) after applying zero bias for 10 minutes at 400 K. The reverse bias, V_r, and filling pulse amplitude, V_p, were –1.0 and 1.4 V, respectively with a 1 ms pulse width, and the rate window was 80 s^{-1} for all samples.

4.3.3 The Arrhenius plot

Figure 4.15 displays Arrhenius plots of seven sputter-induced defects (at 26 K, 140 K, 180 K, 265 K, 320 K and 348 K) in *n*-type GaAs with a carrier concentration of 1.0×10^{15} cm^{-3}. The activation energies of these defects are listed in Table 4.4. As seen in this figure, the activation energies and

apparent capture cross-sections of the sputtered defects are different from high-energy irradiation-induced defects which measured before. Laplace DLTS, shown later, displayed that the S6 defect had two components which we labelled S6a and S6b. Some of the sputter-deposition induced defects were similar to sputter-etching induced defects reported by Venter *et al.* [111], nitride encapsulation [112] and hydrogen plasma treatment [113], [114] (Comparison included in Table 4.4).

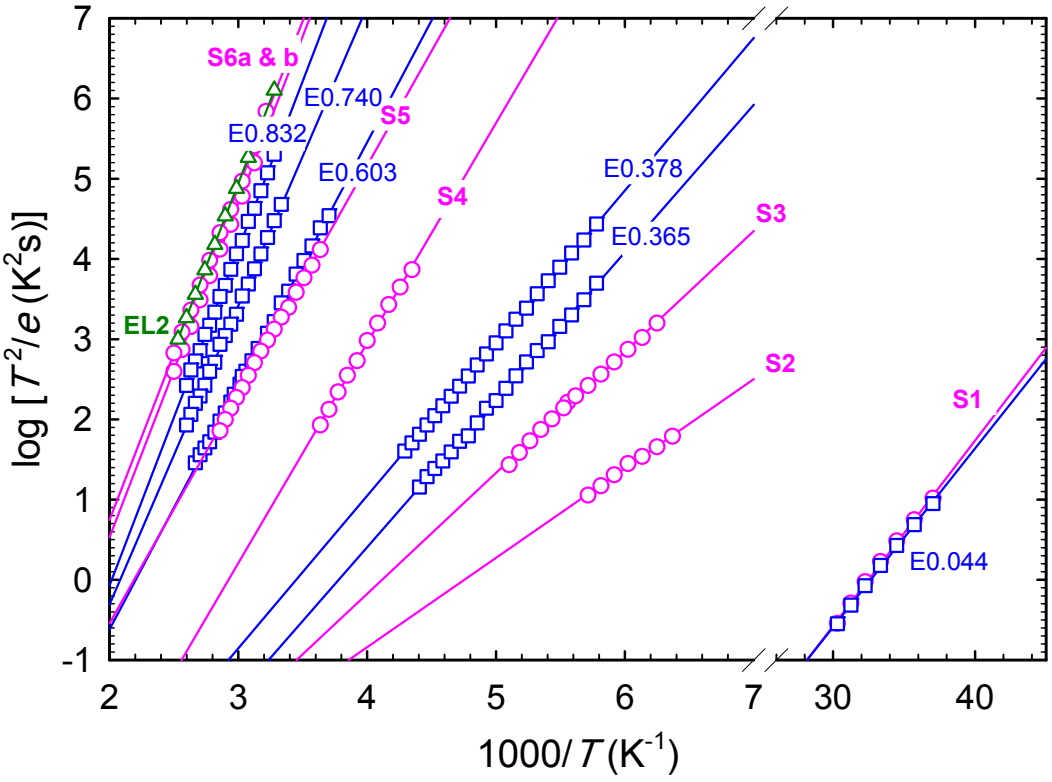

Figure 4.15: Arrhenius plots of sputter-deposition induced defects (circle symbols), n-GaAs electron irradiation induced defects (square symbols, labelled as in Table 4.4) and the EL2 (triangle symbols*)*.

Table 4.4: Electronic properties of sputter induced defects (S1 – S6), Stress-related or nitride capping induced defects [112], hydrogen plasma induced defect [113], [114], Ar plasma-etching induced defects [111], electron-irradiation induced defects and the EL2. (S, P, NC, H and E respectively represent: sputter, Ar plasma, nitride capping, hydrogen plasma and electron irradiation-induced defects)

Defect label	Origin*	E_A (eV)	σ_a (cm^2)	Stability
S1	S	0.046	3.1×10^{-13}	Metastable
E1' [111]	P	0.040	5.3×10^{-14}	Metastable
S2	S	0.22	1.9×10^{-15}	Stable
S3	S	0.30	1.6×10^{-14}	Metastable (transformed to S5)
M4[112]	NC	0.31	1.8×10^{-18}	Metastable (transformed to M3)
M4[114]	H	0.30	----------	Metastable (transformed to M3)
M4[113]	H	0.30	----------	Metastable (transformed to M3)
E(0.31) [111]	P	0.31	5.2×10^{-14}	Metastable (transformed to E0.61)
S4	S	0.55	1.0×10^{-12}	Stable
S5	S	0.56	1.3×10^{-14}	Metastable (transformed to S3)
M3[112]	NC	0.61	5.1×10^{-18}	Metastable (transformed to M4)
M3[114]	H	0.50	----------	Metastable (transformed to M4)
M3[113]	H	0.55	----------	Metastable (transformed to M4)
E(0.61) [111]	P	0.61	7.1×10^{-14}	Metastable (transformed to E0.31)
S6a	S	0.830	8.8×10^{-13}	Stable
S6b	S	0.840	6.6×10^{-13}	Stable
E(0.044)	E	0.044	1.9×10^{-14}	Stable
E(0.365)	E	0.365	8.7×10^{-14}	Stable
E(0.378)	E	0.378	3.6×10^{-14}	Stable
E(0.603)	E	0.603	4.9×10^{-14}	Stable
E(0.740)	E	0.740	5.7×10^{-14}	Stable
E(0.832)	E	0.832	2.8×10^{-12}	Stable
EL2	N	0.820	3.2×10^{-13}	Stable

4.3.4 Laplace results of the EL2 and the S6 defect

Figure 4.16 shows the Laplace DLTS results for the EL2 defect in the control sample (1.0×10^{15} cm^{-3}) and the S6 defect in the sputtered sample. As seen the S6 defect has two components (S6a and S6b) and these do not directly correspond to the EL2 defect. It is interesting that the EL2 defect in the control sample had a small component that was not previously observed. The sputtered sample did not have the EL2 defect, and we speculate that the EL2 was probably modified to S6a and S6b.

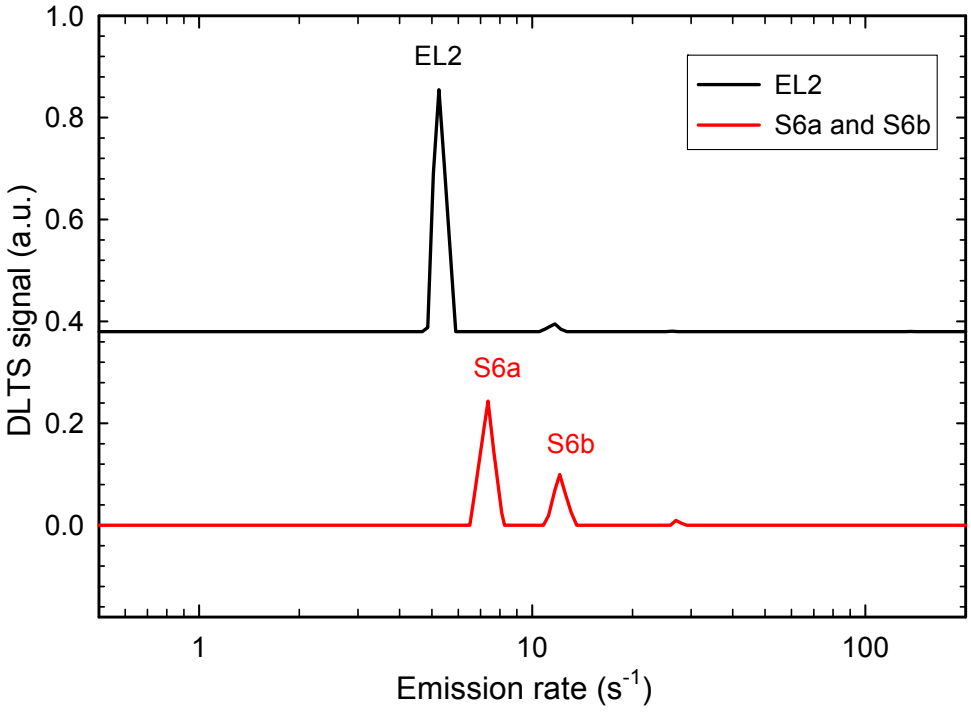

Figure 4.16: Laplace DLTS spectra of EL2 and S6 defects as observed in 1.0×10^{15} cm^{-3} doped material. Both spectra were recorded at 350 K with a reverse bias of –1 V and a filling pulse amplitude of 1.4 V.

4.3.5 Metastability

As shown in Figure 4.14, the S3 and S5 defects were metastable. We checked the metastability in 1.0×10^{15} cm^{-3} doped material .From Figure 4.17, it is clear that the S3 transformed into the S5 after annealing under zero bias at 400 K for 10 minutes, then cooling down under zero bias to 295 K, where the spectrum was measured under –1 V bias. The S5 transformed to the S3 defect, through the application of reverse bias (–2 V) at 400 K for 10 minutes, followed by cooling down under – 2 V to 180 K and measuring of the spectrum under a reverse bias of –1 V. It is interesting to observe the direct correlation between the concentration of S3 and S5. The introduction and removal curves of the metastable defects are shown in Figure 4.17. The transformation curves were measured by transforming as much as possible of the defect into one state at 400 K (–2 V bias for the S3, 0 V bias for the S5) then cooling down (under the same bias conditions) to the annealing temperature, where the sample was annealed under the transformation conditions (0 V bias or –2 V bias respectively) for 5 minutes, followed by rapid cooling to the measurement temperature (295 K or 180 K) under the transformation conditions.

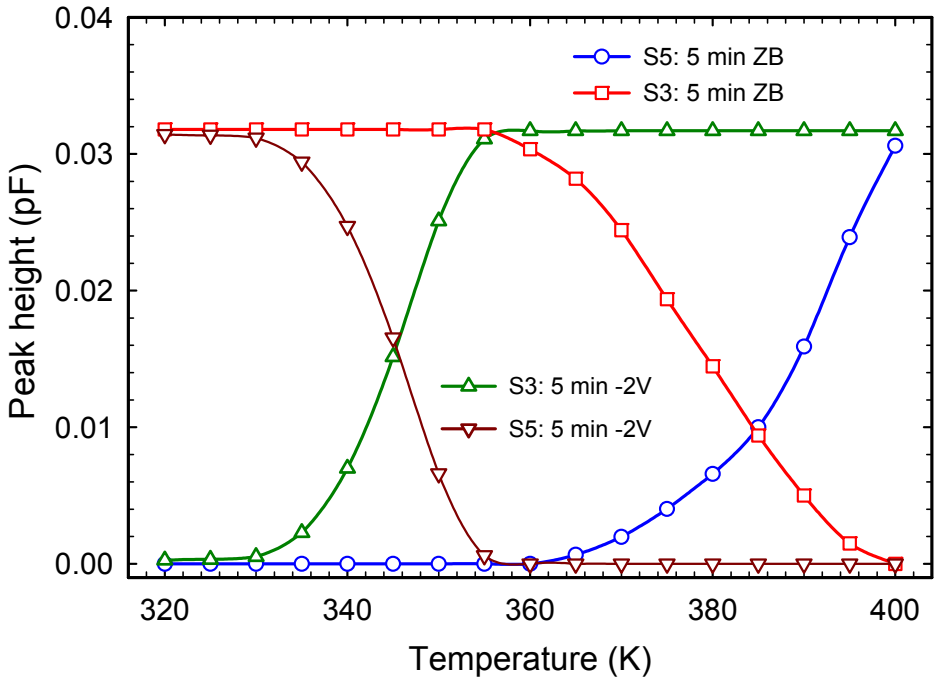

Figure 4.17: Introduction and removal of S3 and S5 metastable defects. The conditions for the transformations are indicated in the figure.

The isochronal transformation of S3 → S5 and S5 → S3 was modelled by first order kinetics [112]:

$$N_X(t,T) = N_0[1 - \exp(-te_0(T))] \tag{4.6}$$

and

$$N_y(t,T) = N_0 \exp[-te_0(T)] \tag{4.7}$$

where N_x corresponds to the defect being removed, and N_y to the defect being introduced. Here N_0 is the maximum defect concentration, t is the annealing time in seconds, and $e_0(T)$ is the temperature dependent transformation rate can be written as:

$$e_0(T) = \alpha \exp(-E/kT) \tag{4.8}$$

In this equation α is a pre-factor with units of s^{-1}, E is the activation energy for the particular transformation of the defect and k is the Boltzmann constant.

The Arrhenius data of the introduction and removal rate of the S3 and S5 metastable defects of 1.0 × 10^{15} cm^{-3} doped material are shown in Figure 4.18, and the transformation rate of each one was calculated.

In this transformation, we have 3 × 10^{15} s^{-1} and 4 × 10^{21} s^{-1} respectively, as pre-factors for eqn. (4.8). The pre-factor obtained from our measurements for the transformation of S3 to S5 is nearly the same as one of the results reported by Buchwald *et al*. [112] (10^{21} s^{-1} pre-factor for the introduction of M4 and the decay of M3). For the transformation of S5 to S3 the pre-factor was 10^{15} s^{-1}, which is higher than the 10^{7} s^{-1} reported by Buchwald *et al.* [112], 10^{8} s^{-1} reported by Conibear *et al* [113] and 10^{11} s^{-1} reported by Pfeiffer and Weber [114].

The activation energies obtained from our measurements are 1.69 and 1.46 eV. By comparing the results with previous reports we conclude that the transformation may be related to arsenic vacancy (V_{As}) diffusion [115]. We compared our results to other reports on Ga, Si or Au diffusion, but these results do not match our data [116], [117], [118].

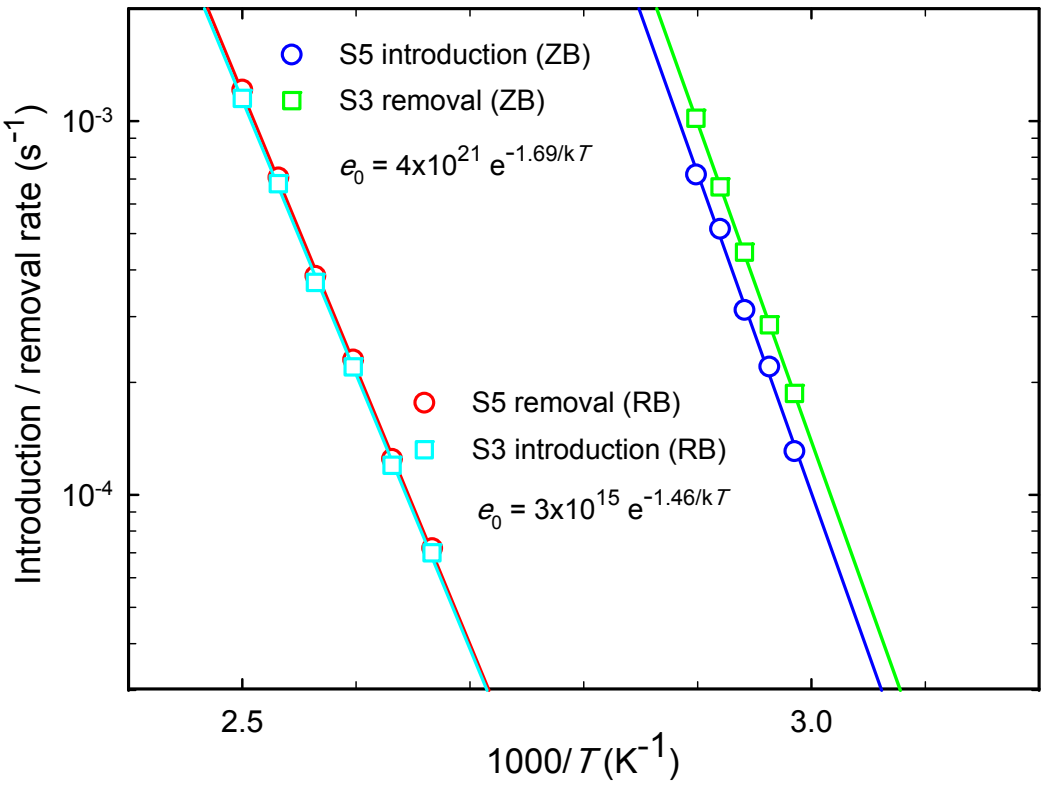

Figure 4.18: Arrhenius data for the transformation of S3 → S5 and S5 → S3.

The pre-factor α can be physically related to the attempt frequency of the process and can be used to deduce the physical mechanism leading to the temperature dependence. Some mechanisms identified so far [119]:

- Free-carrier capture by multi phonon emission ($\alpha \sim 10^7$ s^{-1}),
- Elementary atomic jump ($\alpha \sim 10^{12}$ s^{-1}),
- Free-carrier emission ($\alpha \sim 10^{13}$ - 10^{14} s^{-1}).

The high pre-factor for the transformation of S3 to S5 ($\alpha \sim 10^{21}$ s^{-1}) is larger than would be expected for direct free-carrier capture by a potential well with a large capture cross-section. The smaller capture pre-factor for the transformation S5 to S3 seems to indicate free carrier emission.

4.3.6 Depth Profile

Figure 4.19 displays the depth profile of three different dopant carrier densities (1.0×10^{15} cm^{-3}, 1.0×10^{16} cm^{-3} and 8.0×10^{16} cm^{-3}). The defect concentrations in sputter deposited samples exhibited a rapid decay with an increase in the depth, indicating that the defects were highly concentrated at the surface. In the more highly doped material, the defect concentration was generally higher, but also shallower beneath the Schottky junction. This can be explained by enhanced diffusion in the depletion region (which is wider in lower doped material), possibly due to the charge state of the defects or due to the electric field in the depletion region. Alternatively, they can move away from the surface region by recombination enhanced diffusion 'activated' by the electron-hole pairs created by the energetic electrons or the glow discharge.

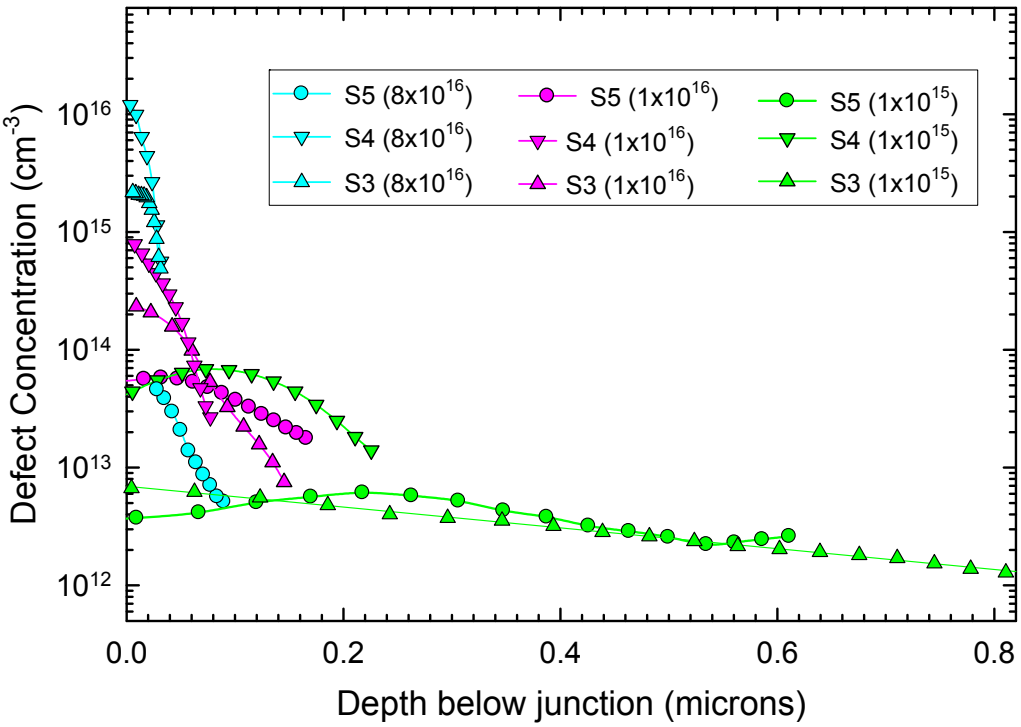

Figure 4.19: Depth profile of the observed deep levels in samples with different carrier densities (1.0×10^{15} cm^{-3}, 1.0×10^{16} cm^{-3} and 8.0×10^{16} cm^{-3}).

4.3.7 Electric field dependence

The electric field dependence of the emission from the sputter-induced defects was measured for the sample with 1.0×10^{15} cm^{-3} carrier density in different temperature ranges to distinguish between Poole-Frenkel (emission rate proportional to the square root of the electric field) and phonon-assisted tunnelling (emission rate proportional to the square of the electric field). Figure 4.20 shows that the electric field dependence of S3 and S4 defects in Figure 4.21 displays the same electric field dependence of the S5 defect. According to Figure 4.20, the field enhanced emission of carriers is described via Poole-Frenkel and phonon-assisted tunnelling mechanisms. For the S3 and S4 defects, the emission of carriers was described by phonon-assisted tunnelling at low fields and then gradually changed to Poole-Frenkel at high fields, but for the S4 defect, the Poole-Frenkel at higher field is not very clear. But as shown in Figure 4.21 the emission of carriers for the S5 defect occurred through the phonon-assisted tunnelling method.

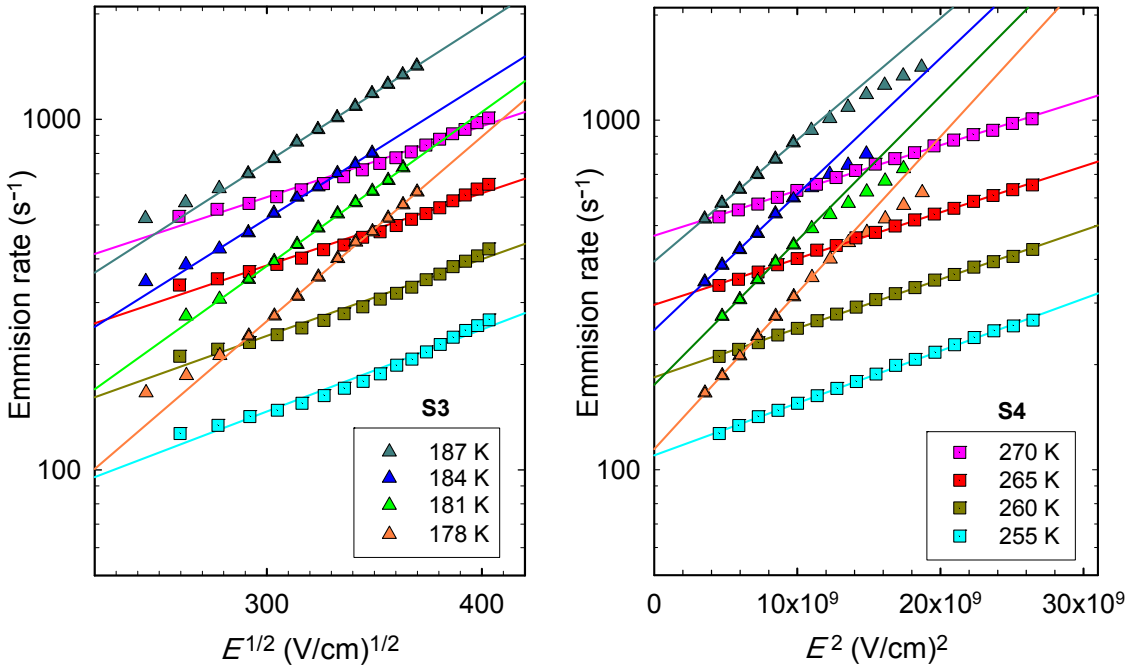

Figure 4.20: The electric field dependence graph for S3 and S4 defect on 1.0×10^{15} cm^{-3} sample. Note that triangle and square symbols, relate to S3 and S4 defects occur in both graphs.

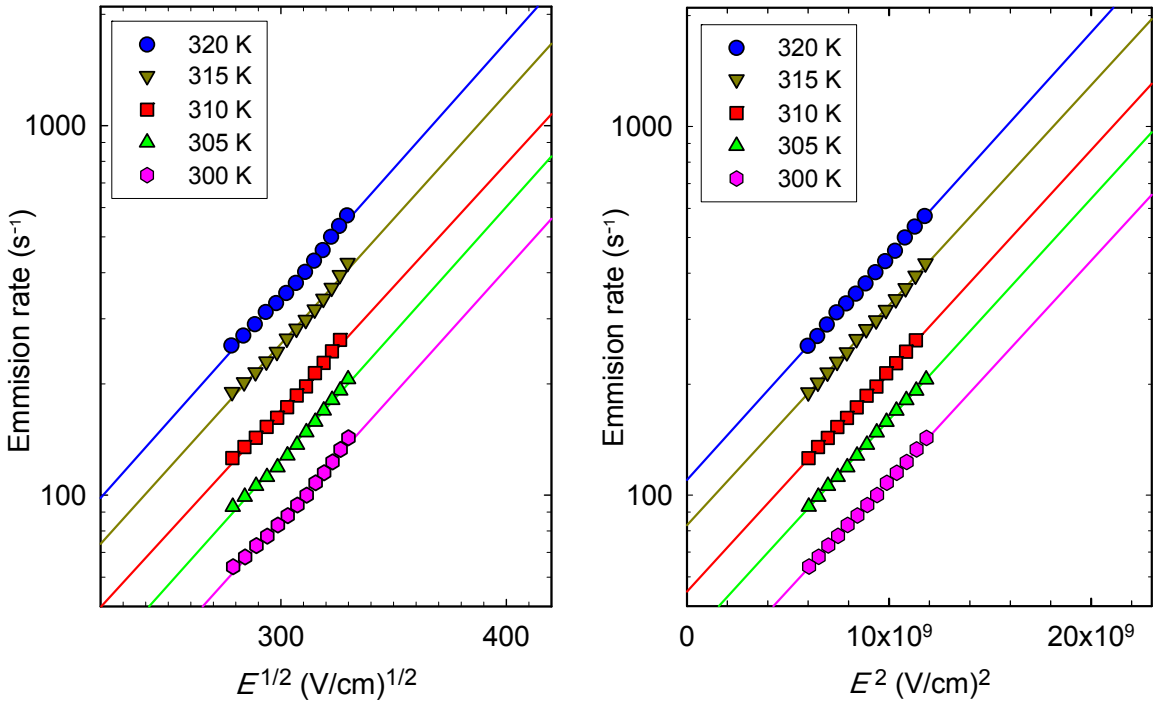

Figure 4.21: The electric field dependence of S5 defect on 1.0×10^{15} cm^{-3} sample.

4.3.8 Capture cross-section

The real capture cross-section measurements were performed for the S3, S4 and S5 defects of 1.0×10^{15} cm^{-3} samples in a different temperature range for each of them. Each of the results was measured under (V_r= –2, V_{P1}= 0.06 and V_{P2}= – 1) V, with different pulse widths in a specific temperature. As shown in Figure 4.22, by increasing temperature, the slope is getting steeper as well. The S3 defect is higher than the S4 and S5 defects. The exceptionally small capture cross-section of the S5 might be due to a capture barrier. This is supported by reasonably strong temperature dependence. According to Equation 4.4, the capture cross-section for each of them was calculated and listed in Table 4.5. As seen in this table the capture cross-section for the S5 defect is higher than for the other two.

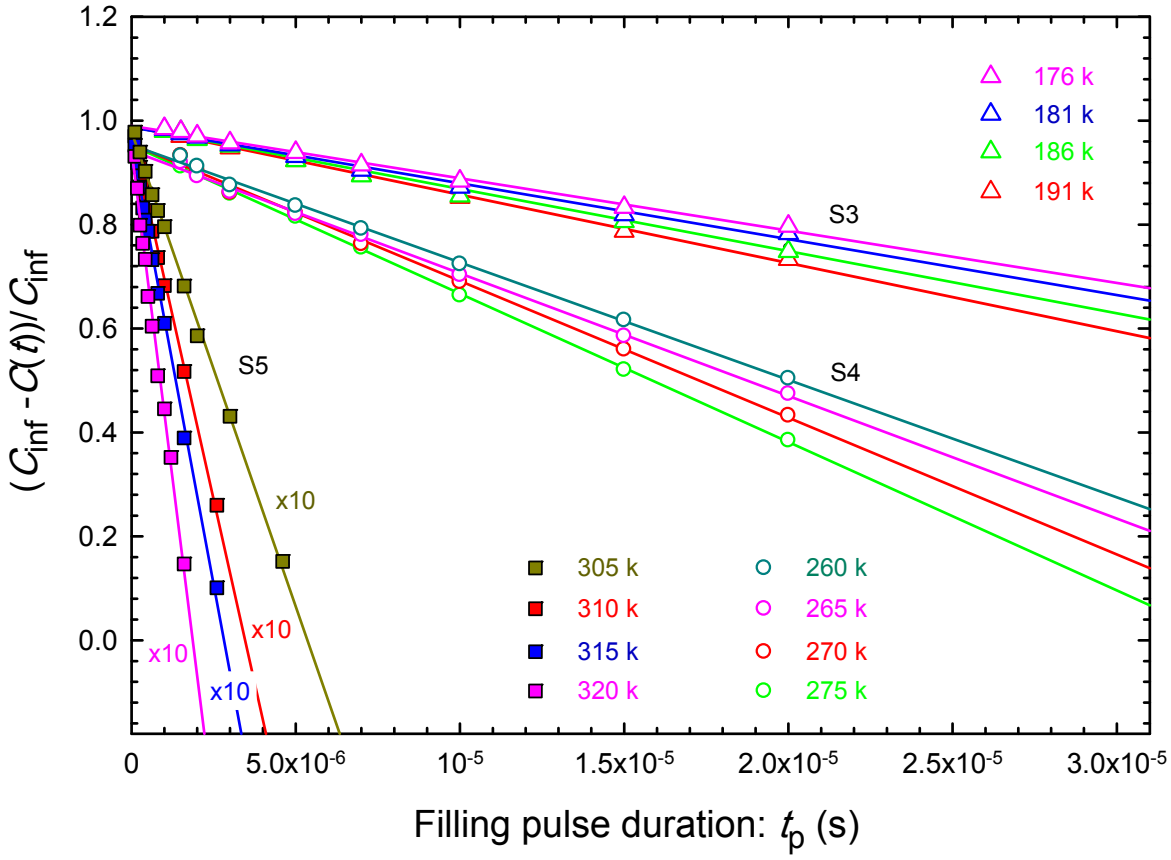

Figure 4.22: Determination of the capture cross-section of S3, S4 and S5 defects in GaAs for $N_D = 1.0\times10^{15}$ cm^{-3}.

Table 4.5: The capture cross-section results of the S3, S4 and S5 defects at different temperatures.

Defect	Temperature (K)	σ_n (cm^2)
S3	176	1.33×10^{-18}
	181	1.43×10^{-18}
	186	1.48×10^{-18}
	191	1.52×10^{-18}
S4	260	2.43×10^{-18}
	265	2.56×10^{-18}
	270	2.70×10^{-18}
	275	2.76×10^{-18}
S5	305	1.82×10^{-17}
	310	2.79×10^{-17}
	315	3.33×10^{-17}
	320	4.91×10^{-17}

The capture cross-section for S3, S4 and S5 defects were measured at different temperatures and are used in Figure 4.23 to calculate the capture barriers (applying Equation (4.5)). As seen in Figure 4.23, the capture barriers for S3, S4 and S5 are 0.025 eV, 0.053 eV and 0.33 eV, respectively. The high temperature limit of capture cross-section (σ_∞) for S3, S4 and S5 were calculated to be (7.24×10^{-18} cm^2, 2.69×10^{-17} cm^2 and 5.75×10^{-12} cm^2 respectively).

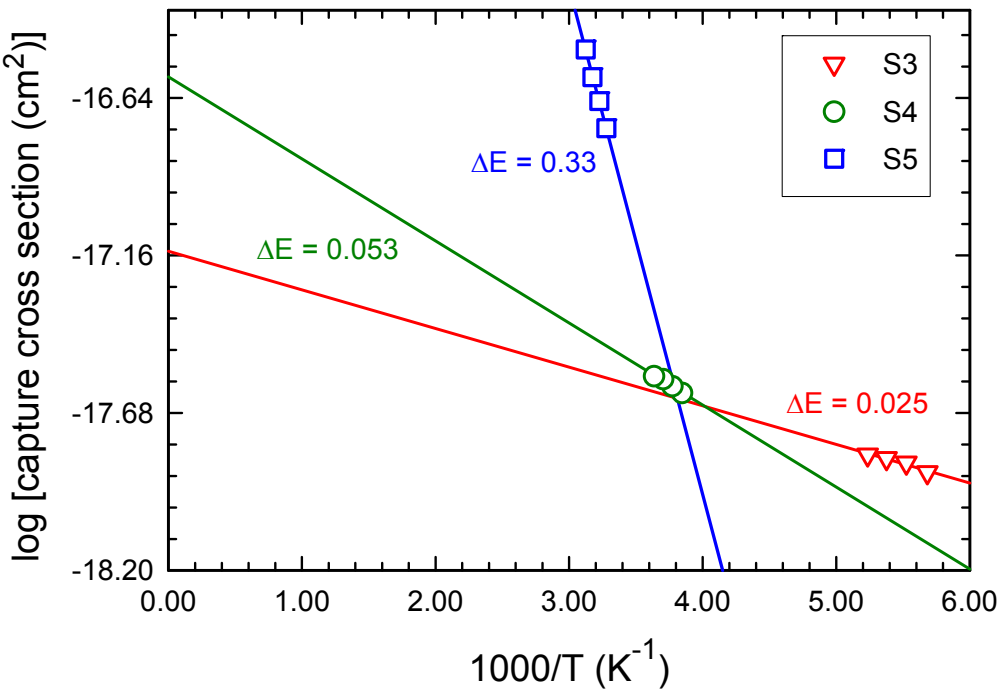

Figure 4.23: Arrhenius plots for the determination of the capture barriers of the S3, S4 and S5 defects in $N_D = 1.9\times10^{15}$ cm^{-3}.

The real capture cross-section of S3 and S4 defect are of the order of 10^{-18} cm^2, which is in the range that may be explained by the Auger mechanism, according to Henry *et al*. [120]. For the S5 defect the capture cross-section is of the order of 10^{-17} cm^2 and is strongly temperature dependent. These features of this capture cross section indicate that this capture occurs through multiphonon emission (MPE) [109].

4.3.9 Effect of annealing on the *I-V* and *C-V* characteristics

In this experiment, we annealed 1.0×10^{15} cm^{-3} and 1.0×10^{16} cm^{-3} doped, sputtered material, under vacuum isochronally for 10 minutes starting at a temperature of 425 K in 25 K steps. The results are shown in Figure 4.24 and Figure 4.25 respectively. As shown in Figure 4.24 (a), the ideality factor for 1.0×10^{16} cm^{-3} doped sample is almost constant but from 575 K it starts to increase significantly. For the 1.0×10^{15} cm^{-3} doped sample, the ideality factor was improved slightly by annealing, and only increased significantly at the much higher temperature of 725 K. This may be

due to the highly doped material having a high concentration of defects close to the interface (as measured by DLTS depth profiling earlier), leading to faster degradation of the Schottky diode.

The series resistance vs annealing temperature is shown in Figure 4.23 (b). For 1.0×10^{15} cm^{-3} doped sample, the series resistance initially decreased sharply and then increased slowly with further annealing, but for the high carrier concentration, the changes is not as significant and it decreased by increasing temperature. The difference is probably due to the resistivity of the lower carrier density material being more sensitive to the presence of defects.

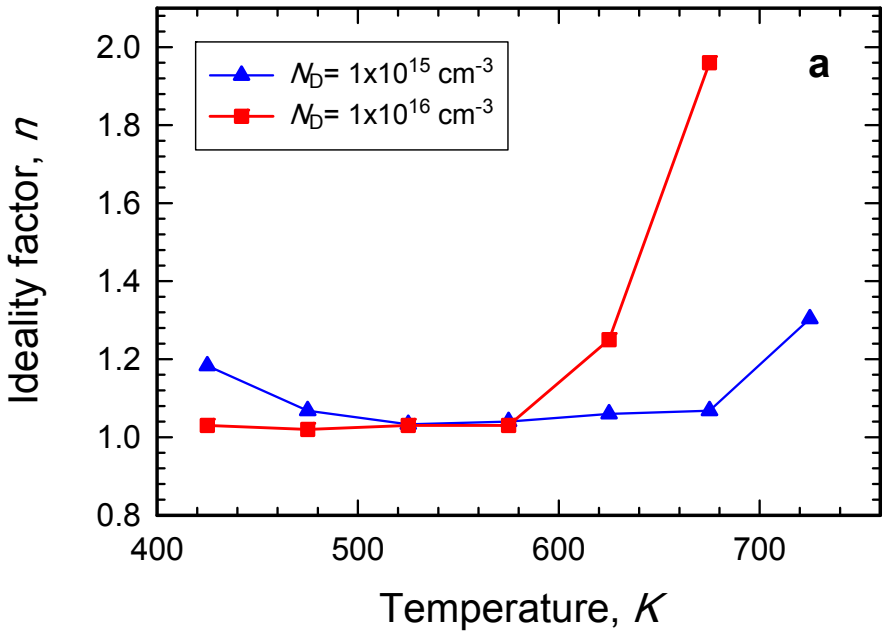

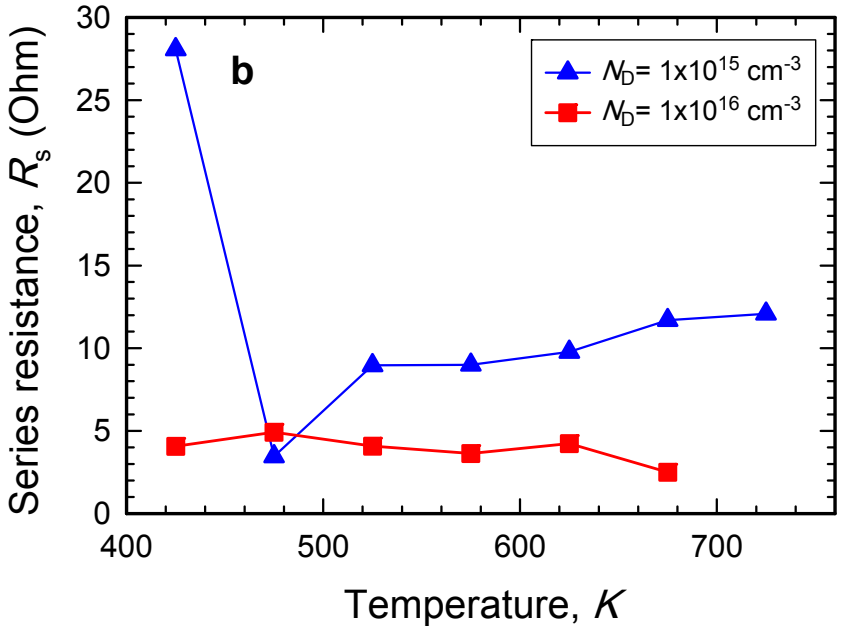

Figure 4.24: The (a) ideality factor and (b) series resistance during annealing for 1.0×10^{15} cm^{-3} and 1.0×10^{16} cm^{-3} doped samples.

According to Figure 4.25 (a), the barrier height as determined by I-V measurements was increased by annealing for both samples and then decreasing slowly. Again, the higher carrier density material seemed to degrade faster, probably due to the higher concentration of defects near the junction. However, for C-V measurements, the Schottky barrier height for 1.0×10^{15} cm^{-3} initially decreased sharply and then increased with annealing temperature. Here the material with the lower carrier density was more sensitive to changes in defect concentration. The initial rapid change is probably due to some defects close to the junction annealing out. Due to their proximity to the interface, these defects were not be visible by DLTS.

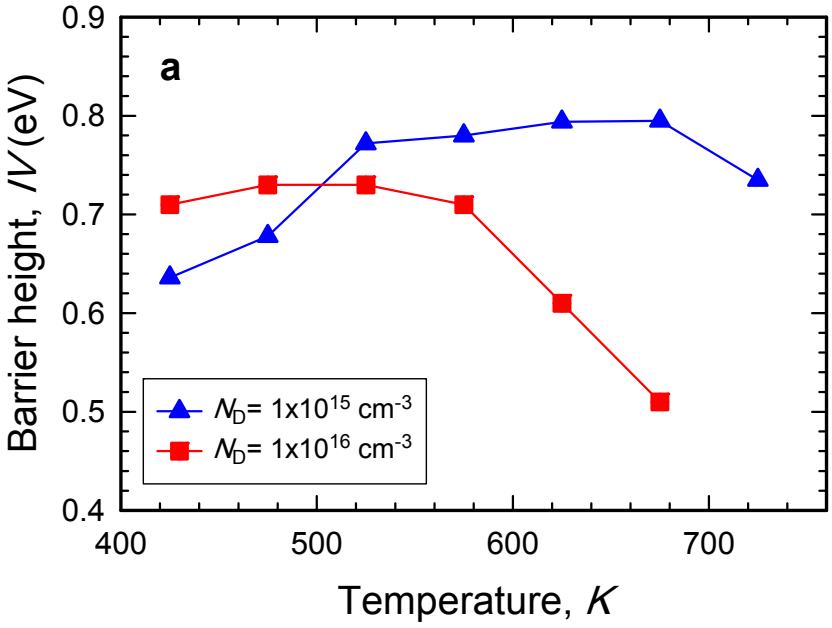

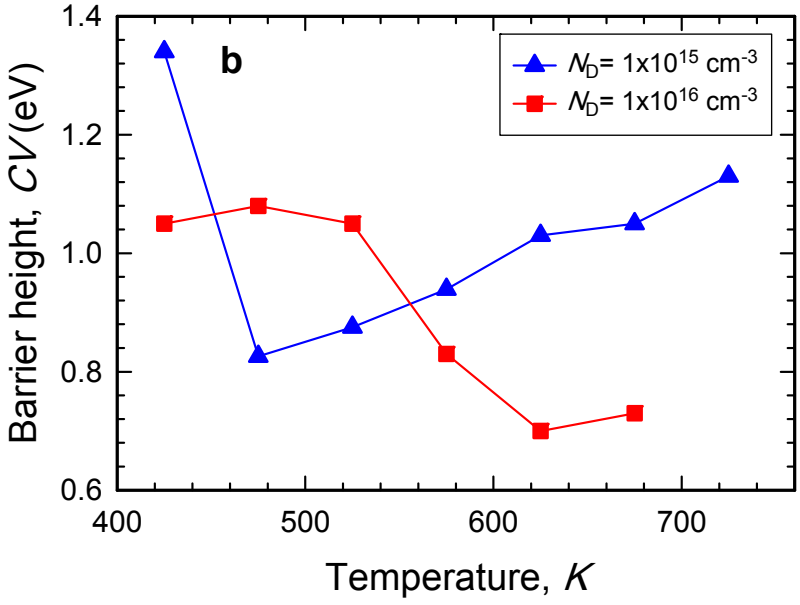

Figure 4.25: Schottky barrier height measured by (a) *I-V* and (b) *C-V* during annealing for 1.0×10^{15} cm^{-3} and 1.0×10^{16} cm^{-3} doped samples.

4.3.10 Summary of sputter deposition induced defects

In summary, the sputter deposition procedure had a significant effect on the ideality factor and Schottky barrier heights of the samples. DLTS spectra indicate that sputter deposition introduced 7 defects (S1, S2, S3, S4, S5 and S6a & S6b). Among these defects 3 of them (S1, S3 and S5) were metastable, and one of them was highly dopant dependent (S4). The S6 components are modified remnants from the EL2 defect. The pre-factors of the introduction and removal of two metastable defects (S3 and S5) were calculated, which corresponded to the transformation of S3 to S5 is 4×10^{21} s^{-1} and S5 to S3 is 3×10^{15} s^{-1}. The activation energies obtained from the transformation measurements may be related to V_{As} diffusion. Depth profiling indicated that the 1.0×10^{15} cm^{-3} doped material had deeper defects with a lower concentration under a Schottky junction compared to the higher carrier density material which can be explained by enhanced diffusion in the depletion region. Capture cross-section of the S5 defects is larger than the S3 and S4 defects that might be due to a capture barrier. The capture barrier and high temperature limit of the capture cross-section were determined for these defects and also followed the same trend as real capture cross-section, the results for S5 defect are larger than the others. For the S3 and S4 defects, the capture cross-section agrees with values predicted by the Auger mechanism and for S5 defect the values agree with the multiphonon emission (MPE) mechanism. From the annealing measurements, it is clear that by increasing annealing temperature the ideality factor initially improved for 1.0×10^{15} cm^{-3}, but for sample 1.0×10^{16} cm^{-3} it was almost constant up to 575 K. We believe that in higher concentration material, there are a high concentration of defects close to the interface which cause the faster degradation of the Schottky diode. The series resistance for lower carrier density initially decreased sharply and then increased during isochronal annealing, however, the higher doping density material showed much smaller change. The difference may be due to the lower carrier density material being more sensitive to the presence of defects. Finally the barrier heights calculated for *I-V* and *C-V* measurements. For *I-V* measurements the barrier height of both samples increased during annealing and then decreasing gradually, but the higher concentration material degraded faster and as explained before, it may due to the higher concentration of defects near the junction. For *C-V* measurements the barrier height for lower carrier concentration initially decreased sharply by annealing which is due to the sensitivity of this material to change in defect concentration.

5 CONCLUSION

In this dissertation, the E3 radiation-induced defects and sputtering induced defects in GaAs were studied and characterized in detail. It was shown that the E3 defect consists of 3 components (E3a, E3b and E3c), and the electrical properties as well as the origin of these defects were investigated. Furthermore, it was shown that the sputtered samples contained seven defects that could be observed by means of DLTS (S1, S3, S4, S5, S6a and S6b). Using DLTS and Laplace DLTS measurements, the electrical properties of these defects were investigated. The aim of this chapter is to present a summary of the results and give an overview of possible future work.

5.1 Summary

5.1.1 E3 defect and its components

Three different Si-doped *n*-type GaAs samples (7.1×10^{14} cm^{-3}, 1.9×10^{15} cm^{-3} and 1.0×10^{16} cm^{-3}) were irradiated by beta particles for different time intervals. Using the results of *I-V* and *C-V* measurements, it was shown that the ideality factor of the Schottky barrier diodes on the samples, increased after electron irradiation due to the creation of generation-recombination centres as a result of the introduction of certain irradiation-induced defects. Furthermore, the results of these measurements indicated that the carrier density of these samples also increased after irradiation.

Afterwards, conventional DLTS measurements of the samples revealed three prominent defects in the temperature range 20 – 300 K (E1, E2 and E3). Subsequently, Laplace DLTS was used to study the finer structure of the E3 defect, and from the results, it was found that the E3 defect consisted of 3 components (E3a, E3b and E3c). From Laplace DLTS spectra, it was shown that the concentration of the E3c was highly carrier density dependent. From the Arrhenius plots drawn for each component, the activation energies and apparent capture cross-sections of each defect were determined (Table 5.1). Furthermore, through introduction rate measurements, it was found that the E3a was not carrier concentration dependent. Afterwards, by studying the effect of injection on other components, it was found that E3c was a metastable defect and it is removed by

subjecting the diode to minority carrier injection pulses at low temperatures (90 – 120K). For the re-introduction of the E3c, the sample was heated to above 160 K under zero bias. The electric field dependence of E3a for all three samples was measured and it was determined that the field enhanced emission of carriers can be described via phonon-assisted tunnelling and subsequently, tunnelling time was calculated.

The capture cross-sections for defects in the 1.0×10^{16} cm^{-3} Si-doped sample was shown to be about a factor of three lower than those in the 1.9×10^{15} cm^{-3} (3.1×10^{-17} cm^2 *vs.* 1×10^{-16} cm^2) sample. The capture barrier and high temperature limit of capture cross-section (σ_∞) were calculated for both carrier densities. The results are (0.023 eV, 1.94×10^{-15} cm^2) for lower carrier density and (0.039 eV, 5.24×10^{-15} cm^2) for higher carrier density material. The reason for these unexpected behaviour is not clear yet.

Finally, from results of the annealing experiments, the order of removal of these components were determined to be: E3b being the first at 500 K and E3a and E3c getting removed simultaneously afterwards at 525 K. Based on all these results combined with reports from different authors, the following table was made to describe the origin of each component of the E3 defect.

Table 5.1. Properties of the electron radiation induced defects in GaAs that we studied.

Defect	E_α (eV)	$\sigma_{n,a}$ (cm^2)	σ_n (cm^2)	Defect ID
E3	0.376† 0.360*	$4.1\times10^{-14\dagger}$ $3.2\times10^{-14\,*}$	--------	-------
E3a	0.380” 0.375† 0.360*	$4.7\times10^{-14”}$ $2.9\times10^{-14\,\dagger}$ $2.1\times10^{-14\,*}$	$3.0\times10^{-16\,”}$ (205K) $1.0\times10^{-16\,\dagger}$ (205K) $3.1\times10^{-17\,*}$ (205 K)	V_{As}
E3b	0.383” 0.395† 0.390*	$2.1\times10^{-13”}$ $3.4\times10^{-13\,\dagger}$ $4.8\times10^{-13*}$	----------	As_i
E3c	0.338” 0.351† 0.340*	$7.7\times10^{-14”}$ $1.3\times10^{-13\,\dagger}$ $6.8\times10^{-14*}$	----------	V_{Ga}-Si_{Ga}

”This study, measured in material with a free carrier density of 7.1×10^{14} cm^{-3}
†This study, measured in material with a free carrier density of 1.9×10^{15} cm^{-3}
*This study, measured in material with a free carrier density of 1.0×10^{16} cm^{-3}

Note: Here E_α is the activation energy, $\sigma_{n,a}$ is the apparent capture cross section and σ_n is the real capture cross section.

5.1.2 Sputtering induced defects in GaAs

As discussed in the results chapter, sputter induced defects in GaAs were studied next. *I-V* and *C-V* measurements were conducted to characterize the effect of sputtering on the Schottky barrier diodes. It was concluded that this technique results in diodes with a noticeable increase in ideality factor and Schottky barrier heights as well as the reverse leakage current. The increase in leakage current was not much above the saturation current indicating that thermionic emission is still the main current transport mechanisms. The net donor concentration vs depth was measured to show that the defects in sputtered samples were concentered close to the interface defects.

Furthermore, conventional DLTS measurements showed 6 defects (S1, S2, S3, S4, S5 and S6) however, Laplace DLTS measurements indicated that the S6 defect consisted of 2 components (S6a and S6b). The results also indicate that three of these defects were metastable and the S3 and S5 defects were transformed into each other under specific conditions. The S1 defect was metastable as well but we have not observed a metastable partner. We found that the S4 defect was highly carrier density dependent, and there was an extra peak S2 which was only observed in one 1.0×10^{16} cm^{-3} doped samples, which we could not explain.

Using Arrhenius plots, the activation energies and apparent capture cross sections were measured and results were reported in Table 5.2. By comparing the sputter-induced defects results with the irradiation-induced defects and EL2 defect from control samples, we found that these defects did not have the same origin and the Laplace DLTS measurements showed that the S6 components do not directly correspond to the EL2 defect.

Introduction and removal of the S3 and S5 metastable defects were investigated under specific conditions (applied reverse – 2 V bias to transform S5 to S3 and 0 V bias for introducing S5 and removed S3 at 400 K). Afterwards the samples were cooled down (under the same bias conditions) to a specific temperature and measured under reverse bias –1 V. After that the pre-factor of this transformation was measured and resulted in 4×10^{21} s^{-1} to transform S3 to S5 and 3×10^{15} s^{-1} for transforming the S5 to S3, which this pre-factor is related to free carrier emission but for the 4×10^{21} s^{-1} prefactor is larger than would be expected for direct free-carrier capture by a potential well with a large capture cross-section. The activation energies of these measurements are 1.69 and 1.46

eV and by comparing the results with the other reports we concluded that they are related to arsenic vacancy (V_{As}) diffusion.

Depth profiles were studied for S3, S4 and S5 defects for three different carrier densities. It was found that the S4 defect was closer to the surface compared to the other defects. Defects in the 1.0×10^{15} cm^{-3} sample were deeper below the Schottky junction. This may be explained by enhanced diffusion in the depletion region, possibly due to the charge state of the defects or due to the electric field in the depletion region. The sputtered defects were highly concentrated at the surface and with their concentration decaying at greater depth. The electric field enhanced emission from the defects was also studied and it was found that the emission of carriers from S3 and S4 could be explained by a combination of the Poole-Frenkel effect and phonon-assisted tunnelling. For the S5 defect, only phonon-assisted tunnelling fitted the data. The capture cross-section of S3, S4 and S5 investigated and the results of S5 plots are higher than the S4 and S5 defects. The real capture cross-section of S3, S4 and S5 defects were measured and they are of the order of 10^{-18} cm^2 for S3 and S4 defects and of the order of 10^{-17} cm^2 for the S5 defect. The capture barrier and high temperature limit of capture cross-section measured for each defect and for the S5 (0.33 eV, 5.75×10^{-12} cm^2) was higher than S3 (0.025 eV, 3.89×10^{-18} cm^2) and S4 (0.053 eV, 2.69×10^{-17} cm^2).

Finally, the effect of annealing on the *I-V* characteristics was investigated and it was found that the annealing initially improved the ideality factor and increased the Schottky barrier heights although at higher temperatures, the diodes degraded.

Table 5.2. Properties of the Sputtered induced defects in GaAs that we studied.

Defect label	Origin*	E_α (eV)	σ_a (cm^2)	Stability
S1	S	0.046	3.1×10^{-13}	Metastable
S2	S	0.22	1.9×10^{-15}	Stable
S3	S	0.30	1.6×10^{-14}	Metastable (transformed to S5)
S4	S	0.55	1.0×10^{-12}	Stable
S5	S	0.56	1.3×10^{-14}	Metastable (transformed to S3))
S6a	S	0.83	8.8×10^{-13}	Stable
S6b	S	0.84	6.6×10^{-13}	Stable
EL2	N	0.82	3.2×10^{-13}	Stable

S corresponds to sputter induced defect and N is control sample.

5.2 Future work

There are more measurements to characterize the electrical properties of defects in sputtered samples as the state below:

Investigate the:

- Relation between the EL2 defect on sputtered induced defects in more depth.
- The annealing of each defect in the sputtered sample.
- The effect of different gases during sputter deposition procedure.

6 REFERENCES:

[1] F. Braun, Ueber die Stromleitung durch Schwefelmetalle, Ann. Phys. 229 (1875) 556–563. doi:10.1002/andp.18752291207.

[2] F. Guthrie, XXXI. On a relation between heat and static electricity, London, Edinburgh, Dublin Philos. Mag. J. Sci. 46 (1873) 257–266. doi:10.1080/14786447308640935.

[3] P.R. Morris, A History of the World Semiconductor Industry, 1989. doi:10.1049/PBHT012E.

[4] G. PICKARD, Means for receiving intelligence communicated by electric waves, 1906. https://patents.google.com/patent/US877451A/en (accessed January 16, 2019).

[5] J. Bardeen, W.H. Brattain, Transistor, a semiconductor triode, Proc. IEEE. 86 (1998) 29–30. doi:10.1109/JPROC.1998.658753.

[6] S.M. Tunhuma, Electrical characterization of process and irradiation induced defects in GaAs, (2016).

[7] V.M. Goldschmidt, Crystal structure and chemical constitution, Trans. Faraday Soc. 25 (1929) 253. doi:10.1039/tf9292500253.

[8] E.. Schubert, Light-Emitting Diodes (3rd Edition) - E. Fred Schubert - Google Books, (n.d.). https://books.google.co.za/books/about/Light_Emitting_Diodes_Second_Edition_200.html?id=algLBgAAQBAJ&redir_esc=y (accessed June 5, 2018).

[9] Gallium Arsenide Semiconductor, (n.d.). https://www.electrical4u.com/gallium-arsenide-semiconductor/ (accessed June 6, 2018).

[10] Y.A. Du, S. Sakong, P. Kratzer, As vacancies, Ga antisites, and Au impurities in zinc blende and wurtzite GaAs nanowire segments from first principles, Phys. Rev. B - Condens. Matter Mater. Phys. 87 (2013) 075308. doi:10.1103/PhysRevB.87.075308.

[11] E.G. Seebauer, M.C. Kratzer, Charged semiconductor defects: Structure, thermodynamics and diffusion, 2009. doi:10.1017/CBO9781107415324.004.

[12] J.S. Blakemore, Semiconducting and other major properties of gallium arsenide, J. Appl. Phys. 53 (1982) R123–R181. doi:10.1063/1.331665.

[13] S.M. Sze, K.K. Ng, Physics of semiconductor devices, Wiley-Interscience, 2007. https://www.wiley.com/en-us/Physics+of+Semiconductor+Devices%2C+3rd+Edition-p-9780471143239 (accessed July 9, 2018).

[14] A. Fox, A. Fox, Optical Properties of Solids (Oxford Master Series in Condensed Matter Physics), Oxford Master Ser. (2001). doi:10.1119/1.1691372.

[15] K. Mylvaganam, Y. Chen, W. Liu, M. Liu, L. Zhang, Hard thin films: Applications and challenges, in: Anti-Abrasive Nanocoatings Curr. Futur. Appl., Elsevier, 2014: pp. 544–

567. doi:10.1016/B978-0-85709-211-3.00021-2.

[16] P. Capper, P. Rudolph, Crystal Growth Technology: Semiconductors and Dielectrics, Wiley-VCH, 2010. doi:10.1002/9783527632879.

[17] T. Nishinaga, HANDBOOK OF CRYSTAL GROWTH, in: Fundamentals, 1993: p. ii. doi:10.1016/B978-0-444-88908-9.50001-2.

[18] H.J. Scheel, Control of Epitaxial Growth Modes for High-Performance Devices, in: Cryst. Growth Technol., John Wiley & Sons, Ltd, Chichester, UK, n.d.: pp. 621–644. doi:10.1002/0470871687.ch28.

[19] D. V. Morgan, K. Board, An introduction to semiconductor microtechnology, J. Wiley, 1990. https://books.google.co.za/books?id=yQ5TAAAAMAAJ&pg=PA23&redir_esc=y (accessed September 22, 2018).

[20] P.D. Dapkus, H.M. Manasevit, K.L. Hess, T.S. Low, G.E. Stillman, High purity GaAs prepared from trimethylgallium and arsine, J. Cryst. Growth. 55 (1981) 10–23. doi:10.1016/0022-0248(81)90265-7.

[21] M. Kawabe, T. Ueda, H. Takasugi, \nInitial Stage and Domain Structure of GaAs Grown on Si(100) by Molecular Beam Epitaxy\n, Jpn. J. Appl. Phys. 26 (1987) L114–L116. doi:10.1143/JJAP.26.L114.

[22] J. Boisvert, D. Law, R. King, D. Bhusari, X. Liu, A. Zakaria, W. Hong, S. Mesropian, D. Larrabee, R. Woo, A. Boca, K. Edmondson, D. Krut, D. Peterson, K. Rouhani, B. Benedikt, N.H. Karam, Development of advanced space solar cells at Spectrolab, Photovolt. Spec. Conf. (PVSC), 2010 35th IEEE. (2010) 1–4. doi:10.1109/PVSC.2010.5614522.

[23] E. Yablonovitch, O.D. Miller, S.R. Kurtz, The opto-electronic physics that broke the efficiency limit in solar cells, in: Conf. Rec. IEEE Photovolt. Spec. Conf., IEEE, 2012: pp. 1556–1559. doi:10.1109/PVSC.2012.6317891.

[24] X. Wang, M.R. Khan, J.L. Gray, M.A. Alam, M.S. Lundstrom, Design of gaas solar cells operating close to the shockley-queisser limit, IEEE J. Photovoltaics. 3 (2013) 737–744. doi:10.1109/JPHOTOV.2013.2241594.

[25] A.D. Holland, A.D.T. Short, T. Cross, X-ray detection using bulk GaAs, Nucl. Inst. Methods Phys. Res. A. 346 (1994) 366–371. doi:10.1016/0168-9002(94)90724-2.

[26] U. Roland, C. Renschen, D. Lippik, F. Stallmach, F. Holzer, A new fiber optical thermometer and its application for process control in strong electric, magnetic, and electromagnetic fields, Sens. Lett. 1 (2003) 93–98. doi:10.1166/sl.2003.002.

[27] D.T. Pierce, R.J. Celotta, G.C. Wang, W.N. Unertl, A. Galejs, C.E. Kuyatt, S.R. Mielczarek, The GaAs spin polarized electron source, Rev. Sci. Instrum. 51 (1980) 478–499. doi:10.1063/1.1136250.

[28] K. Tateoka, A. Sugimura, H. Furukawa, N. Yoshikawa, K. Kanazawa, A GaAs MCM Power Amplifier of 3.6 V Operation with High Efficiency of 49% for 0.9 GHz Digital Cellular Phone Systems, IEEE Trans. Microw. Theory Tech. 43 (1995) 2539–2542.

doi:10.1109/22.473175.

[29] M.W. Thompson, M. W., Defects and Radiation Damage in Metals, Defects Radiat. Damage Met. by M. W. Thompson, Cambridge, UK Cambridge Univ. Press. 1974. (1974). http://adsabs.harvard.edu/abs/1974drdm.book.....T (accessed July 22, 2019).

[30] V.A.J. van Lint, T.M. Flanagan, R.E. Leadon, J.A. Naber, V.C. Rogers, Mechanisms of radiation effects in electronic materials. Volume 1, Res. Support. by U.S. Def. Nucl. Agency. New York, Wiley-Interscience, 1980. 370 P. 81 (1980). http://adsabs.harvard.edu/abs/1980STIA...8113073V (accessed July 22, 2019).

[31] D. V. Lang, Deep-level transient spectroscopy: A new method to characterize traps in semiconductors, J. Appl. Phys. 45 (1974) 3023–3032. doi:10.1063/1.1663719.

[32] K. Iniewski, Radiation Effects in Semiconductors (Google eBook), CRC Press, 2010. http://books.google.com/books?id=zO6C4fcY7WIC&pgis=1 (accessed June 7, 2018).

[33] D. V. Lang, R.A. Logan, L.C. Kimerling, Identification of the defect state associated with a gallium vacancy in GaAs and AlxGa1-xAs, Phys. Rev. B. 15 (1977) 4874–4882. doi:10.1103/PhysRevB.15.4874.

[34] F.D. Auret, S.A. Goodman, G. Myburg, W.O. Barnard, Electrical characterization of sputter-deposition-induced defects in epitaxially grown n-GaAs layers, Vacuum. 46 (1995) 1087–1090. doi:10.1016/0042-207X(95)00112-3.

[35] Y. Leclerc, F.D. Auret, S.A. Goodman, G. Myburg, C. Schutte, Electronic properties of defects introduced during sputter deposition of Cr Schottky contacts on GaAs, in: Ion Beam Modif. Mater., Elsevier, 1996: pp. 870–873. doi:10.1016/B978-0-444-82334-2.50170-2.

[36] L. Dobaczewski, P. Kaczor, I.D. Hawkins, A.R. Peaker, Laplace transform deep-level transient spectroscopic studies of defects in semiconductors, J. Appl. Phys. 76 (1994) 194–198. doi:10.1063/1.357126.

[37] Y. Zengliang, Introduction to Ion Beam Biotechnology, Springer, 2006. doi:10.1007/b135662.

[38] G.D. Watkins, Intrinsic defects in silicon, Mater. Sci. Semicond. Process. 3 (2000) 227–235. doi:10.1016/S1369-8001(00)00037-8.

[39] K. Nordlund, R.S. Averback, Role of self-interstitial atoms on the high temperature properties of metals, Phys. Rev. Lett. 80 (1998) 4201–4204. doi:10.1103/PhysRevLett.80.4201.

[40] Y. Nishi, R. Doering, Handbook of Semiconductor Manufacturing Technology, Second Edition, CRC Press, 2007. doi:10.1201/9781420017663.

[41] S.-J.L. Kang, 12 – SINTERING ADDITIVES AND DEFECT CHEMISTRY, in: Sintering, Elsevier, 2005: pp. 173–179. doi:10.1016/B978-075066385-4/50012-1.

[42] Mouritz A, Strengthening of metal alloys, in: Introd. to Aerosp. Mater., Elsevier, 2012: pp. 57–90. doi:10.1533/9780857095152.57.

[43] H. Hausmann, A. Pillukat, P. Ehrhart, Point defects and their reactions in electron-irradiated GaAs investigated by optical absorption spectroscopy, Phys. Rev. B - Condens. Matter Mater. Phys. 54 (1996) 8527–8539. doi:10.1103/PhysRevB.54.8527.

[44] IMPERFECTIONS OF CRYSTAL LATTICES, (2002) 1–20. http://www.substech.com/dokuwiki/doku.php?id=imperfections_of_crystal_structure (accessed January 16, 2019).

[45] J. Callaway, A. Isabel, B. Santa, C. Science, 1 - Electrons and holes in a semiconductor, Elsevier, 2014. doi:http://dx.doi.org/10.1533/9781782422242.1.

[46] P. Lejček, Grain Boundaries: Description, Structure and Thermodynamics, in: Springer, Berlin, Heidelberg, 2010: pp. 5–24. doi:10.1007/978-3-642-12505-8_2.

[47] L.E. Murr, Volume defects: 3D imperfections in crystals, in: Handb. Mater. Struct. Prop. Process. Perform., Springer International Publishing, Cham, 2015: pp. 313–324. doi:10.1007/978-3-319-01905-5_17-1.

[48] C.P. Poole, Encyclopedic dictionary of condensed matter physics: Volume 1 A-M, Elsevier, 2004. https://books.google.co.za/books?hl=en&lr=&id=CXwrqM2hU0EC&oi=fnd&pg=PP1&dq=Poole,+C.+(2004).+Encyclopedic+dictionary+of+condensed+matter+physics.+1st+ed.+Amsterdam:+Elsevier.&ots=Y5avnvnkWh&sig=iyX0GxawfRHfVHGOwBmo7H8QsCM#v=onepage&q&f=false (accessed August 3, 2018).

[49] C. Honsberg, S. Bowden, Current Losses Due To Recombination, (n.d.). https://www.pveducation.org/pvcdrom/design/current-losses-due-to-recombination (accessed January 18, 2019).

[50] A. Hallén, M. Bakowski, Combined proton and electron irradiation for improved GTO thyristors, Solid State Electron. 32 (1989) 1033–1037. doi:10.1016/0038-1101(89)90167-6.

[51] F.D. Auret, P.N.K. Deenapanray, Deep level transient spectroscopy of defects in high-energy light-particle irradiated Si, Crit. Rev. Solid State Mater. Sci. 29 (2004) 1–44. doi:10.1080/10408430490442458.

[52] J.C. Bourgoin, H.J. von Bardeleben, D. Stievenard, Irradiation Induced Defects in III–V Semiconductor Compounds, Phys. Status Solidi. 102 (1987) 499–510. doi:10.1002/pssa.2211020205.

[53] J.H. Warner, S.R. Messenger, R.J. Walters, G.P. Summers, M.J. Romero, E.A. Burke, Displacement damage evolution in GaAs following electron, proton and silicon ion irradiation, in: IEEE Trans. Nucl. Sci., 2007: pp. 1961–1968. doi:10.1109/TNS.2007.910328.

[54] N. Chen, S. Gray, E. Hernandez-Rivera, D. Huang, P.D. Levan, F. Gao, Computational simulation of threshold displacement energies of GaAs, J. Mater. Res. 32 (2017) 1555–1562. doi:10.1557/jmr.2017.46.

[55] F. Gao, W.J. Weber, R. Devanathan, Defect production, multiple ion-solid interactions and amorphization in SiC, Nucl. Instruments Methods Phys. Res. Sect. B Beam Interact.

with Mater. Atoms. 191 (2002) 487–496. doi:10.1016/S0168-583X(02)00598-0.

[56] B. Lehmann, D. Bräunig, A deep-level transient spectroscopy variation for the determination of displacement threshold energies in GaAs, J. Appl. Phys. 73 (1993) 2781–2785. doi:10.1063/1.353054.

[57] A.L. Barry, R. Maxseiner, R. Wojcik, M.A. Briere, D. Bräunig, An improved displacement damage monitor, IEEE Trans. Nucl. Sci. 37 (1990) 1726–1731. doi:10.1109/23.101183.

[58] K. Nordlund, J. Peltola, J. Nord, J. Keinonen, R.S. Averback, Defect clustering during ion irradiation of GaAs: Insight from molecular dynamics simulations, J. Appl. Phys. 90 (2001) 1710–1717. doi:10.1063/1.1384856.

[59] S. Mahajan, Growth- and processing-induced defects in semiconductors, Prog. Mater. Sci. 33 (1989) 1–84. doi:10.1016/0079-6425(89)90003-0.

[60] L.S. Weinman, S.A. Jamison, M.J. Helix, Sputtered TiW/Au Schottky barriers on GaAs, J. Vac. Sci. Technol. 18 (1981) 838–840. doi:10.1116/1.570958.

[61] S.J. Fonash, S. Ashok, R. Singh, Effect of ion-beam sputter damage on Schottky barrier formation in silicon, Appl. Phys. Lett. 39 (1981) 423–425. doi:10.1063/1.92738.

[62] D.A. Vandenbroucke, R.L. Van Meirhaeghe, W.H. Laflère, F. Cardon, Sputter-induced damage in Al/n-GaAs and Al/p-GaAs Schottky barriers, Semicond. Sci. Technol. 2 (1987) 293–298. doi:10.1088/0268-1242/2/5/008.

[63] Schottky, Walter Hans | Encyclopedia.com, (n.d.). https://www.encyclopedia.com/science/dictionaries-thesauruses-pictures-and-press-releases/schottky-walter-hans (accessed July 20, 2019).

[64] E.H. Rhoderick, R.H. Williams, Metal-semiconductor contacts, Clarendon Press, 1988. https://books.google.co.za/books?id=0zcoAQAAMAAJ&q=Rhoderick,+williams,+metal+semiconductor+contacts.+1988&dq=Rhoderick,+williams,+metal+semiconductor+contacts.+1988&hl=en&sa=X&ved=0ahUKEwikv4PliN3cAhXIBcAKHZwUDw8Q6AEIKDAA (accessed August 8, 2018).

[65] D. Neamen, Semiconductor Physics and Devices: Basic Principles 4th ed, (2011) 768. https://pdfs.semanticscholar.org/bbe0/84bff4b612b7e3acfd33ab1ff376f86e7bfc.pdf (accessed May 8, 2018).

[66] C.Y. Chang, F. Kai, GaAs High-Speed Devices: Physics, Technology, and Circuit Applications, Wiley, 1994. https://books.google.co.za/books?hl=en&lr=&id=S3KyulONSSMC&oi=fnd&pg=PR13&dq=GaAs+high-speed+devices,chang+and+kai,+1994&ots=ZLagPoMJPA&sig=BdU-rxMTdUP-vLjZzKi7oH6UkGA#v=onepage&q=GaAs high-speed devices%2Cchang and kai%2C 1994&f=false (accessed June 5, 2018).

[67] S.S. Li, Semiconductor physical electronics, Springer, 2006.

[68] M. Grundmann, The physics of semiconductors: an introduction including nanophysics and applications (hardback)(series: graduate texts in physics), Springer, 2010.

doi:10.1007/978-3-642-13884-3.

[69] G. Myburg, F.D. Auret, W.E. Meyer, C.W. Louw, M.J. Van Staden, Summary of Schottky barrier height data on epitaxially grown n- and p-GaAs, Thin Solid Films. 325 (1998) 181–186. doi:10.1016/S0040-6090(98)00428-3.

[70] B.J. Streetman, S.K. Banerjee, Solid State Electronic Devices, Pearson Education, 1980. http://lib.hpu.edu.vn/handle/123456789/29081 (accessed July 10, 2018).

[71] W. Shockley, W.T. Read, Statistics of the recombinations of holes and electrons, Phys. Rev. 87 (1952) 835–842. doi:10.1103/PhysRev.87.835.

[72] R.N. Hall, Electron-hole recombination in germanium [21], Phys. Rev. 87 (1952) 387. doi:10.1103/PhysRev.87.387.

[73] E.F. Schubert, Doping in III-V Semiconductors, Cambridge University Press, 2015. https://books.google.co.za/books/about/Doping_in_III_V_Semiconductors.html?id=_dMiJfCmLFoC&redir_esc=y (accessed July 11, 2018).

[74] J. Bourgoin, M. Lannoo, Point Defects in Semiconductors II, Springer Berlin Heidelberg, Berlin, Heidelberg, 1983. doi:10.1007/978-3-642-81832-5.

[75] S. Ganichev, E. Ziemann, W. Prettl, I. Yassievich, Distinction between the Poole-Frenkel and tunneling models of electric-field-stimulated carrier emission from deep levels in semiconductors, Phys. Rev. B - Condens. Matter Mater. Phys. 61 (2000) 10361–10365. doi:10.1103/PhysRevB.61.10361.

[76] W.E. Meyer, Digital DLTS studies on radiation induced defects in by Walter Ernst Meyer PhD (Physics) in the Faculty of Natural & Agricultural Science University of Pretoria November 2006 Supervisor : Prof F D Auret Digital DLTS studies on radiation induced defects, (2006) 0–5.

[77] L. Romano, V. Privitera, C. (Chennupati) Jagadish, Defects in semiconductors, n.d. https://books.google.co.za/books?id=eu6cBAAAQBAJ&pg=PA376&lpg=PA376&dq=Naoya+Iwamoto,+Bengt+G.+Svensson,+2015&source=bl&ots=n0fbO_Ur5t&sig=ACfU3U1lkL2siB-xFLFeK3CA99i-mnAMOA&hl=en&sa=X&ved=2ahUKEwi4h5vCxNzjAhWVQhUIHXmKC-oQ6AEwBHoECAkQAQ#v=onepage&q=Naoya (accessed July 30, 2019).

[78] A. Schulman, L.F. Lanosa, C. Acha, Poole-Frenkel effect and Variable-Range Hopping conduction in metal / YBCO resistive switching devices, (2015). http://arxiv.org/abs/1505.05813 (accessed July 30, 2019).

[79] S. Makram-Ebeid, Effect of electric field on deep-level transients in GaAs and GaP, Appl. Phys. Lett. 37 (1980) 464–466. doi:10.1063/1.91966.

[80] D. Pons, S. Makram-Ebeid, Phonon assisted tunnel emission of electrons from deep levels in GaAs, J. Phys. 40 (1979) 1161–1172. doi:10.1051/jphys:019790040012011610O.

[81] S.D. Ganichev, W. Prettl, I.N. Yassievich, Deep impurity-center ionization by far-infrared radiation, Phys. Solid State. 39 (1997) 1703–1726. doi:10.1134/1.1130157.

[82] J. Pienaar, W.E. Meyer, F.D. Auret, S.M.M. Coelho, Comparison of two models for phonon assisted tunneling field enhanced emission from defects in Ge measured by DLTS, in: Phys. B Condens. Matter, 2012: pp. 1641–1644. doi:10.1016/j.physb.2011.09.106.

[83] Silvaco, Simulations of Deep-Level Transient Spectroscopy for 4H-SiC, (2014). https://www.silvaco.com/tech_lib_TCAD/simulationstandard/2014/apr_may_jun/a2/a2.html (accessed July 13, 2018).

[84] L.A. Kosyachenko, Solar Cells - New Approaches and Reviews, InTech, 2015. doi:10.5772/58490.

[85] J. Wei, Deep Level Transient Spectroscopy Using HF2LI Lock-in Amplifier, (2015). http://www.zhinst.com/blogs/jamesw/deep-level-transient-spectroscopy/ (accessed July 16, 2018).

[86] L. Dobaczewski, A.R. Peaker, K. Bonde Nielsen, Laplace-transform deep-level spectroscopy: The technique and its applications to the study of point defects in semiconductors, J. Appl. Phys. 96 (2004) 4689–4728. doi:10.1063/1.1794897.

[87] Moore. Walter J., Physical chemistry, 5th Ed. [Harlow] Longman Sci. Tech. (1972) 977. https://trove.nla.gov.au/work/10374565?q&sort=holdings+desc&_=1531819531933&versionId=45752546 (accessed July 17, 2018).

[88] M. Mikelsen, E. V. Monakhov, G. Alfieri, B.S. Avset, B.G. Svensson, Kinetics of divacancy annealing and divacancy-oxygen formation in oxygen-enriched high-purity silicon, Phys. Rev. B - Condens. Matter Mater. Phys. 72 (2005) 195207. doi:10.1103/PhysRevB.72.195207.

[89] A. Khan, Y. Masafumi, Deep Level Transient Spectroscopy: A Powerful Experimental Technique for Understanding the Physics and Engineering of Photo-Carrier Generation, Escape, Loss and Collection Processes in Photovoltaic Materials, in: Sol. Cells - New Approaches Rev., InTech, 2015. doi:10.5772/59419.

[90] A.W. Barnard, Electrical characterization of alpha- particle irradiation-induced defects in germanium, (2017).

[91] D. V Lang, Thermally Stimulated Relaxation in Solids, in: P. Bräunlich (Ed.), Top. Appl. Phys., Springer Berlin Heidelberg, Berlin, Heidelberg, 1979: p. 93. doi:10.1007/3-540-09595-0.

[92] Y. Zohta, M.O. Watanabe, On the determination of the spatial distribution of deep centers in semiconducting thin films from capacitance transient spectroscopy, J. Appl. Phys. 53 (1982) 1809–1811. doi:10.1063/1.330683.

[93] S. Goodman, Influence of particle irradiation on the electrical and defect properties of GaAs, (1994). http://nrfnexus.nrf.ac.za/handle/20.500.11892/178814 (accessed December 14, 2018).

[94] Polifab magnetron Sputtering System LEYBOLD, (n.d.). http://www.polifab.polimi.it/equipments/magnetron-sputtering-system-leybold-lh-z400/ (accessed August 1, 2018).

[95] Stanford Advanced Materials, What is sputtering?, (n.d.). http://www.ajaint.com/what-is-sputtering.html (accessed August 1, 2018).

[96] J. Schmidt, K. Bothe, Structure and transformation of the metastable boron- and oxygen-related defect center in crystalline silicon, Phys. Rev. B. 69 (2004) 024107. doi:10.1103/PhysRevB.69.024107.

[97] Diode IV-Characteristics, (n.d.). http://people.seas.harvard.edu/~jones/es154/lectures/lecture_2/diode_characteristics/diode_characteristics.html (accessed March 22, 2019).

[98] J.W. Farmer, D.C. Look, D.C. Look, Electron Irradiation Defects in n-type GaAs Electron-irradiation defects in n-type GaAs, Phys. Rev. B. 21 (1980) 3389–3398. http://corescholar.libraries.wright.edu/physics (accessed March 23, 2018).

[99] P.A. Murawala, V.A. Singh, S. Subramanian, S.S. Chandvankar, B.M. Arora, Origin of an E 3 -like defect in GaAs and Ga As 1 − x Sb x alloys, Phys. Rev. B. 29 (1984) 4807–4810. doi:10.1103/PhysRevB.29.4807.

[100] P.A. Schultz, The E1-E2 center in gallium arsenide is the divacancy, J. Phys. Condens. Matter. 27 (2015) 075801. doi:10.1088/0953-8984/27/7/075801.

[101] D. Pons, J.C. Bourgoin, Irradiation-induced defects in GaAs, J. Phys. C Solid State Phys. 18 (1985) 3839–3871. doi:10.1088/0022-3719/18/20/012.

[102] D. Stievenard, X. Boddaert, J.C. Bourgoin, H.J. von Bardeleben, Behavior of electron-irradiation-induced defects in GaAs, Phys. Rev. B. 41 (1990) 5271–5279. doi:10.1103/PhysRevB.41.5271.

[103] H.J. Von Bardeleben, J.C. Bourgoin, A. Miret, Identification of the arsenic-antisite-arsenic-vacancy complex in electron-irradiated GaAs, Phys. Rev. B. 34 (1986) 1360–1362. doi:10.1103/PhysRevB.34.1360.

[104] J.T. Schick, C.G. Morgan, P. Papoulias, First-principles study of As interstitials in GaAs: Convergence, relaxation, and formation energy, Phys. Rev. B - Condens. Matter Mater. Phys. 66 (2002) 1953021–19530210. doi:10.1103/PhysRevB.66.195302.

[105] F.D. Auret, L.J. Bredell, G. Myburg, W.O. Barnard, Simultaneous observation of sub- and above threshold electron irradiation induced defects in gaas, Jpn. J. Appl. Phys. 30 (1991) 80–83. doi:10.1143/JJAP.30.80.

[106] F.D. Auret, M. Nel, A.W.R. Leitch, A DLTS analysis of electron and hole traps in VPE grown n-GaAs using schottky barrier diodes, J. Electron. Mater. 17 (1988) 111–113. doi:10.1007/BF02652139.

[107] F. Danie Auret, S.A. Goodman, W.E. Meyer, Electronic Properties and Introduction Kinetics of a Metastable Radiation Induced Defect in n-GaAs, Mater. Sci. Forum. 196–201 (1995) 1067–1072. doi:10.4028/www.scientific.net/MSF.196-201.1067.

[108] A. Telia, B. Lepley, C. Michel, Experimental analysis of temperature dependence of deep-level capture cross-section properties at the Au oxidized InP interface, J. Appl. Phys. 69 (1991) 7159–7165. doi:10.1063/1.347607.

[109] A. Mitonneau, A. Mircea, G.M. Martin, D. Pons, Electron and hole capture cross-sections at deep centers in gallium arsenide, Rev. Phys. Appliquée. 14 (1979) 853–861. doi:10.1051/rphysap:019790014010085300.

[110] V. Bondarenko, J. Gebauer, F. Redmann, R. Krause-Rehberg, Vacancy formation in GaAs under different equilibrium conditions, Appl. Phys. Lett. 87 (2005) 161906. doi:10.1063/1.2084330.

[111] A. Venter, C. Nyamhere, J.R. Botha, F.D. Auret, P.J. Janse van Rensburg, W.E. Meyer, S.M.M. Coelho, V. l. Kolkovsky, Ar plasma induced deep levels in epitaxial *n* -GaAs, J. Appl. Phys. 111 (2012) 013703. doi:10.1063/1.3673322.

[112] W.R. Buchwald, G.J. Gerardi, E.H. Poindexter, N.M. Johnson, H.G. Grimmeiss, D.J. Keeble, Electrical and optical characterization of metastable deep-level defects in GaAs, Phys. Rev. B. 40 (1989) 2940–2945. doi:10.1103/PhysRevB.40.2940.

[113] A.B. Conibear, A.W.R. Leitch, C.A.B. Ball, Third metastable hydrogen-related level in n - type GaAs, Phys. Rev. B. 47 (1993) 1846–1848. doi:10.1103/PhysRevB.47.1846.

[114] G. Pfeiffer, J. Weber, Metastable Defects in N-Type GaAs Related to Hydrogen, Mater. Sci. Forum. 143–147 (1993) 873–878. doi:10.4028/www.scientific.net/MSF.143-147.873.

[115] K.M. Luken, R.A. Morrow, Diffusing arsenic vacancies and their interaction with the native defect EL2 in GaAs, J. Appl. Phys. 79 (1996) 1388–1390. doi:10.1063/1.361037.

[116] J.C. Hu, M.D. Deal, J.D. Plummer, Modeling the diffusion of implanted Be in GaAs, J. Appl. Phys. 78 (1995) 1606–1613. doi:10.1063/1.360254.

[117] J.J. Murray, M.D. Deal, E.L. Allen, D.A. Stevenson, S. Nozaki, Modeling Silicon Diffusion in GaAs Using Well Defined Silicon Doped Molecular Beam Epitaxy Structures, J. Electrochem. Soc. 139 (1992) 2037. doi:10.1149/1.2221170.

[118] L.B. Guoba, A.A. Vitkauskas, J. V. Kameneckas, V.R. Sargūnas, A.P. Sakalas, The Influence of Ion-Irradiation on Interdiffusion and Annealing Behavior of Ohmic Contacts to GaAs, Phys. Status Solidi. 111 (1989) 507–513. doi:10.1002/pssa.2211110215.

[119] A. Chantre, Introduction to defect bistability, Appl. Phys. A Solids Surfaces. 48 (1989) 3–9. doi:10.1007/BF00617758.

[120] C.H. Henry, D. V. Lang, Nonradiative capture and recombination by multiphonon emission in GaAs and GaP, Phys. Rev. B. 15 (1977) 989–1016. doi:10.1103/PhysRevB.15.989.

Appendix: publications

IOP Publishing Semiconductor Science and Technology
Semicond. Sci. Technol. 33 (2018) 125011 (8pp) https://doi.org/10.1088/1361-6641/aae9a8

Laplace DLTS study of the fine structure and metastability of the radiation-induced E3 defect level in GaAs

F Taghizadeh, K Ostvar, F D Auret and W E Meyer

Department of Physics, University of Pretoria, Private Bag X20, Hatfield 0028, Pretoria, South Africa

E-mail: F.Taghizadeh@tuks.co.za

Received 1 August 2018, revised 8 October 2018
Accepted for publication 19 October 2018
Published 5 November 2018

Abstract

In this paper we used high-resolution Laplace deep-level transient spectroscopy (DLTS) to study the electrical properties of the E3 defect family introduced in GaAs by MeV electron irradiation. We found that the peak conventionally referred to as the E3 contained 3 components which we labeled E3a, E3b and E3c, with E3a being the most prominent component. The activation energy of E3a for different carrier densities varied between 0.36 and 0.375 eV. From dopant dependent introduction rate measurements, we found that the introduction rates of the E3a and E3b defect did not depend on doping density. However, the E3c concentration increased with increasing carrier density. Furthermore, the E3c was found to be metastable: it was reversibly removed during minority carrier injection at low temperatures and re-introduced by annealing above 160 K under zero bias. Interestingly, annealing measurements revealed that, of the three components, the E3b annealed first at around 500 K while both the other components annealed together at a higher temperature of 525 K. By comparing our results with previous studies, we concluded that the origin of E3a is V_{As}, E3b is As_i and E3c is V_{Ga}–Si_{Ga}.

Keywords: electron irradiation-induced defects in GaAs, Laplace deep-level transient spectroscopy, metastability, introduction rate, defect annealing, defect structure

(Some figures may appear in colour only in the online journal)

1. Introduction

Deep-level transient spectroscopy (DLTS) was introduced by Lang in 1974 [1]. This powerful technique is used to analyze deep level defects in semiconductors [1, 2]. The major shortcomings of DLTS are the lack of structural information and limited spectral resolution [3]. Laplace deep-level transient spectroscopy was introduced by Dobaczewski and Peaker [3] to overcome the spectral resolution shortcoming of DLTS. This technique has a higher resolution than DLTS and is capable of separating defects which have very similar carrier emission rates.

Deep- and shallow-level defects significantly affect the electrical properties of semiconductors. These defects can be introduced during crystal growth or processing steps such as ion implantation, metallization, etching and annealing [4]. In order to fully understand the origin and effect of a defect, factors that should be considered include: deep-level introduction method, doping density and temperature, crystal growth method and defect annealing dynamics.

Gallium arsenide (GaAs) is a III–V, direct band gap semiconductor. It has high electron mobility and a moderately wide band gap (1.424 eV). Because of these properties, it is a suitable candidate for high-frequency applications such as satellite communications and microwave point-to-point links. In this article, the aim is to investigate the E3 defect introduced in epitaxially-grown gallium arsenide by MeV electron irradiation.

Since the first detection of the E1, E2 and E3 radiation-induced defect levels in GaAs by Lang *et al* in 1977 [5], there have been many speculations regarding their possible nature and origin. Lang *et al* [5] concluded that the origins of the E1 and E2 are Ga_i or As_{Ga}, with which Farmer *et al* [6] agreed. However, the results of Pons *et al* [7] and Stievenard [8] show

that both the E1 and E2 are due to V_{As} while in 2015 Schultz [9] used DFT calculations to prove that these two levels are due to the divacancy. From DLTS results and Hall measurements, Lang [5] and Farmer [6] both proposed that E3 is a V_{Ga}. However, from a study combining theory and DLTS, Murawala *et al* [10] concluded that E3 is a V_{As}. This conclusion was also recently supported by Schultz using DFT (using LDA and PBE) [9]. On the other hand, several authors proposed that the E3 consists of defect pairs: Pons *et al* [7] and Stievenard [8] using EPR found evidence for the V_{As}–As_i, and Bardeleben *et al* [11] using EPR for the As_{Ga}–V_{As}. The E3 was also proposed to be the antisite As_{Ga} by Schick *et al* [12].

For this work, GaAs samples were irradiated by beta radiation emanating from ^{90}Sr to introduce point defects. The MeV electrons from this source have sufficient kinetic energy to displace at least one single atom [7]. Using L-DLTS, we found that the E3 level observed in conventional DLTS actually consists of three defect levels with distinct properties. These results can be used to reconcile apparently conflicting results regarding the origin of the E3 level.

2. Experimental procedures

For this experiment we used small rectangularly shaped pieces of n-type OMVPE-grown GaAs on n^{++} GaAs substrates. GaAs was used from various wafers with different silicon doping densities with free carrier densities of 7.1×10^{14}, 1.9×10^{15} and $1.0 \times 10^{16}\,cm^{-3}$. The samples were degreased by boiling in trichloroethylene for 3 min and then boiled in isopropanol for another 3 min. After that, the pieces were rinsed with deionized water, then, for chemical etching, the samples were dipped in a solution of H_2O [100%]: H_2O_2 [50%]: NH_4OH [25%] with (100:1:3) volume ratios for 60 s. Hereafter the samples were again rinsed in deionized water and then dipped in a solution of $6\,mol\,dm^{-3}$ HCl for 60 s and finally rinsed in deionized water and blow-dried by nitrogen gas. Next, the samples were positioned in a resistive evaporation chamber to deposit a layered ohmic contact (Ni (5 nm), Au–Ge (145 nm), and Ni (50 nm)) on the back surface of each sample. The deposited ohmic contacts were annealed at 450 °C for 2 min in an Ar-filled environment. The samples were cleaned again to prepare them for Schottky contact deposition. For second cleaning, we skipped the dipping in H_2O: H_2O_2: NH_4OH. The samples were positioned in the same deposition chamber and 0.6 mm diameter Au Schottky contacts were deposited on the epitaxially-grown surface of the samples through a metal contact mask.

After contact formation the samples were individually subjected to electron irradiation using ^{90}Sr source, with each sample being irradiated for specific durations, depending on their free carrier densities. This radiation was chosen so as to not affect the carrier densities at room temperature. Note that all the measure radiation induced defect are empty at room temperature because of their energy levels position in the band gap. The aim of the experiments was to confirm the existence of the E3 defect in each sample. This was achieved by using conventional DLTS. After the confirmation step, E3 was characterized using Laplace DLTS. The aim of this was to detect the finer structure of the E3 and characterize its formation and behaviour in each sample. The results were compared against each other in an attempt to determine the influence of the duration of the irradiation as well as the effect of the carrier density on the E3 center.

Electric field measurements of the E3a, the most prominent component of the E3, were done for 3 different carrier densities. The field effect data was analyzed according to the Poole–Frenkel model [13] as well as the phonon-assisted tunnelling model of Ganichev *et al* [13, 14] from which the tunnelling time could be determined. In order to gain insight into the origin of the different components, the introduction rates, annealing properties, capture cross section and possible metastability of the individual components of the E3 defect were investigated.

3. Results and discussion

Figure 1 shows the DLTS and Laplace DLTS spectrum of three different carrier densities. DLTS spectrum was recorded over the temperature range 20–300 K as shown in figure 1(b) and the Laplace DLTS spectrum of the E3 defect at 205 K is shown in figure 1(a). The DLTS spectrum demonstrates the presence of three prominent peaks: E1, E2 and E3, which were spaced far apart in temperature at approximately 30, 70 and 200 K, indicating that the energy levels are spaced well apart in the band gap. From the conventional DLTS spectrum it seems that the E3 is a single peak (albeit slightly broad and with some asymmetry for the $1.0 \times 10^{16}\,cm^{-3}$ doped GaAs). However, by using Laplace DLTS, it was clear that the E3 comprised of 3 different individual components which we labeled E3a, E3b and E3c. The properties of the three defects are listed in table 1. In the DLTS graph (figure 1(a)) we observed the comparison between the three different carrier densities. The E3 peak for the higher carrier density is shifted to the left, it is broader and it is asymmetric towards lower temperature side. The Laplace DLTS spectrum of the E3 shows that the relative amplitude of the E3c peak is enhanced at higher carrier densities, thereby explaining the shift and broadening observed in the conventional DLTS spectrum.

The Arrhenius plots of the E3 and its components (E3a, E3b and E3c) in three samples with different free carrier densities (7.1×10^{14}, 1.9×10^{15} and $1.0 \times 10^{16}\,cm^{-3}$) were plotted and showed three distinct levels, as shown in figure 2. The activation energies for all three components were close to activation energies of the E3 reported in literature. Note that the activation energy for all three components decreased with increasing free carrier density, i.e. for E3a, 0.383 eV, 0.372 eV and 0.360 eV for $7.1 \times 10^{14}\,cm^{-3}$, $1.9 \times 10^{15}\,cm^{-3}$ and $1.0 \times 10^{16}\,cm^{-3}$ free carrier concentration, respectively, but the activation energies of E3b and E3c results for $7.1 \times 10^{14}\,cm^{-3}$ are with a ± 0.01 eV error bar which is due to lower concentration of these defects compared with the higher carrier densities.

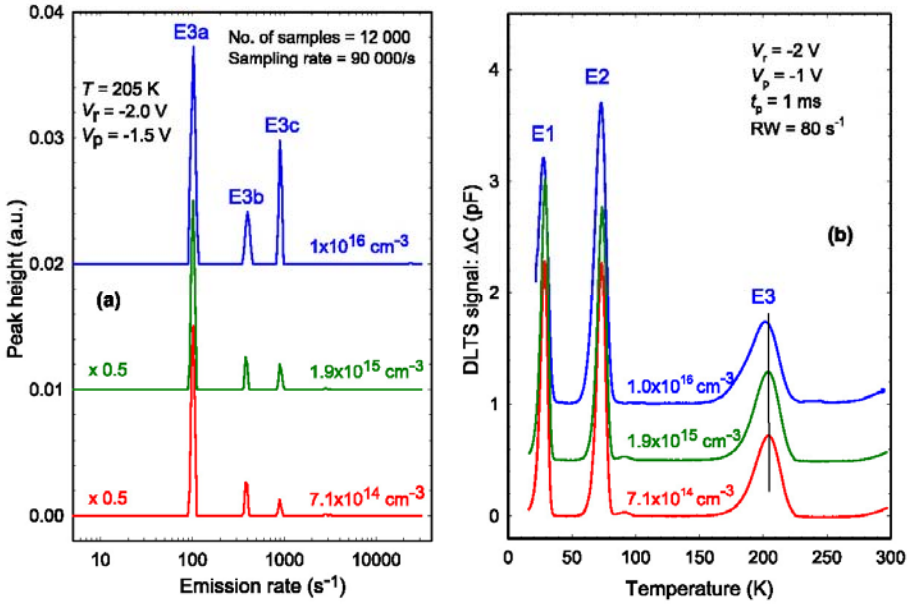

Figure 1. (a) Laplace DLTS spectra and (b) conventional DLTS of three different carrier densities: 7.1×10^{14}, 1.9×10^{15} and 1.0×10^{16} cm^{-3} doped n-GaAs. While conventional DLTS only detects one peak, Laplace DLTS is able to reveal the finer structure of the E3.

Table 1. Electronic properties of the E1–E2 defects and the E3 with its components in GaAs with a doping density of 1.9×10^{15} and 1.0×10^{16} cm^{-3}.

Defect	E_A (eV)	$\sigma_{n,a}$ (cm^2)	σ_n (cm^2)	Defect ID
E1	0.045	1.1×10^{15} [15]	—	Divacancy [9]
	0.040	1.6×10^{17} [16]		
E2	0.142	1.3×10^{13} [15]	—	Divacancy [9]
	0.140	3.0×10^{15} [16]		
E3	0.300 [7]	6.2×10^{15} [7]	—	—
	0.375 [15]	1.3×10^{14} [15]		
	0.390 [17]	6.0×10^{14} [17]		
	0.376[b]	4.1×10^{14b}		
	0.360[c]	3.2×10^{14c}		
E3a	0.380[a]	4.7×10^{14a}	3.0×10^{16a} (205 K)	V_{As}
	0.375[b]	2.9×10^{14b}	1.0×10^{16b} (205 K)	
	0.360[c]	2.1×10^{14c}	3.1×10^{17c} (205 K)	
E3b	0.383[a]	2.1×10^{13a}	—	As_i
	0.395[b]	3.4×10^{13b}		
	0.390[c]	4.8×10^{13c}		
E3c	0.338[a]	7.7×10^{14a}	—	V_{Ga}–Si_{Ga}
	0.351[b]	1.3×10^{13b}		
	0.340[c]	6.8×10^{14c}		

[a] This study, measured in material with a free carrier density of 7.1×10^{14} cm^{-3}.
[b] This study, measured in material with a free carrier density of 1.9×10^{15} cm^{-3}.
[c] This study, measured in material with a free carrier density of 1.0×10^{16} cm^{-3}.

To investigate whether or not the E3 defects depended on the Si dopant, we did introduction rate measurements of the main component, E3a, for three different carrier densities. Figure 3 shows the results, and it is clear that the introduction rate was the same for all the free carrier densities. This indicates that the E3a defect does not involve a dopant atom, in this case Si. We found the introduction rate of the E3a in our samples was 0.42 cm^{-1}, which agrees with the value of

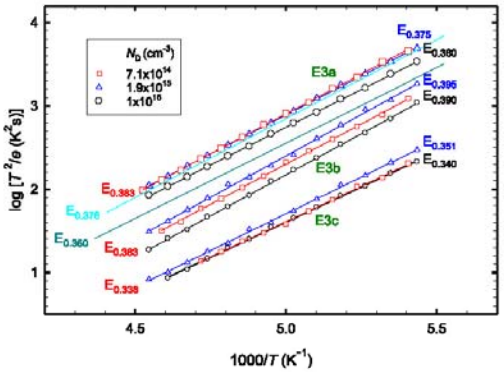

Figure 2. Arrhenius plots of the E3 in GaAs for 3 different carrier densities. The solid lines without symbols are for conventional DLTS scans. The subscripts beneath the E labels are the DLTS activation energies in eV determined from the Arrhenius plots. Note that the error bars for the E3b and E3c for the 7.1×10^{14} cm^{-3} are ± 0.01 because these defects are present in very low concentrations compared the defects in the 1.0×10^{16} cm^{-3} GaAs.

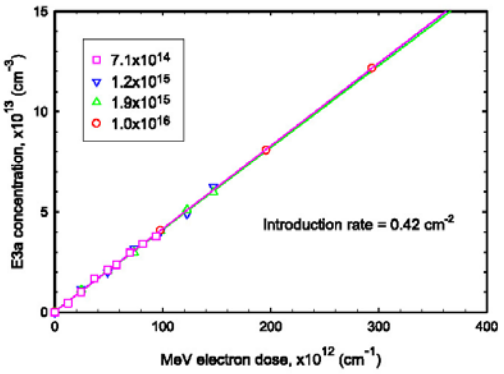

Figure 3. Concentration of the E3a in GaAs as a function of electron fluence from a ^{90}Sr radionuclide.

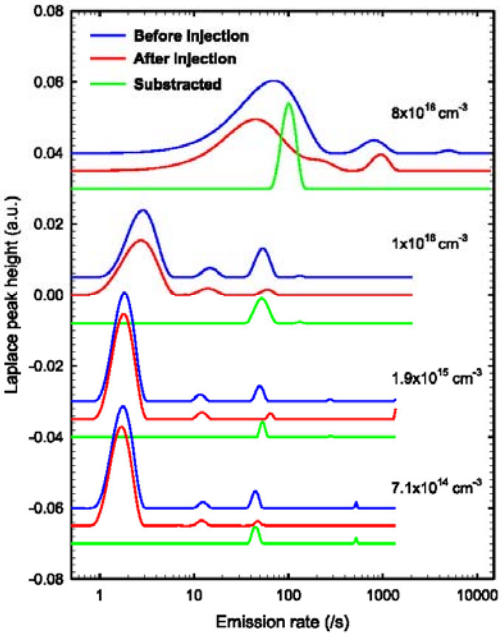

Figure 4. Laplace spectra of electron irradiated n-GaAs with four different carrier densities for three different types of spectra (as indicated in the figure). Spectra were recorded at a reverse bias of −2 V and a filling pulse amplitude of 2 V. The measurement temperature was 180 K.

0.4 cm^{-1} found by Pons [7]. Note that the E3b and E3c components for the lower doping density GaAs were too small to allow for an accurate measurement of their introduction rates as a function of doping density.

Figure 4 shows Laplace DLTS spectra of samples with different carrier densities. For each carrier density, three different spectra are shown: before minority carrier injection, after injection and subtracted from each other. The principles of minority carrier injection were first explained by Auret *et al* [18] and it was applied for the E3 defects in GaAs [19]. Firstly, from the graphs we see that the relative concentration of the E3c increased with increasing carrier density. Secondly, before injection the spectrum consisted of all 3 components of the E3 defect. However, after injection the E3c was reversibly removed and the spectrum consisted only of E3a and E3b. The injected spectrum was recorded after subjecting the diode to minority carrier injection pulses at low temperatures (90–120 K). For the re-introduction of the E3c, the sample was heated to above 160 K under zero bias. The subtracted spectrum shows only the E3c. These processes were reproducible and indicate that the E3c is metastable. This phenomenon has been observed previously [20], and been ascribed to charge state controlled metastability involving hole capture and emission.

Electric field dependence of the main E3 component, E3a, was measured for 3 different carrier densities to distinguish between Poole–Frenkel (emission rate proportional to the square root of the electric field) and phonon-assisted tunneling (emission rate proportional to the square of the electric field) [13, 14]. From figure 5 it is clear that the field enhanced emission of carriers is best described by phonon-assisted tunnelling, with all 3 different carrier densities providing consistent results. Figure 6(a) shows the graphs of emission rate versus the square of the electric field for different temperatures (200, 205, 210, 215 and 220 K) as well as the tunnelling time as a function of $1000/T$. It is clear that the linear relationship between emission rate and electric field squared is valid over a wide temperature range.

The model by Ganichev and Prettl [21] describes the phonon-assisted tunnelling in terms of the tunnelling time of

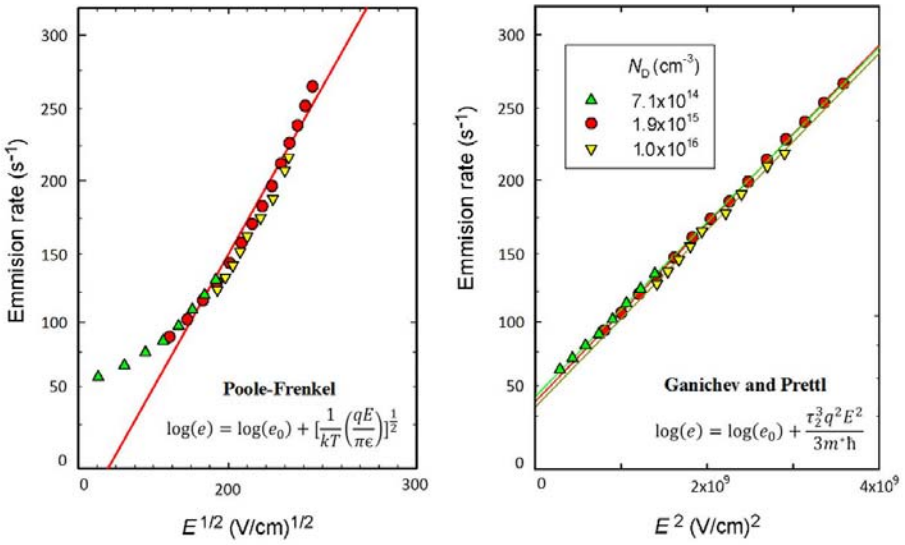

Figure 5. Electric field dependence of E3a in GaAs for different free carrier densities.

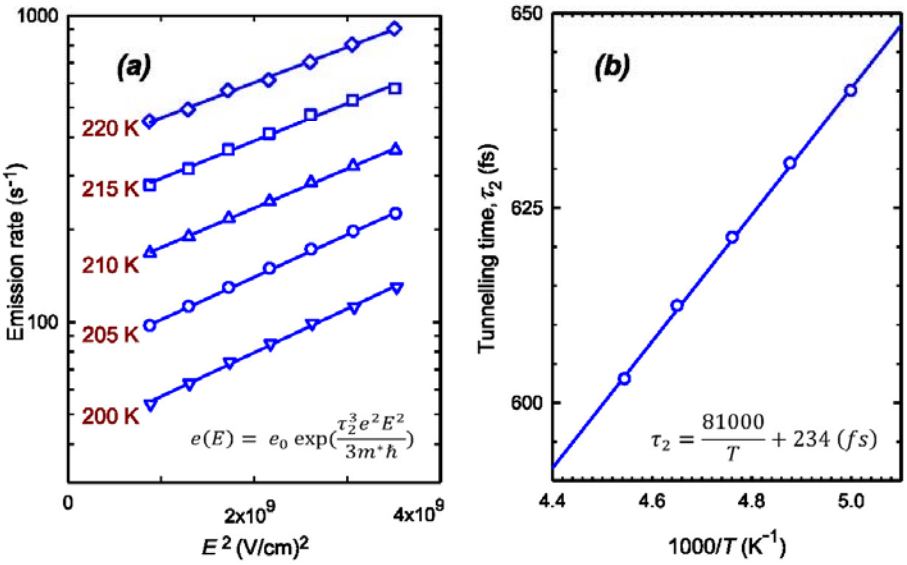

Figure 6. (a) Electric field dependence of E3a in GaAs for different temperatures. (b) Tunneling time versus $1000/T$ for the E3a. The equation of the regression line is shown in the legend.

an electron through the potential well of the defect:

$$e(E) = e_0 \exp\left(\frac{\tau_2^3 e^2 E^2}{3m^*\hbar}\right). \quad (1)$$

In this equation τ_2 is the tunnelling time, E is the electric field strength, m^* is the effective mass of an electron and $\hbar$ is the Planck constant. We measured the tunnelling time according to this model and figure 6(b), and it was found to be given by

$$\tau_2 = \frac{81000}{T} + 234\ (fs). \quad (2)$$

True capture cross-section measurements of E3a were done for two different carrier densities (1.9×10^{15} and 1.0×10^{16}) cm^{-3} as shown in figure 7. The DLTS signal after application of a

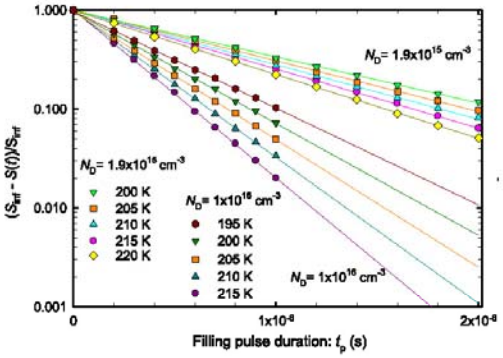

Figure 7. Determination of the capture cross section of E3a in GaAs for $N_D = 1.9 \times 10^{15}$ cm ^{3} and $N_D = 1.0 \times 10^{16}$ cm ^{3}.

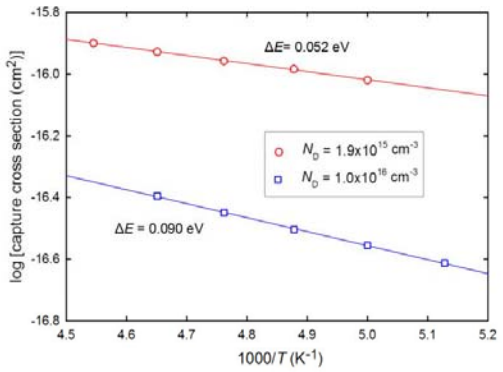

Figure 8. Arrhenius plot for the determination of the capture barrier of the E3a in a GaAs for $N_D = 1.9 \times 10^{15}$ cm ^{3} and $N_D = 1.0 \times 10^{16}$ cm ^{3}.

filling pulse of length t_p, may be described by [22]

$$S(t_p) = S_{\text{inf}}\left[1 - \exp\left(\frac{t_p}{\tau_c}\right)\right] \tag{3}$$

here S_{inf} is the magnitude of the DLTS signal observed after a filling pulse sufficiently long to fill all the defects and τ_c is the time constant of the capture process given by

$$\tau_c = \sigma N_d v_{\text{th}}, \tag{4}$$

where σ is the capture cross section, N_d is the free carrier density and v_{th} is the thermal velocity of the carriers [22]. It follows that σ may be determined from the slope of the plot shown in figure 7:

$$\sigma = 2.3 \text{ slope}/N_D v_{\text{th}}. \tag{5}$$

Calculations using equation (5), with experimentally determined slopes and values of N_D, show that the capture cross section for material with a free carrier concentration of 1.0×10^{16} cm^{-3} is about a factor of three lower than that with 1.9×10^{15} cm^{-3} (3.1×10^{-17} cm^2 versus 1.0×10^{-16} cm^2).

The temperature dependence of the capture cross section may be explained by the existence of a capture barrier, ΔE, so that the capture cross section as a function of the temperature is given by [22]

$$\sigma(T) = \sigma_\infty e^{\frac{-\Delta E}{kT}}, \tag{6}$$

where k is the Boltzmann constant and T is the temperature. The capture cross section for samples with a carrier density of 1.0×10^{16} and 1.9×10^{15} cm^{-3} were measured at different temperatures and are used in figure 8 to calculate the capture barriers. As shown in figure 8, the capture barrier for 1.9×10^{15} cm^{-3} is 0.052 eV and for 1.0×10^{16} cm^{-3} is 0.090 eV. Thus, when applying equation (6) to our results, the capture barrier for higher carrier densities is higher than for lower carrier densities.

Figure 9 demonstrates the effect of annealing on the E3 defect. The annealing measurements were done for the sample with a carrier density of 1.0×10^{16} cm^{-3}. As can be seen, the E3b defect annealed out before the other two at 500 K. E3a

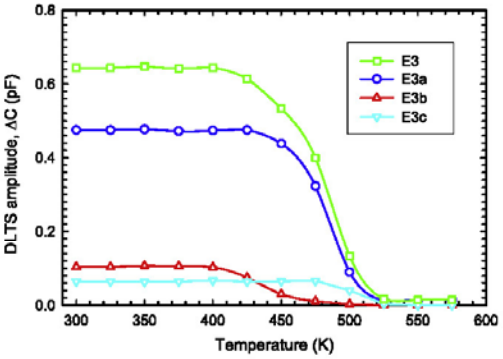

Figure 9. Isochronal annealing (10 min periods) of the components of the E3 defect in GaAs, and the total E3 (square symbol) is the sum of the three E3 components.

and E3c annealed out simultaneously at 525 K. This indicates that the E3b defect is structurally different from the others.

In summary, we found that the E3 is not a single defect but rather consists of three separate levels (E3a, E3b and E3c). The activation energies and apparent capture cross sections were calculated for defects in 1.0×10^{16} cm^{-3} doped GaAs. Results from introduction rate studies indicate that the concentration of E3a and E3b is independent of the doping density and hence these defects do not involve dopant atoms. For E3c the results suggest that this component is highly dependent on carrier density. We therefore conclude that the E3c defect involves a Si dopant atom. In addition, the E3c was found to be metastable. Furthermore, results from annealing profiles for all three components show that the E3b annealed out at 500 K and the E3a and E3c annealed out at 525 K. From this, we conclude that the three components of the E3 defect are due to three structurally different defects that coincidently happen to have similar emission rates. This might explain why there is so much uncertainty in the

literature about the origin of the E3. Perhaps the most interesting proposal was by Bondarenko *et al* [23] who deduced from positron annihilation and Hall measurements that in Si-doped GaAs, E3 may be V_{Ga}–Si_{Ga}. This proposed defect could well be our E3c of which we have shown that the concentration is directly proportional to the Si doping concentration. E3a is the most prominent component of E3 and may therefore be the V_{As} which Bondarenko *et al* [23] predicted to form in undoped GaAs. The latest reports regarding the E3 origin by Schultz [9] supports that E3 is V_{As}. According to Stievenard *et al* [8] the E3b can be As_i, as they mentioned E3 is a V_{As}–As_i and the As_i was found to anneal out earlier (around 493 K) than V_{As} (around 523 K), then we can conclude that E3b is As_i. The annealing temperature of the E3a is further support for the E3a being due to the V_{As}.

4. Conclusions

DLTS spectra recorded between 20 and 300 K show the presence of the E1, E2 and E3 defects in electron irradiated n-type GaAs. By using Laplace DLTS we have found that the E3 is not a single peak but consists of three individual components (E3a, E3b and E3c) with different structures. For the $1.0 \times 10^{16}\,cm^{-3}$ doped GaAs the activation energies were 0.360 eV, 0.392 eV and 0.335 eV, respectively, and their apparent capture cross sections were $2.1 \times 10^{-14}\,cm^2$, $4.8 \times 10^{-13}\,cm^2$ and $6.8 \times 10^{-14}\,cm^2$ for E3a, E3b and E3c, respectively. Carrier density dependent introduction rate results indicate that the E3c defect involves a Si dopant atom while the E3a and E3b do not. In addition, the E3c is also metastable: it can be removed by injecting minority carriers at low temperatures and re-introduced by heating up above 160 K under zero bias. Very important, we also observed that of the three components, the E3b annealed out first at 500 K and both the other components annealed out at 525 K. We conclude that all three components are structurally different and, by comparing the properties with results with those of other researchers, it is clear that E3a is V_{As}, E3b is As_i and E3c is V_{Ga}–Si_{Ga}. From the electric field measurements, we found that the field enhanced emission of carriers was well described by phonon-assisted tunnelling. It was found that the capture cross section of the $1.9 \times 10^{15}\,cm^{-3}$ doped material is higher than in the $1.0 \times 10^{16}\,cm^{-3}$ doped material.

Acknowledgments

This work is based on the research supported by the National Research Foundation of South Africa under grant number 98961. Opinions, findings and conclusions or recommendations are that of the authors, and the NRF accepts no liability whatsoever in this regard. The Laplace DLTS software and hardware used here were received from L Dobaczewski (Institute of Physics, Polish Academy of Science) and A R Peaker (Center for Electronic Materials Devices and Nanostructures, University of Manchester).

ORCID iDs

F Taghizadeh https://orcid.org/0000-0002-2554-8203

References

[1] Lang D V 1974 Deep-level transient spectroscopy: a new method to characterize traps in semiconductors *J. Appl. Phys.* **45** 3023–32
[2] Benton J L J 1990 Characterization of defects in semiconductors by deep level transient spectroscopy *J. Cryst. Growth* **106** 116–26
[3] Dobaczewski L, Peaker A R and Bonde Nielsen K 2004 Laplace-transform deep-level spectroscopy: the technique and its applications to the study of point defects in semiconductors *J. Appl. Phys.* **96** 4689–728
[4] Meyer W E 2006 Digital DLTS studies on radiation induced defects in by Walter Ernst Meyer PhD (Physics) in the faculty of natural & agricultural science university of Pretoria november 2006 supervisor: Prof F D Auret Digital DLTS studies on radiation induced defects, pp 0–5
[5] Lang D V, Logan R A and Kimerling L C 1977 Identification of the defect state associated with a gallium vacancy in GaAs and $Al_xGa_{1-x}As$ *Phys. Rev.* B **15** 4874–82
[6] Farmer J W, Look D C and Look D C 1980 Electron irradiation defects in n-type GaAs electron-irradiation defects in n-type GaAs *Phys. Rev.* B **21** 3389–98
[7] Pons D *et al* 1985 Irradiation-induced defects in GaAs *J. Phys. C: Solid State Phys.* **18** 3839–71
[8] Stievenard D, Boddaert X, Bourgoin J C and von Bardeleben H J 1990 Behavior of electron-irradiation-induced defects in GaAs *Phys. Rev.* B **41** 5271–9
[9] Schultz P A *et al* 2015 The E1–E2 center in gallium arsenide is the divacancy *J. Phys.: Condens. Matter* **27** 075801
[10] Murawala P A, Singh V A, Subramanian S, Chandvankar S S and Arora B M 1984 Origin of an E3-like defect in GaAs and $GaAs_{1-x}Sb_x$ alloys *Phys. Rev.* B **29** 4807–10
[11] Von Bardeleben H J, Bourgoin J C and Miret A 1986 Identification of the arsenic-antisite-arsenic-vacancy complex in electron-irradiated GaAs *Phys. Rev.* B **34** 1360–2
[12] Schick J T, Morgan C G and Papoulias P 2002 First-principles study of As interstitials in GaAs: convergence, relaxation, and formation energy *Phys. Rev.* B **66** 1953021
[13] Ganichev S, Ziemann E, Prettl W and Yassievich I 2000 Distinction between the Poole–Frenkel and tunneling models of electric-field-stimulated carrier emission from deep levels in semiconductors *Phys. Rev.* B **61** 10361–5
[14] Pienaar J, Meyer W E, Auret F D and Coelho S M M 2012 Comparison of two models for phonon assisted tunneling field enhanced emission from defects in Ge measured by DLTS *Physica* B **407** 1641–4
[15] Auret F D, Bredell L J, Myburg G and Barnard W O 1991 Simultaneous observation of sub- and above threshold electron irradiation induced defects in gaas *Japan. J. Appl. Phys.* **30** 80–3
[16] Tunhuma S M, Auret F D, Legodi M J and Diale M 2016 The fine structure of electron irradiation induced EL2-like defects in n-GaAs *J. Appl. Phys.* **119** 145705

Materials Science in Semiconductor Processing 99 (2019) 23–27

Contents lists available at ScienceDirect

Materials Science in Semiconductor Processing

journal homepage: www.elsevier.com/locate/mssp

Electronic properties and transformation kinetics of two prominent metastable defects introduced in GaAs during sputter deposition of Au Schottky contacts

F. Taghizadeh*, P.J. Janse van Rensburg, K. Ostvar, W.E. Meyer, F.D. Auret

Department of Physics, University of Pretoria, Private Bag X20, Hatfield, 0028, Pretoria, South Africa

ARTICLE INFO

Keywords:
Sputter-deposition induced defects in GaAs
Laplace deep-level transient spectroscopy
Metastability
Transformation kinetics
Near-surface damage

ABSTRACT

Au Schottky barrier contacts (SBDs) were DC sputter deposited on Si doped n-type GaAs at a power of 150 W. Deep-level transient spectroscopy (DLTS) and Laplace DLTS were used to characterize the sputter-induced defects near the surface of the GaAs. In this study, *I-V* and *C-V* measurements showed that the sputter deposited diodes had a significantly lower barrier height and a higher free carrier density. Using DLTS, it was found that this sample contained seven defects – three of them were metastable while one of the others was highly dopant dependent. The energy levels of these defects are E_c – 0.046 eV, E_c – 0.22 eV, E_c – 0.30 eV, E_c – 0.55 eV, E_c – 0.56 eV, E_c – 0.83 eV and E_c – 0.84 eV. The EL2 defect was not observed in the sputtered samples, but one of the sputter-induced defects emitted in the same range as the EL2, however, it had two components and their DLTS signatures (E_c – 0.83 eV and E_c – 0.84 eV) differed significantly from that of the EL2. By applying different bias conditions (− 2 V and zero V) for annealing procedures, the metastable defects (E_c – 0.30 eV and E_c – 0.56 eV) were transformed into each other. The pre-factor obtained from transformation rate of E_c – 0.56 eV → E_c – 0.30 eV under reverse bias was 3×10^{15} s^{-1} which is related to free carrier emission.

1. Introduction

Schottky barrier diodes (SBDs) play a significant role in very large-scale integration technology [1]. Sputter deposition is one of the methods to fabricate both low and high-barrier SBDs The advantages of sputter deposition are: ability to deposit metals with high melting point, stoichiometric deposition of compounds, high deposition rate and better adhesion than resistive deposition [2,3]. However, the energetic particles involved in this process introduce surface and sub-surface disorder, and these unwanted disorders affect the rectification characteristics of Schottky diodes [2]. The surface and sub-surface disorder introduce defects that have both discrete levels in the semiconductor band gap as well as continuous energy levels [4]. The barrier height of the sputter deposited metal contacts on n-type GaAs are lower than similar resistively-deposited contacts and higher for p-type GaAs [5]. Recently, deep level transient spectroscopy (DLTS) has been used to investigate the defects introduced in epitaxially grown Si-doped and bulk-grown GaAs [3,5,6,7].

Laplace DLTS is a high resolution technique capable of resolving defects with closely spaced emission rates in order to characterize them. In this study, we used high resolution Laplace DLTS, introduced by Dobaczewski et al. in 2004 [8], to investigate the electrical properties in the 20–405 K temperature range of defects introduced during sputter deposition of Au on Si-doped n-type gallium arsenide (GaAs).

2. Experimental procedure

The *n*-GaAs used in this study was grown by metalorganic vapour phase epitaxy (MOVPE) on n^+ GaAs substrates. These samples were doped with Si to 1.0×10^{15} cm^{-3} and 1.0×10^{16} cm^{-3}, respectively. First, the samples were degreased and chemically etched. Thereafter Ni/AuGe/Ni ohmic contacts with thicknesses of 100/1450/300 Å, respectively, were fabricated on the back surface, then they were annealed in Ar at 450 °C for 2 min to form the ohmic contact.

After ohmic contact fabrication, samples were cleaned and etched again, and mounted immediately inside the vacuum chamber for the sputter deposition of the Schottky contacts. Circular Au Schottky contacts were sputter deposited through a metal contact mask onto the GaAs layers. The depositions were carried out at a DC power of 150 W at an Ar pressure of 8×10^{-2} mbar with a DC bias of 580 V for 5 min.

For the control sample the cleaning and ohmic contact deposition

* Corresponding author.
E-mail address: f.taghizadeh@tuks.co.za (F. Taghizadeh).

https://doi.org/10.1016/j.mssp.2019.04.012
Received 3 October 2018; Received in revised form 6 April 2019; Accepted 6 April 2019

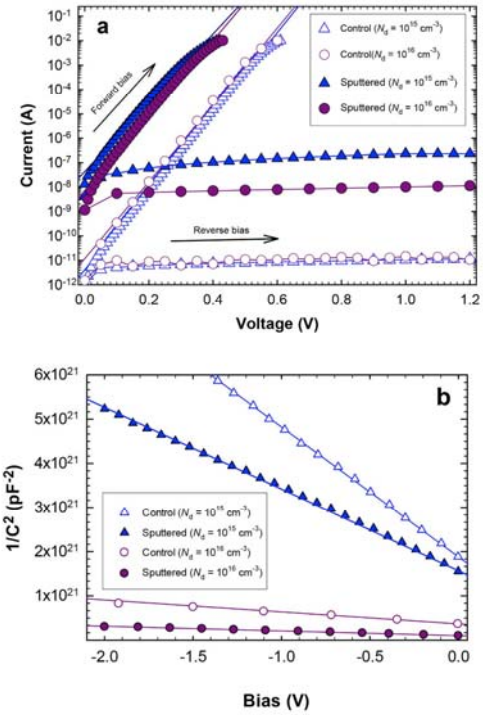

Fig. 1. Demonstrates the change in (a) I-V and (b) C-V plots as a result of sputter deposition of Schottky contacts on $1.0 \times 10^{15}\,cm^{-3}$ and $1.0 \times 10^{16}\,cm^{-3}$ samples.

procedures were the same as for the sputtered samples. After the second cleaning procedure the sample was quickly mounted in the same deposition chamber which was used for ohmic contact fabrication, and 0.6 mm diameter Au Schottky contacts were deposited (1000 Å) on the epitaxially grown surface of the samples through a metal contact mask.

The influence of these sputter-induced defects on the diode properties was assessed by current-voltage (*I-V*) and capacitance-voltage (*C-V*) measurements. The *I-V*/*C-V* measurements were performed at 25 °C, meanwhile the bias was applied by an HP 4140 B pA meter/Voltage source and a HP 4192 LF Impedance analyser, with the voltage monitored with a HP 34401A multimeter. All the control and sputtered samples were measured under the same conditions. The electrical properties of the sputter-induced defects in GaAs were characterized by DLTS and Laplace DLTS in the 20–405 K temperature range. DLTS temperature was measured using a platinum resistance thermometer and bias was applied by a dedicated Laplace DLTS card, monitored by an oscilloscope.

3. Results and discussion

As shown in Fig. 1, the *I-V* characteristics of the control samples were close to ideal, with an ideality factor of 1.02, indicating that thermionic emission was the dominant current transport mechanism. Both the sputtered contacts showed significantly worse *I-V* characteristics, with a higher ideality factor and lowering in barrier height. See Table 1 for details. Despite some deviation from ideality, the ideality factor remained close to one and the reverse leakage current did not increase significantly above the saturation current, indicating that thermionic emission was still the dominant current transport mechanism in the sputtered diodes. The lower doped material showed a higher reverse leakage current, probably due to more carrier generation by the defects in the wider depletion region. In both cases, the sputtered contacts had a higher series resistance than the those on the control samples.

Table 1
Diode parameters of n-type GaAs of control and sputter samples ($1.0 \times 10^{15}\,cm^{-3}$ and $1.0 \times 10^{16}\,cm^{-3}$).

Sample		n	φ_{IV}(eV)	φ_{CV}(eV)	$R_s(\Omega)$	carrier concentration (cm^{-3})
$1.0 \times 10^{15}\,cm^{-3}$	control	1.02	0.96	0.97	3.8	1.1×10^{15}
	sputtered	1.15	0.63	0.74	10	3.5×10^{15}
$1.0 \times 10^{16}\,cm^{-3}$	control	1.02	0.87	1.72	3.4	1.2×10^{16}
	sputtered	1.11	0.65	1.05	4.8	1.6×10^{16}

The *C-V* characteristics (plotted as $1/C^2$ vs V in Fig. 1) showed constant carrier concentration profiles for the control samples, while the sputtered samples showed a significant increase in carrier concentration and, similar to the *I-V* characteristics, a decrease in barrier height. The C-V barrier heights were higher than the *I-V* barrier heights, indicating that there might have been some barrier height inhomogeneities. The slight deviations from linearity in the *C-V* characteristics indicates a minor variation in the carrier density with depth. It is clear that the change in carrier density due to sputter deposition occurs to a depth much deeper than the depletion region probed, because unlike thermal deposition techniques, in plasma sputtering, the ions in the plasma gain significant energy before colliding with the substrate. Therefore, at the time of arrival, these sputtered particles have energies many times larger than the binding energy of the surface of the substrate and therefore can penetrate deeper into the material. It is therefore clear that sputter-related defects can diffuse a significant distance into the semiconductor [9].

The deviation from ideal thermionic emission as well as the reduction in the barrier height may be due to near-surface damage, changing the properties of the interface as well as deep level defects causing carrier generation and barrier height inhomogeneity, indicating poorer rectification due to sputter damage.

Fig. 2 depicts the DLTS spectra from sputter-induced defects and a control sample of *n*-GaAs, Si doped with concentration of $1.0 \times 10^{15}\,cm^{-3}$ and $1.0 \times 10^{16}\,cm^{-3}$. The DLTS spectra were obtained at rate windows of 80 s^{-1} and in the 20–405 K temperature range by applying a reverse bias and filling pulse amplitude of −1 V and 1.4 V, respectively. For the control sample (curve (a)) we observed only the EL2 defect. For the sputtered diodes on $1.0 \times 10^{16}\,cm^{-3}$ doped GaAs, we observed seven defects (S1, S2, S3, S4, S5 and S6a & S6b), as shown in curve (b). Curves (c) and (d) (recorded on $1.0 \times 10^{15}\,cm^{-3}$ doped GaAs) indicate the S5 and S3 are metastable: By applying −2 V at 400 K for 10 min and cooling under the same bias, S5 transformed to S3 and when zero bias at 400 K was applied for 10 min, followed by cooling under the same bias, the S3 transformed back to S5. Similarly, the S1 defect was metastable, and, as seen in Fig. 2, applying a reverse bias of −2 V at 400 K for 10 minutes introduced the S1 while zero bias at 400 K for 10 minutes totally removed it. However, no new defects was observed when the S1 was removed.

From Fig. 2 it is also clear that the S4 defect was highly dependent on the carrier density and the peak height decreased by about a factor ten when the dopant concentration was reduced by a factor 10. Note that in curves (c) and (d) the S4 peak height was multiplied by a factor of 10. The S2 was only observed in one of the $1.0 \times 10^{16}\,cm^{-3}$ doped samples, the reason for this is not yet clear.

Fig. 3 shows Arrhenius plots of the seven sputter-induced defects (at 26 K, 140 K, 180 K, 265 K, 320 K and 384 K in Fig. 3) in n-type GaAs with a carrier concentration of $1.0 \times 10^{15}\,cm^{-3}$. The activation energies of the sputter-induced defects are listed in Table 2. As seen in

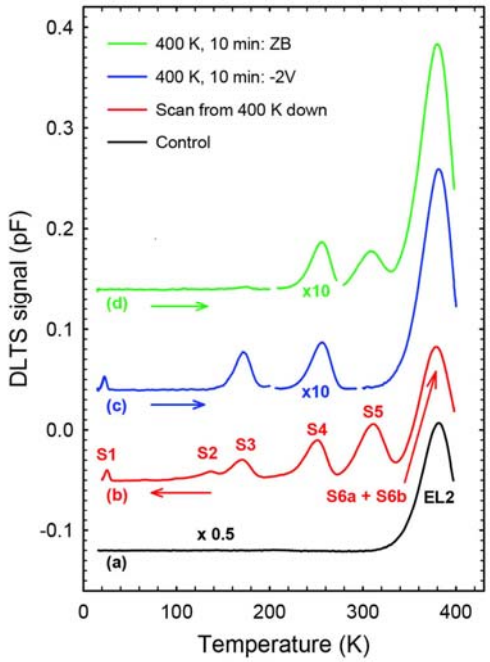

Fig. 2. DLTS spectra of (a) a control sample, (b) sample (1.0×10^{16} cm^{-3} Si doped) directly after sputtering, (c) sputtered sample (1.0×10^{15} cm^{-3} Si doped) after applying −2 V at 400 K for 10 minutes and (d) sputtered sample (1.0×10^{15} cm^{-3} Si doped) after applying zero bias for 10 minutes at 400 K. The reverse bias, V_r, and filling pulse amplitude, V_p, were −1.0 and 1.4 V, respectively with 1 ms pulse width and the rate window was 80 s^{-1} for all samples.

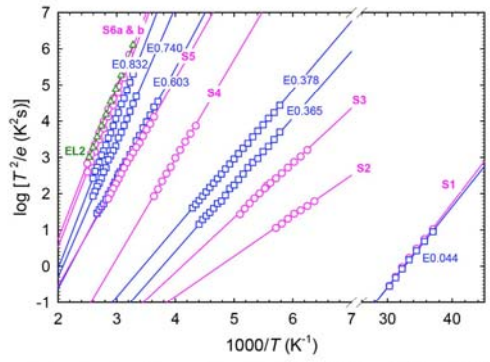

Fig. 3. Arrhenius plots of sputter-deposition induced defects (circle symbols), *n*-GaAs electron irradiation-induced defects (square symbols, labelled as in Table 1) and the EL2 (triangle symbols).

Fig. 3 the activation energy and apparent capture cross-sections of the sputter-induced defects differed from those of the high energy electron irradiation-induced defects. Laplace DLTS measurements (see later) showed that the S6 defect had two components which we labelled S6a and S6b. Some of the sputter-deposition induced defects were similar to sputter-etching induced defects reported by Venter et al. [10], nitride

Table 2
Electronic properties of sputter-induced defects (S1–S6), Stress related or nitride capping induced defects [11], hydrogen plasma induced defect [12,13], Ar plasma-etching induced defects [9], electron-irradiation induced defects and the EL2.

Defect label	Origin[a]	E_A (eV)	σ_a (cm^2)	Stability
S1	S	0.046	3.1×10^{-13}	Metastable
E1' [9]	P	0.040	5.3×10^{-14}	Metastable
S2	S	0.22	1.9×10^{-15}	Stable
S3	S	0.30	1.6×10^{-14}	Metastable (transformed to S5)
M4 [11]	NC	0.31	1.8×10^{-18}	Metastable (transformed to M3)
M4 [13]	H	0.30	–	Metastable (transformed to M3)
M4 [12]	H	0.30	–	Metastable (transformed to M3)
E(0.31) [9]	P	0.31	5.2×10^{-14}	Metastable (transformed to E0.61)
S4	S	0.55	1.0×10^{-12}	Stable
S5	S	0.56	1.3×10^{-14}	Metastable (transformed to S3)
M3 [11]	NC	0.61	5.1×10^{-18}	Metastable (transformed to M4)
M4 [13]	H	0.50	–	Metastable (transformed to M4)
M3 [12]	H	0.55	–	Metastable (transformed to M4)
E(0.61) [9]	P	0.61	7.1×10^{-14}	Metastable (transformed to E0.31)
S6a	S	0.83	8.8×10^{-13}	Stable
S6b	S	0.84	6.6×10^{-13}	Stable
E(0.044)	E	0.044	1.9×10^{-14}	Stable
E(0.365)	E	0.365	8.7×10^{-14}	Stable
E(0.378)	E	0.378	3.6×10^{-14}	Stable
E(0.603)	E	0.603	4.9×10^{-14}	Stable
E(0.740)	E	0.740	5.7×10^{-14}	Stable
E(0.832)	E	0.832	2.8×10^{-12}	Stable
EL2	N	0.82	3.2×10^{-13}	Stable

[a] S = Sputter (current study), NC = Stress related or/Nitride capping [11], H = Hydrogen plasma [12,13], P = Plasma etched (Ar) [10], E = electron irradiation and N = Native defect.

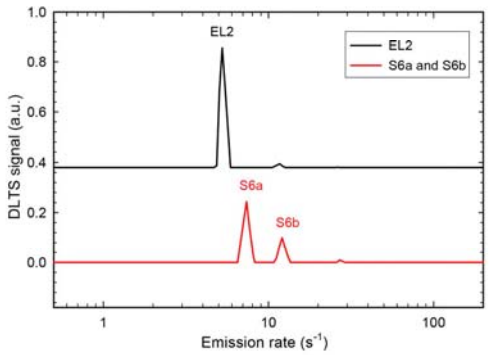

Fig. 4. Laplace spectra of EL2 and S6 defects as observed in 1.0×10^{15} cm^{-3} doped material. Both spectra were recorded at 350 K with a reverse bias of −1 V and a filling pulse amplitude of 1.4 V.

encapsulation [11] and hydrogen plasma treatment [12,13] (Comparison included in Table 2).

Fig. 4 depicts the Laplace DLTS results for the S6 defect in the sputtered sample and the EL2 defect in the control sample. It is clear that the S6 defect has two components (S6a and S6b) and they do not directly correspond to the EL2 defect. It is interesting that the EL2 defect in the control sample had a small component that was not previously observed. The samples that were sputter deposited did not have the EL2 defect, and we speculate that the EL2 was modified to S6a and S6b.

As shown in Fig. 3, the S3 and S5 defects were metastable. From Fig. 5, it is evident that the S3 transformed into the S5 after annealing under zero bias at 400 K for 10 minutes followed by cooling down under zero bias to 295 K, where the spectrum was measured under a bias of

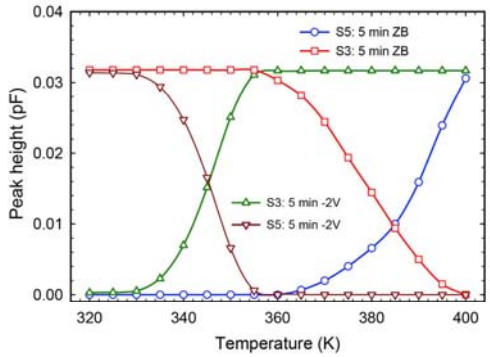

Fig. 5. Introduction and removal of S3 and S5 metastable defects. The conditions for the transformations are indicated in the figure.

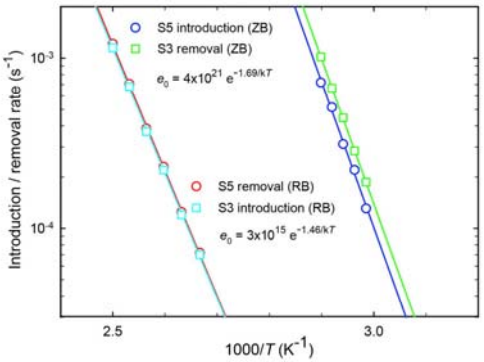

Fig. 6. Arrhenius data for the transformation of S3 → S5 and S5 → S3.

−1 V. Similarly, S5 could be transformed back to S3 under reverse bias (−2 V) while annealing at 400 K for 10 minutes followed by cooling down under −2 V to 180 K where the spectrum was measured under a bias of −1 V. It is interesting to observe the direct correlation between the concentration of S3 and S5. Fig. 5 shows the introduction and removal curves of the metastable defects. Transformation curves were measured by transforming as much as possible of the defect into one state at 400 K (−2 V bias for the S3, 0 V bias for the S5) followed by cooling (under the same bias conditions) to the annealing temperature, where the sample was annealed under the transformation conditions (0 V bias or −2 V bias respectively) for 5 minutes, followed by rapid cooling to the measurement temperature (295 K or 180 K) under the transformation conditions.

The isochronal transformation of S3 → S5 and S5 → S3 was modelled by first order kinetics:

$$N_X(t, T) = N_0[1 - \exp(-te_0(T))] \quad (1)$$

and

$$N_Y(t,T) = N_0\exp[-te_0(T)] \quad (2)$$

where N_X corresponds to the defect being removed and N_Y to the defect being introduced.

In these equations, N_0 is the maximum defect concentration, t is the annealing time in seconds and $e_0(T)$ is the temperature dependent transformation rate, in s^{-1}. The transformation rates can be written as:

$$e_0(T) = \alpha \exp(-E/kT) \quad (3)$$

In this equation, α, is a pre-factor with units of s^{-1}, E is the activation barrier for the particular transformation of the defect and k is the Boltzmann constant.

In Fig. 6, Arrhenius data of introduction and removal rate of S3 and S5 metastable defects are shown and transformation rate for each one was calculated.

In these transformation rates we have 3×10^{15} s^{-1} and 4×10^{21} s^{-1}, respectively, as pre-factors for equation. (3). The pre-factor obtained from our measurements to transform S5 from S3 is almost the same as the one reported by Buchwald et al. [11] (10^{21} s^{-1} pre-factor of formation M4 and decay of M3). For the transformation of S3 to S5 the pre-factor was 10^{15} s^{-1}, which is higher than the 10^{7} s^{-1} reported by Buchwald et al. [11], 10^{8} s^{-1} reported by Conibear et al. [12] and 10^{11} s^{-1} reported by Pfeiffer and Weber [13].

The pre-factor α can be physically related to the attempt frequency of the process and can be used to deduce the physical mechanism leading to the temperature dependence. Some mechanisms identified so far [14] include elementary atomic jump ($\alpha \sim 10^{12}$ s^{-1}), free-carrier capture by multiphonon emission ($\alpha \sim 10^{7}$ s^{-1}), free-carrier emission ($\alpha \sim 10^{13}$ - 10^{14} s^{-1}). The high prefactor for the transformation of S3 to S5 ($\alpha \sim 10^{21}$ s^{-1}) is even larger than would be expected for direct free-carrier capture by a potential well with a large capture cross-section. The smaller capture prefactor for the transformation S5 to S3 seems to indicate free carrier emission.

4. Conclusions

Au Schottky barrier contacts (SBDs) were fabricated on n-type GaAs using DC sputtering and their electrical properties were investigated. *I-V* and *C-V* results indicate that the ideality factor and Schottky barrier height significantly changed compared to the resistively deposited control sample. DLTS spectra were recorded over a temperature range of 20–400 K. Sputter deposition introduced seven defects in GaAs, of which the energy levels range from E_c – 0.046 eV to E_c – 0.84 eV, of which one was highly dopant dependent. Laplace DLTS was used to characterize the defects. From the Arrhenius plots we extracted the activation energy and apparent capture cross-section of each defect. One defect, labelled the S6, consisted of two different components and differed significantly from the EL2 defect which appears in the same temperature range, but was not observed in the sputtered samples.

None of the defects were similar to those observed after electron irradiation but three were similar to those found in nitride encapsulation, hydrogen plasma and Ar plasma etched samples. Annealing the sample at 400 K under two different bias conditions, namely -2 V and 0 V, showed that three of them are metastable. Two peaks, E_c – 0.30 eV and E_c – 0.56 eV, transformed into each other with electron capture being the rate determining step for one of the transformation processes. The E_c – 0.046 eV defect was metastable as well but we could not find the defect which it transforms into.

Acknowledgements

This work is based on the research supported by the National Research Foundation of South Africa under grant number 98961. Opinions, findings and conclusions or recommendations are that of the authors, and the NRF accepts no liability whatsoever in this regard. The Laplace DLTS software and hardware used here was received from L. Dobaczewski (Institute of Physics, Polish Academy of Science) and A. R. Peaker (Center for Electronic Materials Devices and Nano-structures, University of Manchester).

Appendix A. Supplementary data

Supplementary data to this article can be found online at https://doi.org/10.1016/j.mssp.2019.04.012.

References

[1] F.D. Auret, O. Paz, N.A. Bojarczuk, Characterization of process-induced defects and device properties of ion beam sputter-deposited Mo contacts on Si, J. Appl. Phys. 55 (6) (Mar. 1984) 1581–1589.

[2] Y. Leclerc, F.D. Auret, S.A. Goodman, G. Myburg, C. Schutte, Electronic properties of defects introduced during sputter deposition of Cr Schottky contacts on GaAs, Ion Beam Modification of Materials, Elsevier, 1996, pp. 870–873.

[3] F.D. Auret, S.A. Goodman, G. Myburg, W.O. Barnard, Electrical characterization of sputter-deposition-induced defects in epitaxially grown n-GaAs layers, Vacuum 46 (8–10) (Aug. 1995) 1087–1090.

[4] F.D. Auret, S.A. Goodman, G. Myburg, W.E. Meyer, Electrical characteristics of Ar-ion sputter induced defects in epitaxially grown n-GaAs, J. Vac. Sci. Technol. B Microelectron. Nanom. Struct. 10 (6) (Nov. 1992) 2366.

[5] D.A. Vandenbroucke, R.L. Van Meirhaeghe, W.H. Laflère, F. Cardon, "Sputter-induced damage in Al/n-GaAs and Al/p-GaAs Schottky barriers," *Semicond*, Sci. Technol. 2 (5) (May 1987) 293–298.

[6] W.J. Devlin, R.F. sputtered Au-Mo contacts to n-GaAs, Electron. Lett. 16 (3) (1980) 92.

[7] M.G. Lupo, A. Cola, L. Vasanelli, A. Valentini, Deep level transient spectroscopy of Mo/GaAs Schottky barriers prepared by DC sputtering, Phys. Status Solidi 124 (2) (Apr. 1991) 473–481.

[8] L. Dobaczewski, A.R. Peaker, K. Bonde Nielsen, Laplace-transform deep-level spectroscopy: the technique and its applications to the study of point defects in semiconductors, J. Appl. Phys. 96 (9) (2004) 4689–4728.

[9] A.H. Eltoukhy, J.E. Greene, "Diffusion enhancement due to low-energy ion bombardment during sputter etching and deposition, J. Appl. Phys. 51 (8) (Aug. 1980) 4444–4452.

[10] A. Venter, et al., Ar plasma induced deep levels in epitaxial *n* -GaAs, J. Appl. Phys. 111 (1) (Jan. 2012) 013703.

[11] W.R. Buchwald, G.J. Gerardi, E.H. Poindexter, N.M. Johnson, H.G. Grimmeiss, D.J. Keeble, Electrical and optical characterization of metastable deep-level defects in GaAs, Phys. Rev. B 40 (5) (Aug. 1989) 2940–2945.

[12] A.B. Conlbear, A.W.R. Leitch, C.A.B. Ball, Third metastable hydrogen-related level in n -type GaAs, Phys. Rev. B 47 (4) (Jan. 1993) 1846–1848.

[13] G. Pfeiffer, J. Weber, Metastable defects in N-type GaAs related to hydrogen, Mater. Sci. Forum 143–147 (Oct. 1993) 873–878.

[14] A. Chantre, Introduction to defect bistability, Appl. Phys. Solid Surf. 48 (1) (Jan. 1989) 3–9.